D 2067

Università
Ca'Foscari
Venezia

Corso di Dottorato di ricerca
in Science and Management of
Climate Change
ciclo XXXII

Tesi di Ricerca

Seasonal to interannual variability on the southeast Greenland shelf: a study focused on the Sermilik area.

SSD: GEO12

Coordinatore del Dottorato
ch. prof. Carlo Carraro

Supervisore
Dott.ssa Simona Masina

Co-Supervisore
Dtt.ssa Doroteaciro Iovino

Co-Supervisore
Dtt.ssa Fiammetta Straneo

Dottorando
Federica Facchinetti
Matricola 956310

Contents

1 General introduction **1**

2 Analysis of the South-East Greenland shelf mean state and seasonal variability with GLOB16 model **5**
2.1 Introduction 5
2.2 Model specification and datasets 8
2.2.1 The GLOB16 configuration 8
2.2.2 Observational datasets 10
2.3 Results 13
2.3.1 Mean state on South-East Greenland shelf 13
2.3.2 Seasonal variability on South-East Greenland shelf . 34
2.4 Discussion and conclusions 57

3 Mechanisms and processes responsible for the observed temperature variability on the SE Greenland shelf **61**
3.1 Introduction 61
3.2 Observational datasets 62
3.3 Results 64
3.3.1 Inter-annual variability validation 64
3.3.2 Inter-annual variability mechanisms and processes . . 71
3.4 Summary 88

4 Numerical simulations of the Sermilik fjord dynamics with an high resolution model **91**
4.1 Introduction 91
4.2 Sermilik fjord circulation 94
4.3 Methodology and experiments design 100
4.3.1 SURF model characteristics and work-flow 100
4.3.2 Experimental set-up 103
4.3.3 Freshwater runoff implementation 106

4.4 Results 110
4.4.1 Summer (HRS) and winter (HRW) experiments . . . 110
4.4.2 Summer and wint er experiments with runoff (HRSr and HRWr) 120
4.4.3 Summer sensitivity experiments 128
4.5 Summary 149

5 Summary and conclusions **151**

Chapter 1

General introduction

The Greenland ice sheet underwent rapid and large changes over the decade 2000-2010, with increased net mass loss observed via many of its outlet glaciers (e.g. [1], [2]). The causes for these dynamic changes are still not well understood, but the leading hypotheses to explain the retreat of the glaciers is the ocean forcing, involving an increase in sub-marine melting at the ice-ocean interface [3] . The glacier retreat, in particular for South-East Greenland glaciers, coincided with a rapid warming of the Sub-Polar North Atlantic gyre that began in the mid-1990s and that is still going on [3].
These findings make the understanding of the processes behind the SE Greenland variability crucial for future climate projections, since they raise the potential for continued increases in warming and ice-mass loss, and eventually have implications for sea level rise and climate.
In particular, south of Denmark Strait, the South-East (SE) Greenland continental shelf is characterized by the presence of the East Greenland boundary current system (Fig. 1.1), formed by:

- The Arctic-origin, fresh and cold East Greenland Current (EGC) that flows southward on the shelf-break;

- The Atlantic-origin, salty and warm Irminger Current (IC) that recirculates from the Irminger Sea and merges with the EGC to form a single flow that is often referred to as the East Greenland/Irminger Current (EGC/IC) or slope current;

- The East Greenland Coastal Current (EGCC), possibly branching from the EGC south of the Denmark Strait or further upstream, on the inner shelf;
- The East Greenland Spill Jet, formed by dense water cascading off the shelf south of Denmark Strait (e.g. [4])

In recent modeling studies ([5]; [6]; [7]; [8]) the freshwater flowing on the SE shelf of Greenland and carried by the EGCC and EGC (which includes Arctic freshwater, sea ice, Greenland melt and icebergs) has been shown to be one of the main sources of freshwater for the subpolar gyre interior.
Additionally, freshwater export from the Arctic and Greenland is expected to increase, influencing the stratification of the adjacent Labrador Sea, and in turn the deep convection and the strength of the Atlantic Meridional Overturning Circulation. [6], [9], [10], [11]
A more complete understanding of the relative partitioning of the water masses composing the EGCC is important for evaluating the amount of heat entering the glacial fjords that influences the melting of Greenland's outlet glaciers. The water masses composition influences the variability of the water masses that are forced into Greenland's glacial fjords, and then in turn the heat content of waters that can be found at the glacier-ocean interface. [12]
In this region Greenland glacial fjords are fjords with a marine-terminating glacier that connect the Greenland Ice Sheet (GrIS) and the the North Atlantic sub-polar gyre. They are a key feature of the Greenland coast, importing oceanic heat and exporting melt-water into the ocean. Glacial fjords are usually very long and narrow (50-100 km long and 5-10 km wide), and the properties of the water inside the fjords resemble the water masses that are found on the continental shelf outside them.
Since a significant portion of this loss is due to acceleration of the fjord-terminating outlet glaciers, particularly those along the SE coast of Greenland (e.g. [13]), understanding the fjords' internal dynamics, its exchanges with the outside shelf and the export paths of the melted water is critical. Glaciers are found in remote regions, thus obtaining data is difficult and costly, and challenging due to the presence of calving glaciers and icebergs. For these reasons numerical models can be used as a key tool for determining how submarine melting and its characteristic influences the dynamics within the fjord. To shed light on these aspects, the

case-study of the Sermilik fjord in South-East Greenland is proposed.
The Sermilik fjord is located in the SE sector of Greenland and includes the Helheim glacier, one of the Greenland's largest outlet glaciers that account for ∼20% of the ice sheet's mass discharge [14].
Since the relative partitioning of the water masses composing the EGCC changes both seasonally and inter-annually, a more complete understanding of the hydrographic variability of the East Greenland Coastal Current is important also for investigating shelf-fjord exchange.
The observational record on the continental shelf is scarce in space and time, and to address all the above-mentioned uncertainties two 'frontier' resolution models, GLOB16 and high-RES have been used and analyzed.
GLOB16 is an eddy-resolving global ocean/sea ice configuration with a horizontal resolution of 1/16° or ∼4 km on the SE Greenland shelf. It has been used to investigate the variability and evolution of the currents progressing along the east Greenland shelf, as well as the extent to which the inter-annual changes on the shelf are due to changes in atmospheric forcing, subpolar-gyre circulation and changes in the transport of the East Greenland Current system.
The advantages of treating these issues with a global model, instead of the more commonly used regional configurations, are the possibility to analyze and address the mechanisms responsible for the variability of a region where these processes are largely influenced by large scale climate modes.
Moreover, since this resolution is not adequate to resolve the ocean dynamics within the Sermilik fjord, a regional configuration model at a very high resolution (1/48° horizontal resolution that translates to an horizontal resolution of 1 km on the shelf) has been nested in the first global model in order to understand the processes that control the properties and circulation outside and within the fjords.
In synthesis, the aim of this thesis is to address the following questions:

1. How does the global eddy-resolving model represent the mean state, seasonal and inter-annual variability on the South-East Greenland shelf? (Chapter 2)

2. How do the overall model hydrography and circulation in South-East Greenland shelf compare with available observations (moorings, satellites data and ship campaigns)? (Chapter 2)

3. Which are the processes or mechanisms that influence the most the inter-annual variability observed on the east Greenland shelf? (Chapter 3)

4. Is the high-RES model configuration able to represent the shelf-forced and buoyancy-forced dynamics within the fjord? (Chapter 4)

5. Which are (and to which extent) the runoff properties that affect the most the circulation and the temperature and salinity of the fjord? (Chapter 4)

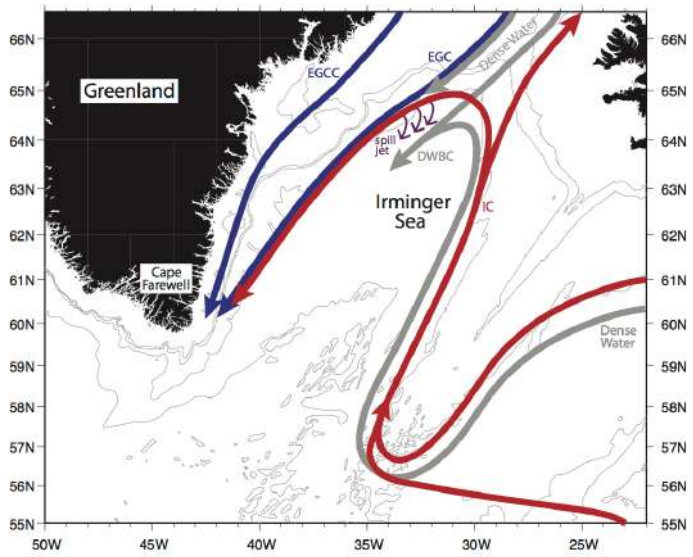

Figure 1.1: *Schematic circulation of the east Greenland boundary system from [9] (EGCC = East Greenland Coastal Current; EGC = East Greenland Current; IC = Irminger Current; DWBC = Deep Western Boundary Current).*

Chapter 2

Analysis of the South-East Greenland shelf mean state and seasonal variability with GLOB16 model

2.1 Introduction

The South-East (SE) Greenland shelf is characterized by the presence of the East Greenland boundary current system, a complex system of currents ranging from the inner shelf of SE Greenland to the base of the continental slope, as shown in Fig. 1.1.

In this region the Arctic-origin, fresh and cold East Greenland Current flows southward along the shelf-break next to the Atlantic-origin, salty and warm Irminger Current. The EGC merges with the recirculating portion of the Irminger Current to form a single flow that is often referred to as the East Greenland/Irminger Current or slope current. On the inner shelf the EGCC, possibly branching from the EGC south of the Denmark Strait or further upstream, advects cold, fresh water equatorward towards Cape Farewell [10].

Offshore, at the base of the continental slope, the Deep Western Boundary Current (DWBC) advects the dense recently ventilated overflow water equator-ward.

The DWBC is formed by the Denmark Strait Overflow Water (DSOW) and Iceland Scotland Overflow Water (ISOW), and have a fundamental impact on the

circulation in the Irminger and Labrador seas, which are active sites of deep-water formation [15].
The EGCC is a major conduit of freshwater from the Nordic Seas and high Arctic into the North Atlantic (e.g. [10], [16]) and, even though the existence of the EGCC is well-established, there remains various uncertainty regarding the current characteristics and fate.
Also the origin of the coastal current remains uncertain. Bacon et al. (2008) [17] suggests that Arctic sea ice is a major source of freshwater for the coastal current. Moreover, a coastal current has been identified north of Denmark Strait: this was later confirmed by Havik et al. (2017) [18].
Only summertime freshwater transport estimates are available for the EGCC along the shelf, and they range from 10 mSv to 100 mSv, while summertime estimates of the EGCC volume transports span across 0.5-2.0 Sv ([19], [4], [10], [11]).
It is of critical importance to determine the fate of the freshwater in the EGCC considering the potential impacts on the dynamics downstream. The Labrador Sea is a major site of convective overturning that influences the stratification of the subpolar North Atlantic, and the surface freshwater distribution in the Labrador Sea affects the ability for the convection to occur. Hence, it is important to determine the sources and timing of freshwater to the interior Labrador Sea.
Additionally, the variability of the East Greenland Coastal Current hydrography plays a major role on the stability of the Greenland ice sheet by leading warm Atlantic Water to enter Greenland's outlet fjords [3]. Indeed, the water masses that can be found in Greenland's glacial fjords exhibit a two-layer stratification and are composed of two distinct water masses: a warm, Atlantic-origin water (AW) and a colder, polar origin water (PW) [20].
The hypothesis is that the interaction of these two water masses advecting southward in the East Greenland Current intrude in Greenland's outlet glacial fjords and in turn influences the entering heat content [20]. A more complete understanding of the hydrographic variability in the East Greenland Coastal Current is important for assessing both fresh water transport along the Greenland shelf and investigating shelf-fjord exchange.
The study presented in this chapter makes use of a high-resolution model (with horizontal resolution of about 4 km in the region of interest) based on NEMO ocean model [21], in order to shed light on the variability and evolution of the

currents progressing along the east Greenland shelf.
In this chapter, we aim to advance our understanding of the dynamics, water mass variability, and transport of the East Greenland boundary current system as it progresses along the SE Greenland shelf. The analyzed model output starts in January 2008 and ends in December 2017. Specifically, we aim to answer the following questions:

1. How does the model represent the mean state and seasonal variability on the South-East Greenland shelf?

2. How do the overall model hydrography and circulation in South-East Greenland shelf compare with available observations (moorings, satellites data and ship campaigns)?

3. Is the observed variability in the OSNAP campaign well captured by the model?

The chapter is organized as follows: in section 2, the key features of the eddy-resolving configuration are presented, as well as the observational dataset used in the region of interest. In the third section an overview of the mean state and seasonal variability of the currents is resented, and a comparison between the model and different observational dataset in shown. The focus will be on the variability of temperature, salinity and currents. Summary and discussion will follow in the last section.

2.2 Model specification and datasets

2.2.1 The GLOB16 configuration

The CMCC GLOB16 is a a global, eddying configuration of the ocean and sea ice system based on version 3.4 of the Nucleus for European Modeling of the Ocean (NEMO) ocean model [21]. The model configuration is described in detail by Iovino et al. [22] and will only be outlined here.
The ocean component OPA is a finite difference, hydrostatic, primitive equation ocean general circulation model, coupled with the Louvain-la-Neuve sea ice model (LIM2). The model makes use of a nonuniform tripolar grid. The horizontal grid has a $1/16°$ resolution at the equator, corresponding to 6.9 km that increases poleward as cosine of latitude, resulting in total 5762 x 3963 grid points (Fig. 2.1).

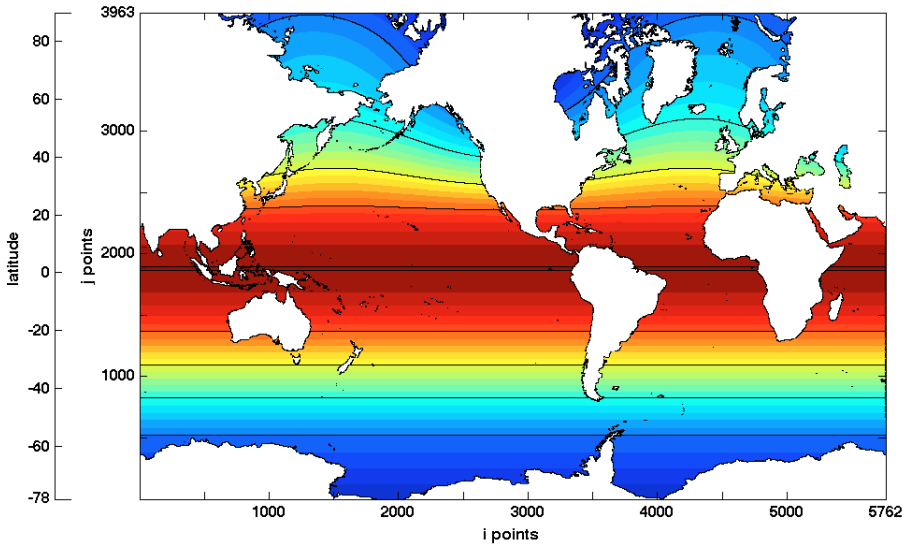

Figure 2.1: *GLOB16 meridional resolution, increasing poleward as cosine of latitude on a tripolar grid.*

Eddies are considered explicitly modeled when the horizontal grid points that describe them are more or equal then two. Since over the SE Greenland shelf the Rossby radius is around 7 km [23], while the model resolution in that region is less than 4 km, here the resolution is barely sufficient to resolve mesoscale eddies. However, vertical stratification over the shelf also plays a critical role in defining

the value of Rossby radius, that changes greatly over the shelf on seasonal timescales.

In the vertical, the model contains 98 levels from the surface to a maximum of 6000 m, and layers increase in thickness from 0.8 m at the surface to 144 m at the bottom; for instance, 29 levels cover the first 100 m.

The simulations analyzed are started from a state of rest in January 1975, with initial conditions for temperature and salinity derived from the World Ocean Atlas 2013 set of climatologies (WOA13; [24], [25]). The model is forced by the Japanese 55-year Reanalysis based dataset for driving ocean-sea ice model (JRA55-do version 1.3, [26]]), with 55 km spatial resolution and 3-hourly output. The model makes use of CORE bulk formula in order to compute surface boundary condition fields. No restoration on SST or SSS is applied. The output is analyzed within the decade January 2008 to December 2017; this time period is chosen in order to allow the analysis of both inter-annual and seasonal variability of water masses on the SE Greenland shelf. The output files are generated as 1 day averages and are then averaged into monthly means without changing the horizontal or vertical resolution.

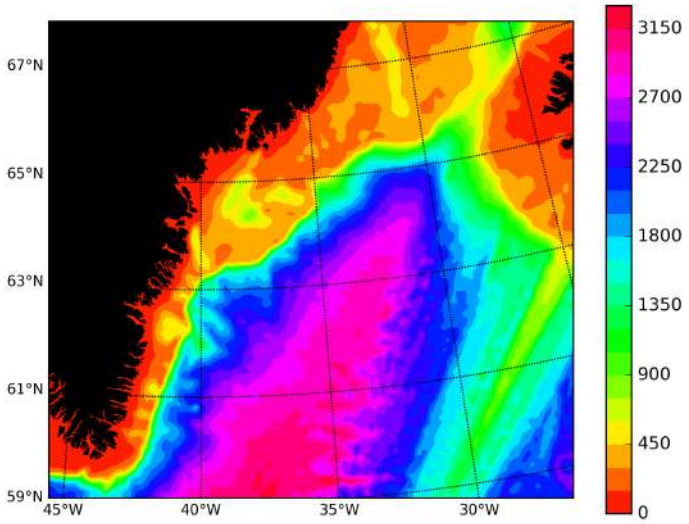

Figure 2.2: *GLOB16 bathymetry in the region of interest (in meters).*

To generate annual cycles, the ten years of monthly mean model output are further averaged into mean months. To compare seasonal differences mean calendar months are averaged into spring (JFM), summer (AMJ), fall (JAS) and winter (OND) seasons. The region of interest and the relative GLOB16 bathymetry is presented in Figure 2.2: lateral boundaries were chosen to have a comprehensive view of the boundary current system on the East Greenland shelf, from Denmark Strait to south of Cape Farewell.

2.2.2 Observational datasets

In this section, the observational datasets that have been used to validate the mean fields and seasonal variability of the model are presented and described.

Advanced Very High Resolution Radiometer

The Advanced Very High Resolution Radiometer (AVHRR) Pathfinder Version 5.3 L3-Collated (L3C) sea surface temperature has been used [27]. The AVHRR multi-purpose imaging instrument is used for global monitoring of cloud cover, sea surface temperature, ice, snow and vegetation cover characteristics. It is an across track scanner that senses the Earth's outgoing radiation from horizon to horizon in six channels (three solar channels in the visible-near infrared region and three thermal infrared channels), with a spatial resolution of 1km at nadir.

Overturning in the Sub-polar North Atlantic Program

The Overturning in the Sub-polar North Atlantic Program (OSNAP) consists in an observing system for sustained trans-basin measurements in the sub-polar North Atlantic [28]. The main goal of the program is to gain a better understanding of the Atlantic meridional overturning circulation (AMOC), an essential component of the global climate system that plays a fundamental role in establishing the mean climate state and its variability on inter-annual to longer time scales, as it is responsible for 25% of the total poleward heat transport in the northern hemisphere [29].

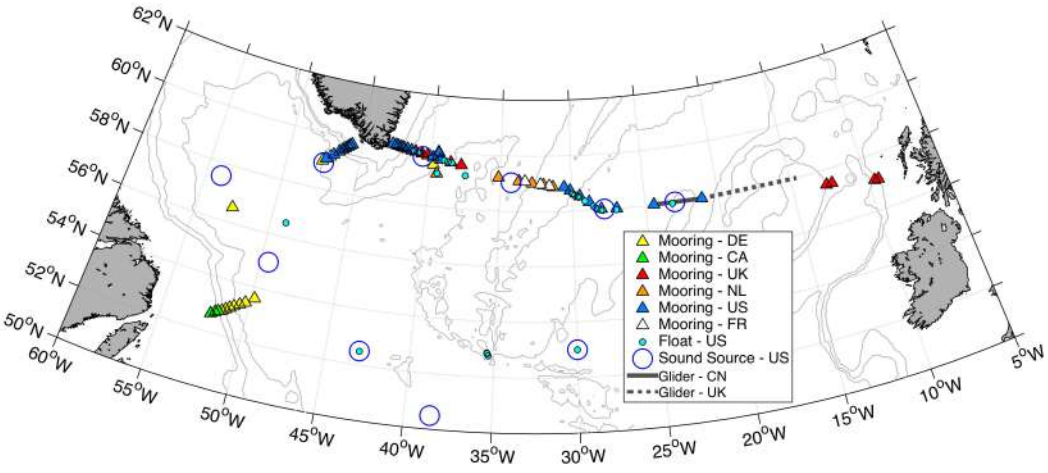

Figure 2.3: *A comprehensive view of OSNAP instruments, extending from southern Labrador to south-western Greenland and from SE Greenland to the coast of Scotland.*

A deep understanding of the AMOC and its natural variability is crucial for identifying the mechanisms of climate variability and climate prediction on seasonal to decadal scales.
OSNAP, deployed in the summer of 2014, aimed to measure the full-depth mass fluxes associated with the AMOC as well as meridional heat and freshwater fluxes. OSNAP consists of two branches: OSNAP West extends from southern Labrador to south-western Greenland and OSNAP East from SE Greenland to the coast of Scotland (Fig. 2.3 and 2.4). The OSNAP moorings are complemented by other moorings from different experiments to enhance the ability of OSNAP in measuring the heat, mass, and freshwater fluxes in the subpolar North Atlantic and capturing the variability along the basins, as follows:

- Two of the four moorings that form the U.S. global Ocean Observatories Initiative (OOI) Irminger Sea node were placed along the OSNAP line;

- Moorings located on the Reykjanes Ridge are complemented by those from the French Reykjanes Ridge Experiments (RREX) [30] ;

- In the eastern basin, a suite of gliders measures properties across the Rockall-Hatton Basin and westward into the Iceland Basin.

Additionally, acoustically tracked deep floats (RAFOS) have been released on the OSNAP lines to study the connectivity of overflow water pathways between moored arrays. A comprehensive view of the profound and diverse set of instruments exploited in the program is in Fig. 2.4.

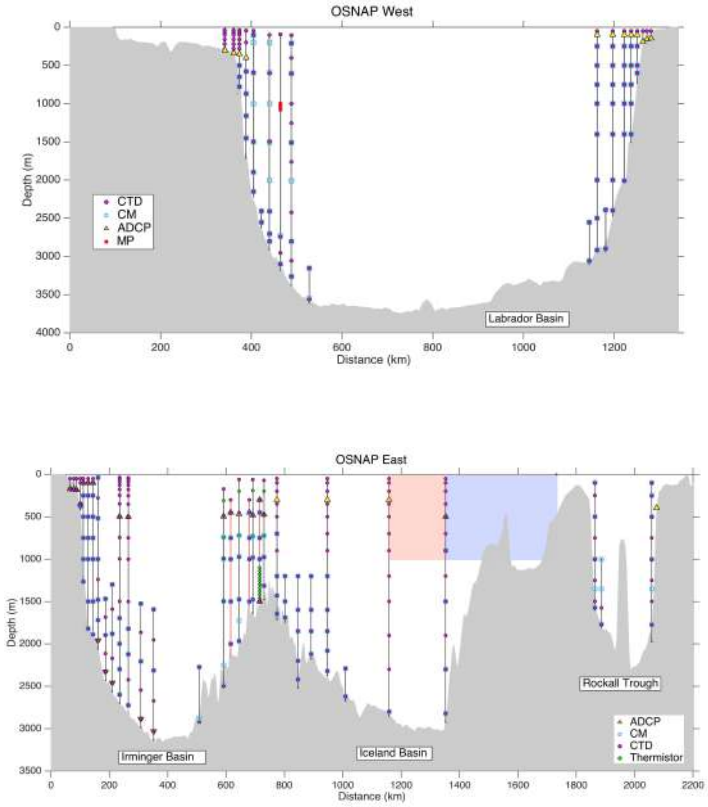

Figure 2.4: *Schematic of all the instruments deployed in OSNAP West and East from [28]. The instrument types are: thermistor, CTD, current meter (CM), ADCP, and moored profiler (MP). Glider domains are indicated by the pink and blue shaded box.*

2.3 Results

2.3.1 Mean state on South-East Greenland shelf

Mean velocity, temperature and salinity, depth-averaged in the layer 0-200m over the 2008-2017 period, are shown in Figure 2.5. Averaging the layer between 0-200m gives a comprehensive view of the surface-intensified currents along the SE Greenland shelf.
In Figure 2.6 the same fields are shown for the 200-400m layer, in order to capture the slope current running on the edge of the continental shelf. Figures 2.5a and 2.6a show three different currents, recognizable as the surface- intensified EGCC, the EGC that merges downstream of Sermilik fjord to form the EGC/IC, and the recirculating Irminger Current. The EGCC in the mean i is apparently emerging on the shelf around latitudes 67N - 68 N and it Is clearly distinct from the shelf-break flow of the EGC/IC. Further offshore, the EGC/IC shows onshore excursions around topographic features - e.g. Kangerdlugssuaq and Sermilik Troughs.
Model mean temperature and salinity (Fig. 2.5b,c and Fig. 2.6b,c] show warm and salty waters outside the shelf and cold, fresh water on the east Greenland shelf. The EGCC and EGC/IC flow along all the Greenland east shelf.

Specifically, Figure 2.5b shows 0-200 m average temperature, that exhibits a steep gradient between shelf and open sea. All over the SE Greenland shelf temperatures range between -2 °C and 1 °C indicating the presence of PW, while offshore we find temperatures that goes from 2°C to 7 °C. Maximum temperature are found concurrently with the IC recirculating from the Irminger Sea toward the SE shelf. Figure 2.6b shows the same pattern, even though temperatures on the shelf here are warmer, indicating the presence of AW. The same deductions can be made from salinity (Fig 2.5c and 2.6c): saline water is found far offhore at all depths, while on the shelf the mean salinity in the first 200 m is found to be around 33.5 psu, while from 200 m to 400 m is around 34 psu. This is due to the presence of the shelf of PW sitting above AW.

To infer the water mass properties and the variability as they travel southward, four different sections has been selected and analyzed. Starting from north, the first section is located approximatively at 66°N (section 'a' in Fig. 2.7), in order to encase the coastal current and to be far from topographic features (e.g. the

Kangerdlugssuaq Through). The second section is placed upstream of Sermilik fjord and downstream of Kangerdlugssuaq fjord, at 65°N (section 'b' in Figure 2.7). The third transect is located at around 63°N where the shelf narrows and where we can encase both the coastal and shelf current (section 'c' in Figure 2.7). The fourth section (section 'd') lies at Cape Farewell, at 61°N, where OSNAP measurements are available. The bathymetry of the chosen sections is shown in Figure 2.8. The mean speed, temperature and salinity at sections (averaged in the 2008-2017 period) are displayed in Fig. 2.9-2.12. In all the fours sections the front between the Atlantic and Arctic waters is distinguishable by the rapid transition from cold and fresh to warm and salty conditions and it is located at the edge of the continental shelf. The velocity field present two cores of velocities that are visible in all the four sections, indicating the presence of the EGCC and EGC/IC currents all over the shelf.

Figure 2.9 displays the 2008-2017 current (a), temperature (b) and salinity (c) fields for the southern-most transect near Cape Farewell. Associated with the

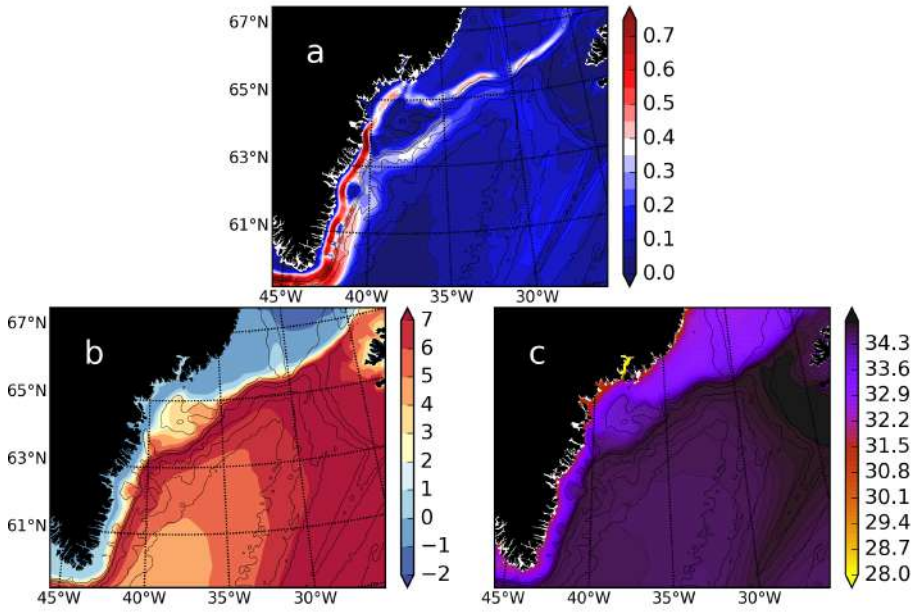

Figure 2.5: *Mean velocity (a), temperature (b) ans salinity (c) from GLOB16 output for the 2008-2017 period, averaged on 0-200m.*

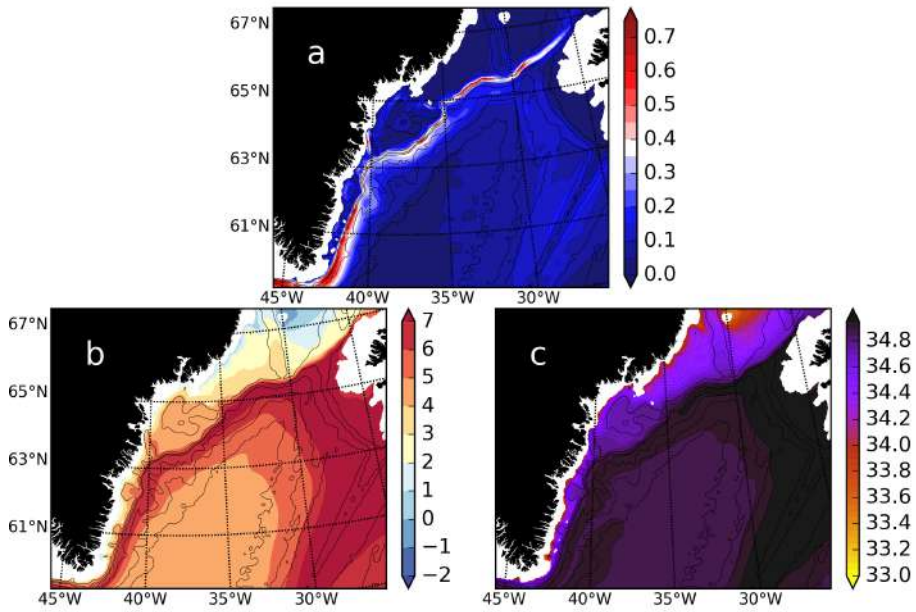

Figure 2.6: *Mean velocity (a), temperature (b) ans salinity (c) from GLOB16 output for the 2008-2017 period, averaged on 200-400m.*

low salinity wedge on the inner shelf, there is a distinct equatorward jet, with mean velocities around 60 cm/s. The surface flow associated with the slope current is found farther offshore: mean velocities here are more or less 50 cm/s with a core extending from the surface to 500 meter depth. The near vertical 34.6 psu isohaline (Fig. 2.9c)] helps to distinguish between the AW in the IC and the EGC waters. Inshore, a wedge of very fresh and cold water, with salinity < 33 psu and temperature < 3 °C is distributed over the shelf. This is the front associated with the EGCC. It is present a region of weak flow that separates the EGCC from the EGC velocity core. Just after the shelf-break and associated with the slope current, the temperature rises up to 4°C, due to the fraction of AW within the EGC/IC. Moving northward, section 'c' lies at about 63°N where the shelf reaches one of its narrowest point. There, the EGCC is pronounced, with mean velocities near the surface exceeding 80 cm/s, and near-bottom values up to 30 cm/s (Fig. 2.10a).

Here it is difficult to isolate the EGCC from the EGC/IC compared to the distinct

signature seen at section 'd' near Cape Farewell. The bathymetry plays a key role in shaping the structure of the current, the very narrow shelf steers the EGC/IC and EGCC to flow together. The enhanced equatorward flow on the slope (centered at 500 m) may also be formed by the East Greenland Spill Jet discussed e.g. by Pickart et al. (2005) [4], that have been observed at the same latitude, formed by dense waters cascading from the shelf.

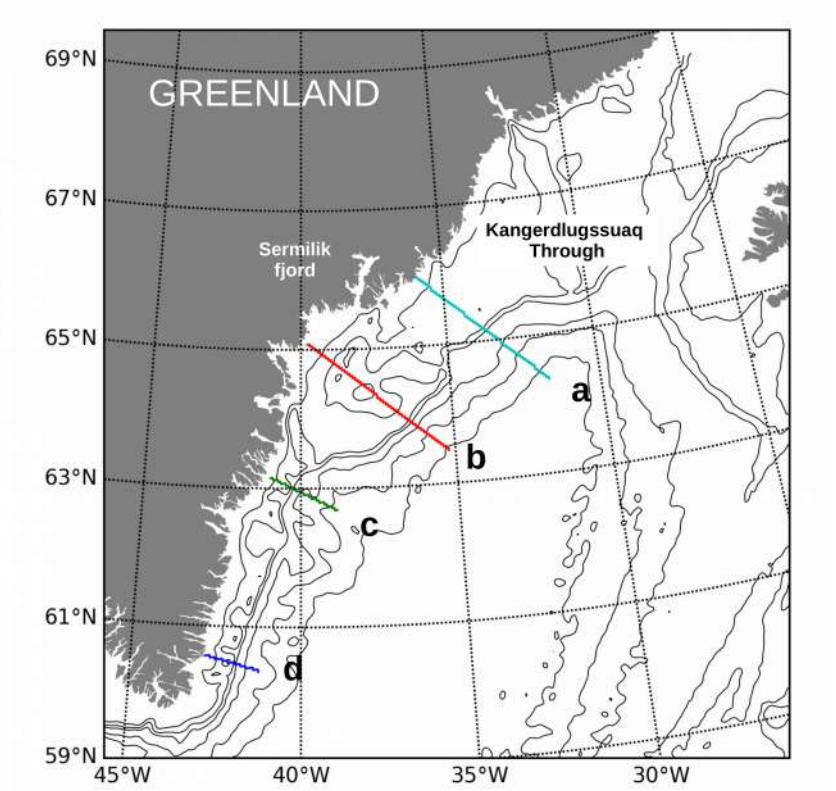

Figure 2.7: *Overview of chosen sections along the Eat Greenland Shelf. Black contours indicate topography. From north to south we can find section a (lightblue) ,b (red) ,c (green)and d (blue). Black lines indicates bathymetry contours. Sermilik fjord and Kangerdlugssuaq through are indicated.*

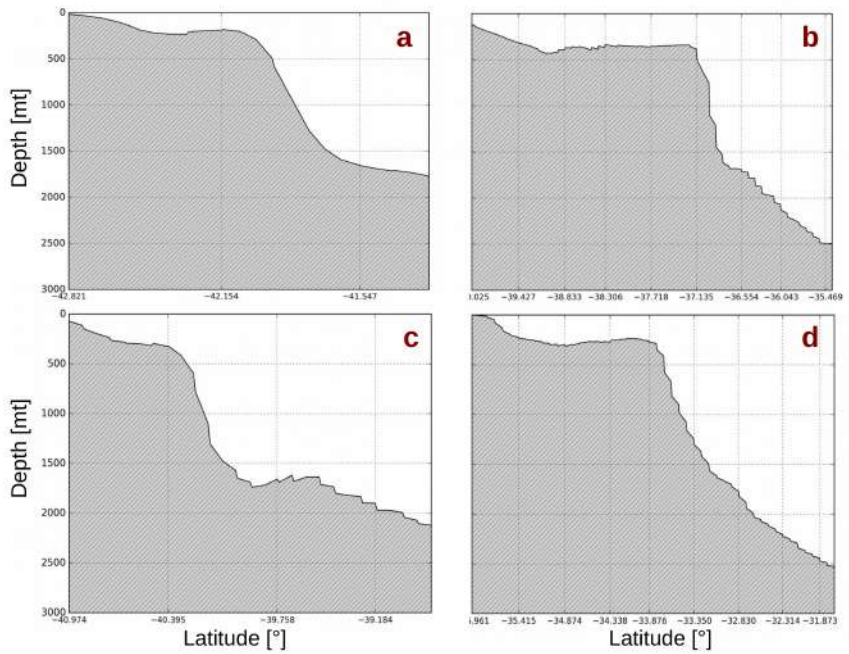

Figure 2.8: *From upper right to lower left: (a) 67°N section; (b) 65°N section; (c) 63.5°N section; (d) 61°N section bathymetry.*

At section 'b', located near 65°N, the shelf reaches one of its widest point. As in the other sections, we observed a fresh wedge of water indicative of the EGCC, with a mean velocity of 40 cm/s. In this case, the we can observe the core of the EGC/IC system detached and distinguishable from the EGCC (Fig. 2.11). A maximum in velocity (exceeding 50 cm/s) is found on the shelf-break at depth of 500 meters. This feature can also be attributed to the Spill Jet. The freshest water is the coldest and is found inshore over the shelf, but interestingly we also find salty and warm water also in the subsurface waters, far inshore of the shelf-break. This supports the notion of flow being diverted toward the inner shelf, bringing with it AW influence from the EGC/IC system.

Section 'a' is the northern-most section. Here, the mean velocity (Fig. 2.12a) shows two cores, the EGC/IC system and the EGCC, which are clearly separated and distinguishable, in conjunction to a third core most likely due to the shifting of the EGC/IC in time. A detailed description of this feature will be presented in the next section. The EGC is confined to a shallow depth extending for most

part of the shelf, and the strongest flow in the section occurs on the slope at about 500 m, associated with the Spill Jet. The salinity field has a large wedge of fresh water in most part of the shelf, associated with low temperatures (Fig. 2.12b,c).
At section 'd', the southerner-most located at Cape Farewell we compare the OSNAP results from the paper from Le Bras et al. 2018 [9]. Here they show the mean temperature salinity and velocity from a transect of mooring (from the OSNAP program) at Cape Farewell (Fig. 2.13). Since the OSNAP available dataset is from August 2014 to August 2016, a time-series for the same period is considered from the numerical simulation for a direct comparison (Fig. 2.14).
Both the EGCC and EGC/IC current are similar in magnitude and pattern between the observations and the modeled data. One difference is that the mean velocity in the model is higher by 0.1-0.2 m/s. Salinity and temperature on the shelf are well represented, while offshore surface temperatures are about 1°C warmer in GLOB16. Overall, the model can properly represent the mean features and the hydrology over the shelf and at the shelf-break at Cape Farewell. Another difference is that the core of the EGC/IC in the model extends from the surface towards 500 m deep caused by the different modeled bathymetry of the shelf in the region.

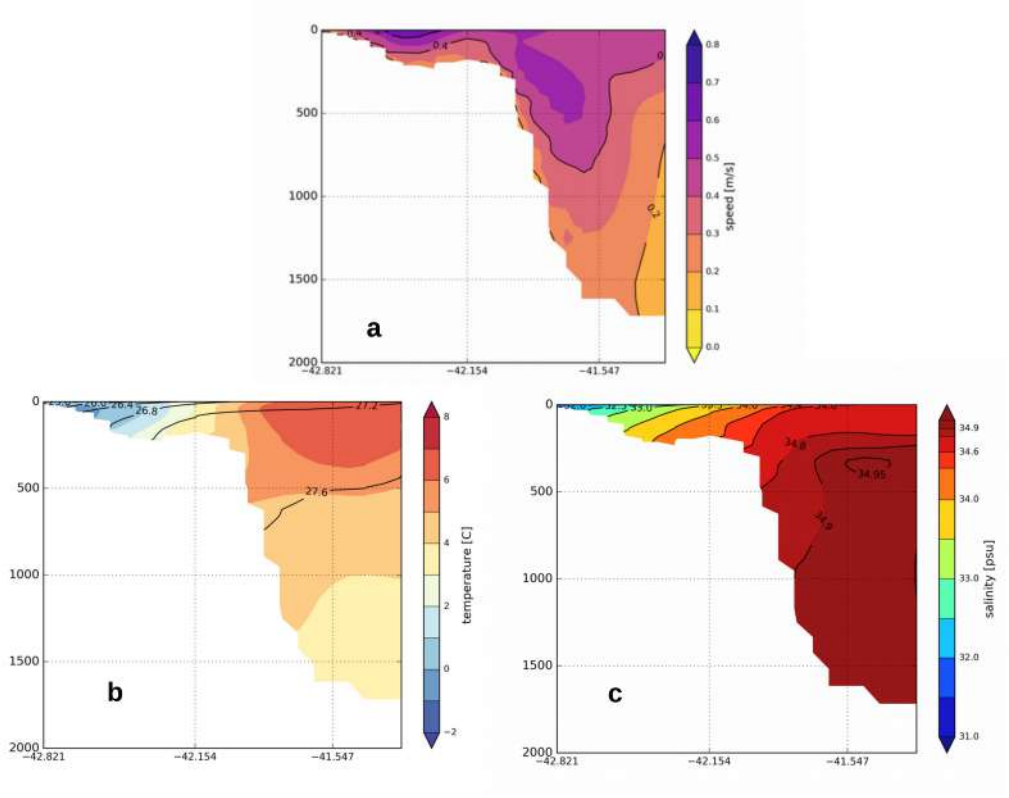

Figure 2.9: *Section 'd'. Cape Farewell 2008-2017 fields. From upper right to lower left: (a) mean velocity; (b) mean temperature (color), with selected isopycnals (kg/m^3) contoured in black ; (c) mean salinity.*

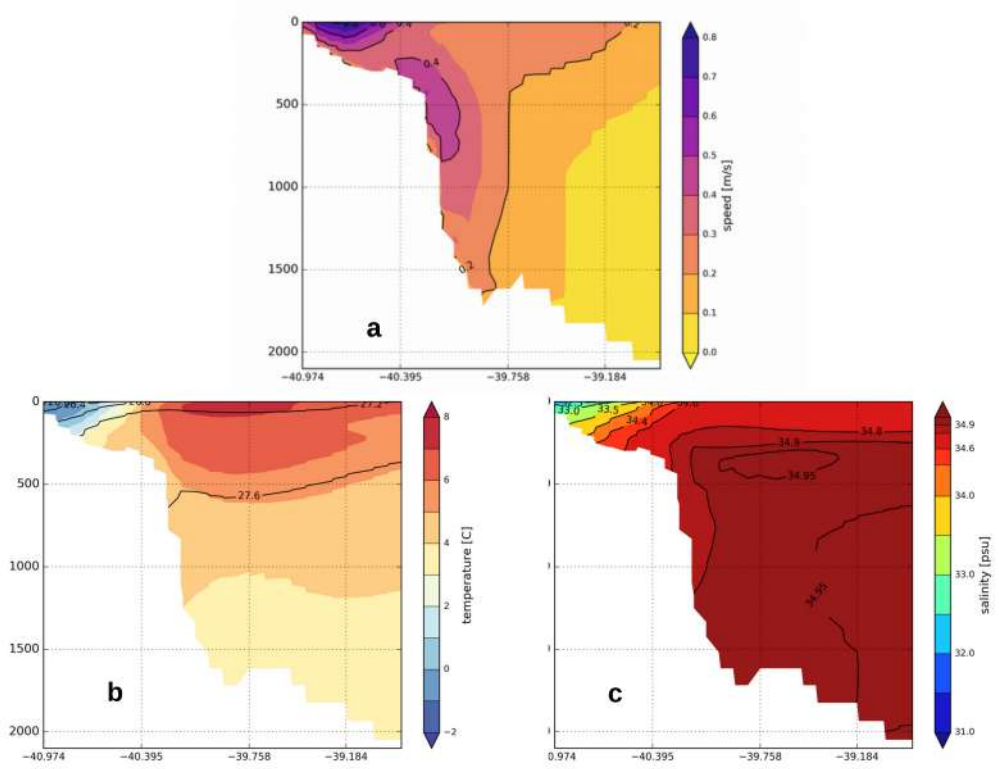

Figure 2.10: *Section 'c'. Cape Farewell 2008-2017 fields. From upper right to lower left: (a) mean velocity; (b) mean temperature (color), with selected isopycnals (kg/m3) contoured in black ; (c) mean salinity.*

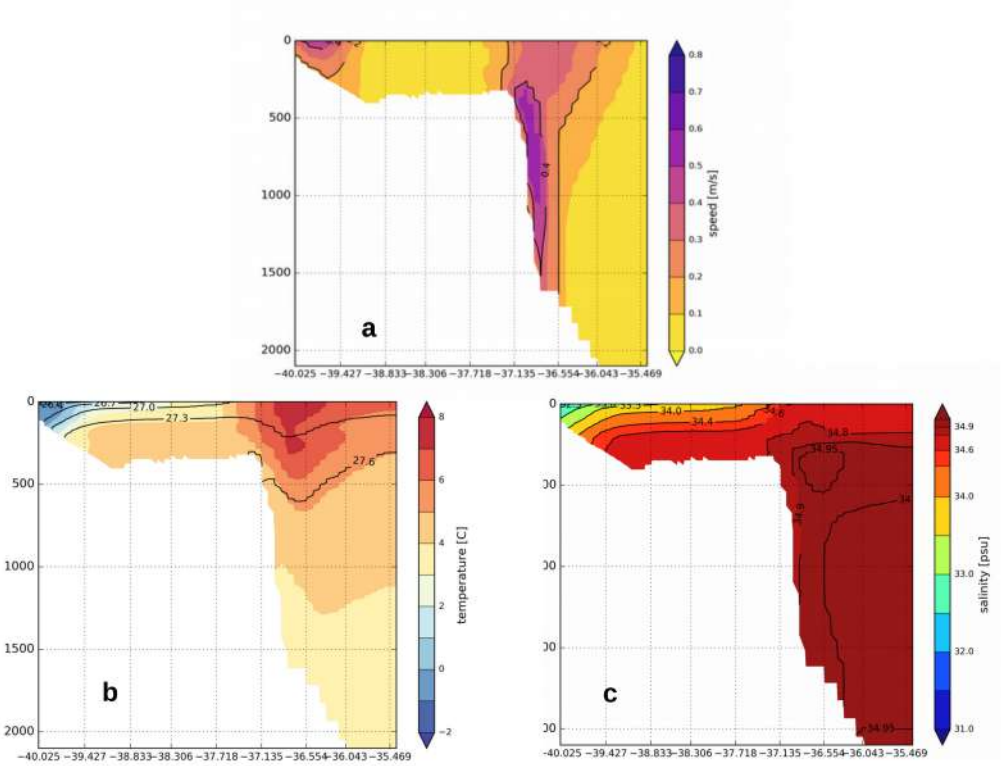

Figure 2.11: *Section 'b'. Cape Farewell 2008-2017 fields. From upper right to lower left: (a) mean velocity; (b) mean temperature (color), with selected isopycnals (kg/m^3) contoured in black ; (c) mean salinity.*

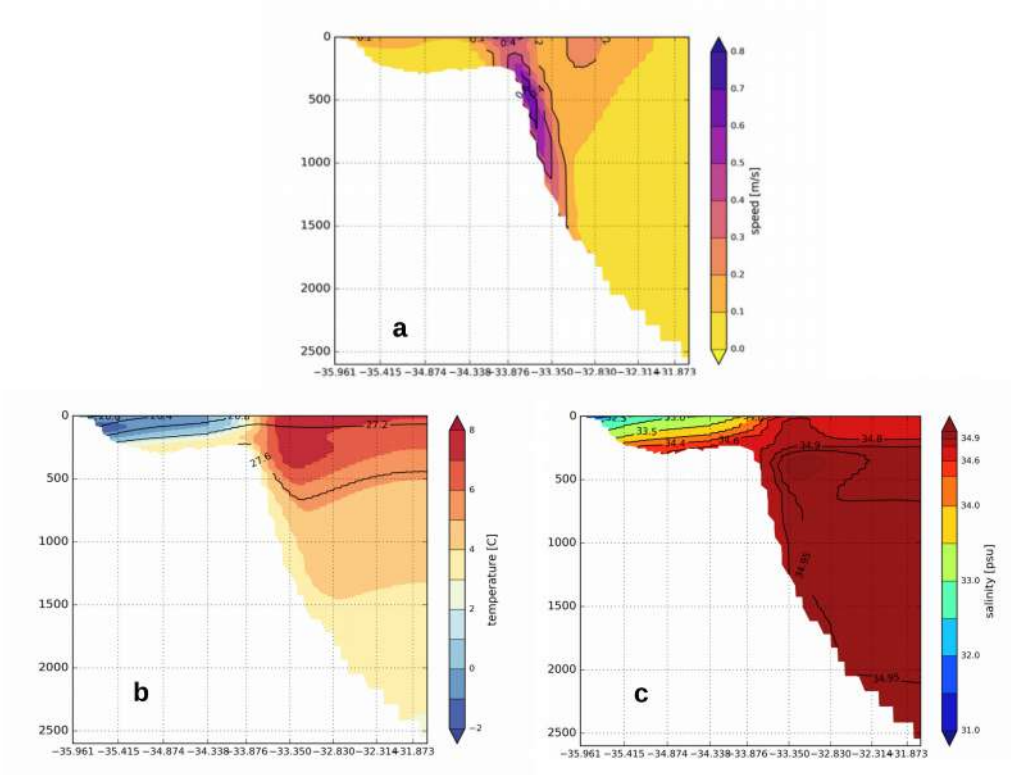

Figure 2.12: *Section 'a'. Cape Farewell 2008-2017 fields. From upper right to lower left: (a) mean velocity; (b) mean temperature (color), with selected isopycnals (kg/m^3) contoured in black ; (c) mean salinity.*

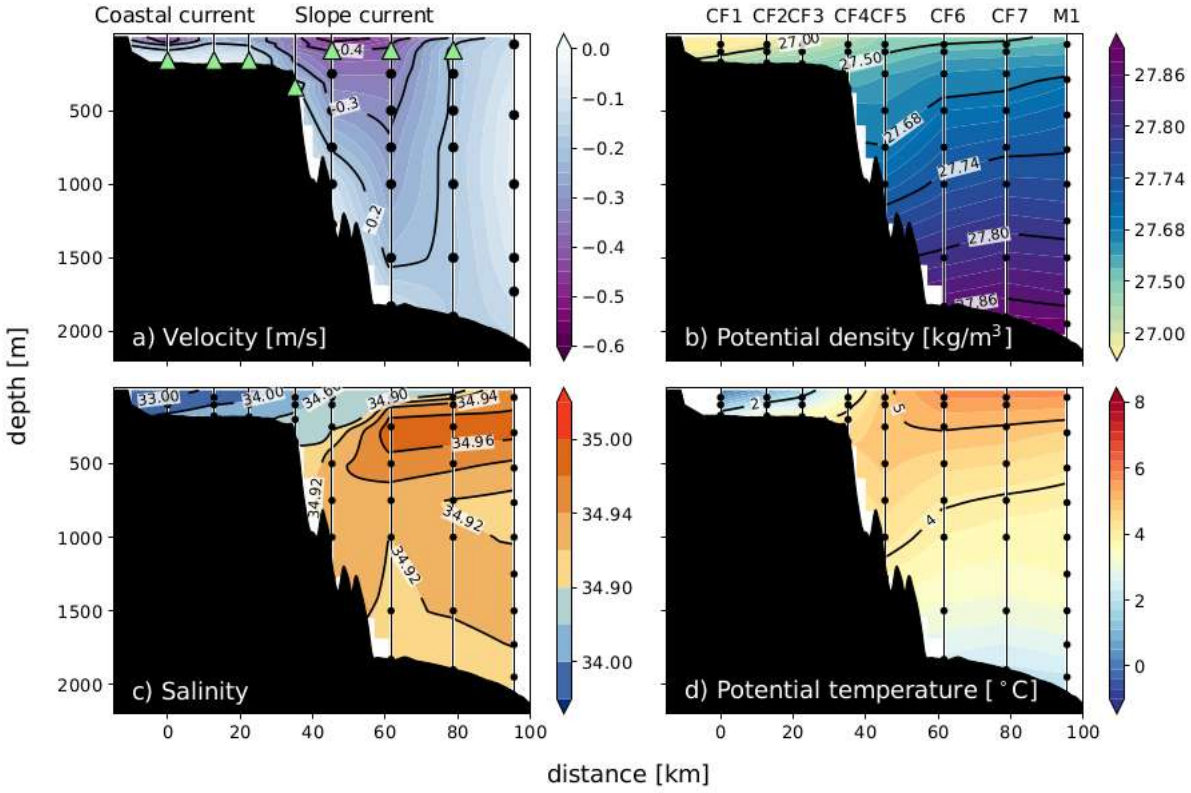

Figure 2.13: *P*lots from [9]. Time mean sections of a) along-stream velocity, b) potential density, c) salinity and d) potential temperature based on the OSNAP Cape Farewell mooring data from the first full year.

A T-S diagrams is presented in Figure 2.15 for the climatological mean of the four different section described above. In the climatological mean, the four sections exhibit a similar behavior in the T/S space. From literature (e.g. [10]), along the SE Greenland shelf, the water masses that originally derive from the Arctic are classified into three water masses: Polar Intermediate Water (PIW), Polar Surface Water (PSW), and warm Polar Surface Water (PSWw).

- PIW: $\rho > 1027.70$ kg/m3 and T < 0 °C;
- PSW : $\rho < 1027.70$ kg/m3 and T < 0 °C;
- PSWw: PSW that melting sea ice warms and freshens.

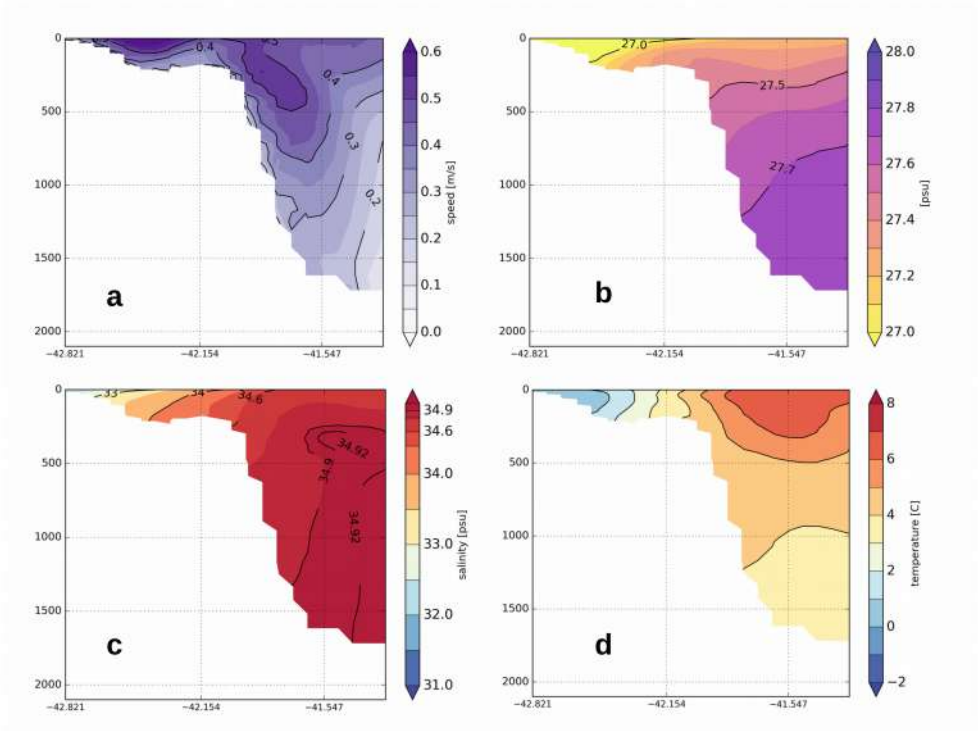

Figure 2.14: *P*lots from [9]. Time mean sections of a) along-stream velocity, b) potential density, c) salinity and d) potential temperature based on the OSNAP Cape Farewell mooring data from the first full year.

In the modeled T/S, we will consider all water masses colder than 2°C and fresher than 32 psu as Polar Water (PW); those waters are the ones found inshore closest to the coast. Offshore, we expect the EGC/IC current to include the water mass historically identified to as Irminger Sea Water and having temperature of 4-5 °C and salinity of ∼35 psu, and the Northeast Atlantic Water, which lies in the interior of the basin, with temperature warmer than 7°C and salinity higher than 35 psu [10]. In this work, we refer to all the Atlantic-influenced water as Atlantic Water (AW), characterized by T $>$ 4.5°C and S $>$ 34.8 psu.
The T-S diagram in Figure 2.15 show the properties of the climatological mean (2008- 2017) for temperature and salinity, and highlights the signature of both the PW and the AW on the shelf and the shelf-break. Maximum temperatures are around 6-8 °C with salinities $>$ 34.8 psu while coldest water masses have a

temperature lower than 0 °C with salinity that ranges from 31.5 to 33.5 psu. We observe that the water masses (AW and PW), even though they exhibit the same properties in the four sections, show more mixing as they flow along the shelf from north to south.

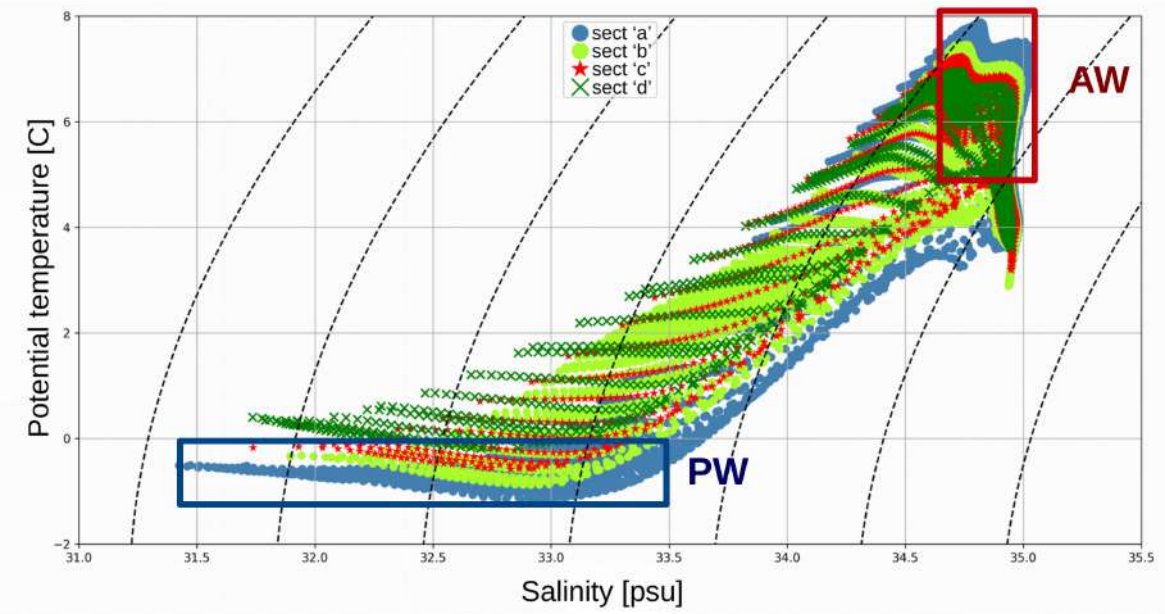

Figure 2.15: T/S diagram for the SE shelf, distinguished by section (see legend). Shaded black lines indicate isopycnal contours.

Regarding the volume and freshwater transport at different latitudes of the East Greenland Coastal Current, there have been some measurements sparse in time, since it has been discovered (e.g. [4], [10], [31], [11]), and their results are presented in Tables 2.1 and 2.2 It is worth to note that all the measurement of the currents via ship have been collected during the summer period, facilitate by the absence of sea ice on the shelf, so there are no available observational records of the current properties that cover the entire year. One exception is the

OSNAP dataset, that will be presented later in the discussion. In this paragraph we will show the climatological mean for the EGCC velocity simulated by the model (Table 2.3) and the results of all the available measurement conducted from 2005 till 2014 summarized in Tables 2.1 and 2.2. In order to compute the volume and freshwater transport of each current from the model output, we needto define a criteria to define the lateral and depth boundaries of the EGCC and EGC/IC currents. Different definitions have been used in the past to delineate the EGC based on hydrography: for example [32] used the 34.9 isohaline to distinguish the EGC from the IC, while [10] set it at 34.8. Using these past studies as a guide, we use the 34.9 isohaline to mark the boundary between the EGC and IC, even though comparison with diverse reference salinities have been made, and do not result in significant differences in the freshwater transport. In order to define the EGCC as a distinct feature from the EGC, here we use a similar method to the one used in [10], namely as a function of velocity field. Specifically, we define the lateral limits by where the velocity decreases to 15% of the maximum inner jet velocity and the depth limit to be where the 34.9 isohaline touches the ground.
Following the above criteria, the climatological (2008-2017) mean of freshwater and volume transports at the four sections is presented in Table 2.3. While a comprehensive study of the transport seasonality is presented in Sect. 2.3.2.
Using these definition criteria for defining the currents boundaries, we computed the volume transport to be: and the freshwater transport to be:

$$V_t = \iint_{-H}^{0} v_{perp} dx dy \tag{2.1}$$

$$FW_t = \iint_{-H}^{0} v_{perp}(1 - S/S_0)) dx dy \tag{2.2}$$

where S_0 is the reference salinity, that has been chosen to be 34.9 psu. With this comparison we observe that the model is able in reproducing the right magnitude of both volume and freshwater mean transport. Accordingly with observations, the transports increase flowing southward from section 'a' until section 'd'. This difference in transport come from various branches of EGC/IC feed the EGCC recirculating on the shelf.

In order to validate the the temperature obtained from the output of the model, a comparison between the Sea Surface Temperature (SST) from the AVHRR

	60°N (CF)	61°N	63°N	65°N	66°N (DS)
Bacon et al. 2002	**0.86±0.12**	X	X	X	X
Wilkinson and Bacon 2005	**1.07**	**1.54**	**0.46**	X	**0.27**
Holliday et al. 2007	X	X	X	X	**1.3**
Sutherland and Pickart 2008	**0.6**	X	**1.4**	**0.9**	**0.9**
Harden et al. 2014	X	X	X	X	**0.66±0.18**
Lin et al. 2018	**1.28±0.33**	X	X	X	X

Table 2.1: Volume transport estimates of the EGCC, between Denmark Strait (DS) and Cape Farewell (CF), from the available literature (see first column). Errors are written when available. All values here are in Sverdrup for the volume transport and in mSv for the freshwater transport. References: [4], [10], [11], [19], [33], [34], [31].

	60°N (CF)	61°N	63°N	65°N	66°N (DS)
Bacon et al. 2002	**60 ± 12**	X	X	X	X
Wilkinson and Bacon 2005 (5% vol. transp.)	**55**	**77**	**23**	X	**13**
Harden et al. 2014	X	X	X	X	**42 ± 12**
Sutherland and Pickart 2008	**60**	X	**90**	**60**	**40**
Lin et al. 2018	**74 ± 5**	X	X	X	X

Table 2.2: Freshwater transport estimates of the EGCC, between Denmark Strait (DS) and Cape Farewell (CF), from the available literature (see first column). Errors are written when available. All values here are in Sverdrup for the volume transport and in mSv for the freshwater transport. References: [4], [10], [11], [19], [33], [34].

EGCC	60°N (CF)	61°N	63°N	65°N (DS)
Mean volume transport (Sv)	2.05 ± 0.7	2.36 ± 0.43	1.36 ± 0.43	0.17 ± 0.21
Mean freshwater transport (mSv)	67 ± 19	86 ±16	53 ±18	10 ± 12

Table 2.3: Volume and freshwater transport estimates of the EGCC from GLOB16 model in the different sections

dataset is here shown and compared to SST from GLOB16 (Figure 2.16 a,b). The advantage of satellite data is that, in a region where collecting data is a challenge, it can give us an estimate of SST all over the SE Greenland shelf for the whole year. Observed mean temperature ranges from -1 °C on the shelf to the 5 °C of the recirculating Irminger current. The SST on the shelf is uniformly colder and the SST outside is uniformly warmer. Modeled mean SST show the same pattern, however the model exhibit a steeper shelf-ocean gradient: temperature goes from -1.8°C on the shelf to around 8°C outside. We can conclude that climatological mean is well represented by GLOB16 in all its features, distinguishing the shelf from the Irminger Sea Interior even though the model accentuates the differences in temperature.

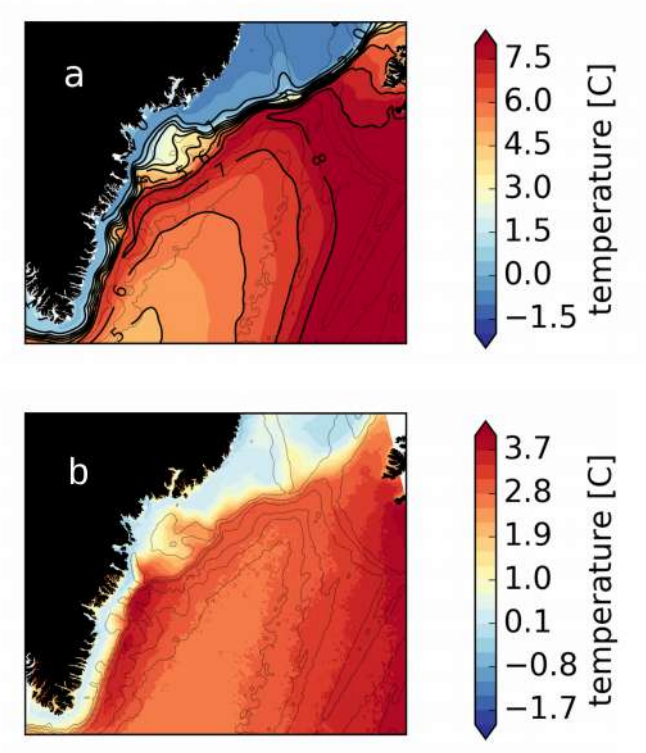

Figure 2.16: *G*LOB16 (a) and AVHRR (b) mean SST for the period 2008-2017. The two color-bar are different to better capture each variability.

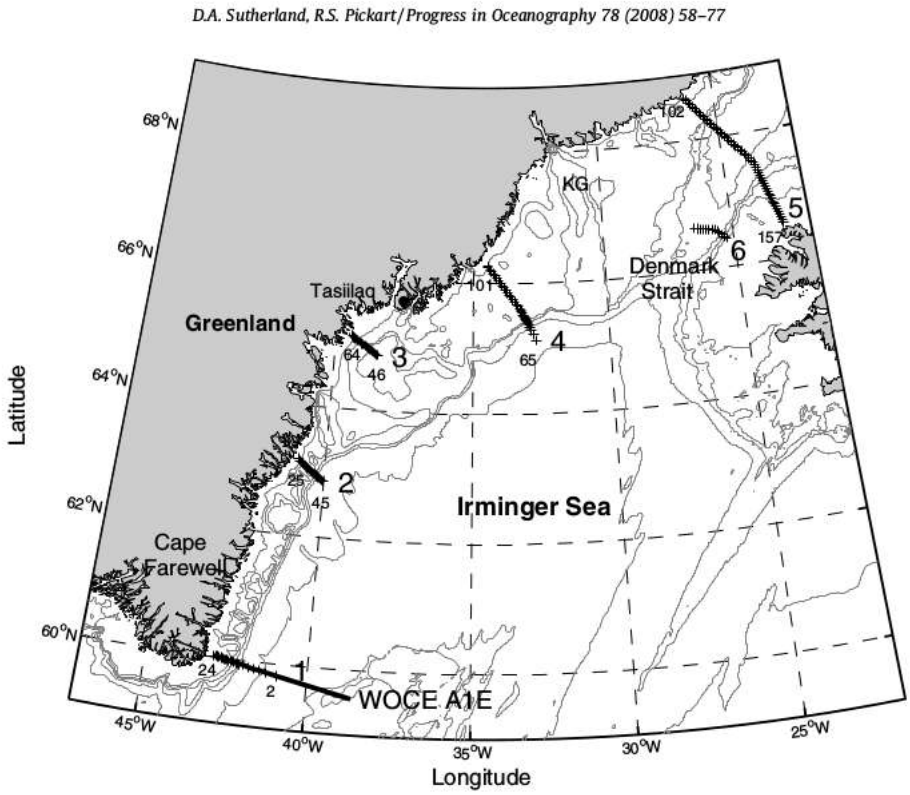

Figure 2.17: *F*igure from [10]. Five locations where the observations were taken in the summer of 2004.

In order to evaluate the modeled progression of the currents along the shelf, a useful method is the comparison between the modeled output and the fields obtained during the summer 2004 campaign by Sutherland and Pickart [10], that provided the first comprehensive description of the EGCC. The decade of the model (2008-2017) is different, so the following comparison is just qualitative, but having a 10 years reliable dataset allows us to answer questions on the temporal (seasonal, inter-annual) and spatial variability of the EGCC and the entire shelf circulation.

The Sutherland and Pickart' 2008 dataset is composed by five sections along the SE Greenland continental shelf, as can be seen in Figure 2.17 and the resulting salinity and current fields for summer 2004 are show in Figure 2.18. They have

shown that the EGCC exists along the entire shelf, distinct from the shelf- break EGC, with a high velocity core (from 50 to 100 cm/s) and with low-salinity and a wedge-shaped structure. The single exception they found was near 63°N, where the shelf narrows considerably and the EGC comes into close proximity with the EGCC. We observed the same behavior in summer in our model (Fig. 2.19), indeed the EGCC is seen in all the sections in summer, associated with low-salinity and cold water. Similarly, where the shelf narrows we see similarly a merging of the EGCC and EGC, as expected. The model is overall slightly saltier all over the shelf, but the currents have the right order of magnitude. From this comparison we can conclude that the model is reliable in representing the currents properties in summer along the shelf.

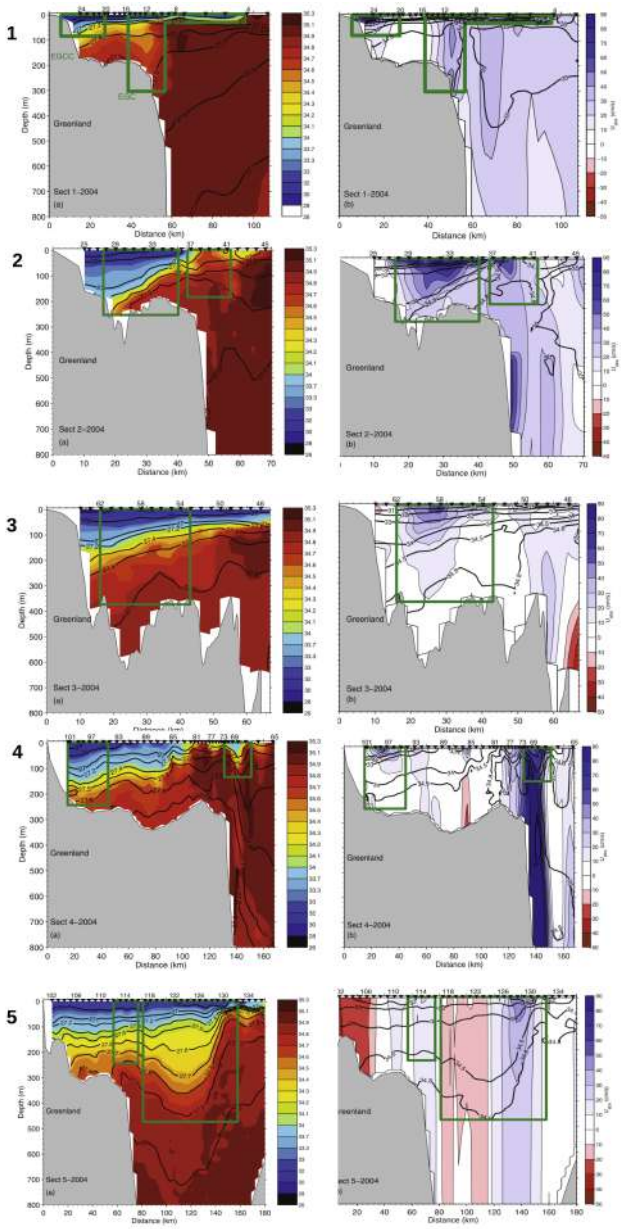

Figure 2.18: *F*rom upper to lower panel: Sections 1,2,3,4,5 from Sutherland et al. 2008 [10]. The first column shows the salinity field while the second column shows the U-component of velocity. Green boxes are the lateral and depth boundary of the EGCC and EGC currents as defined in the paper.

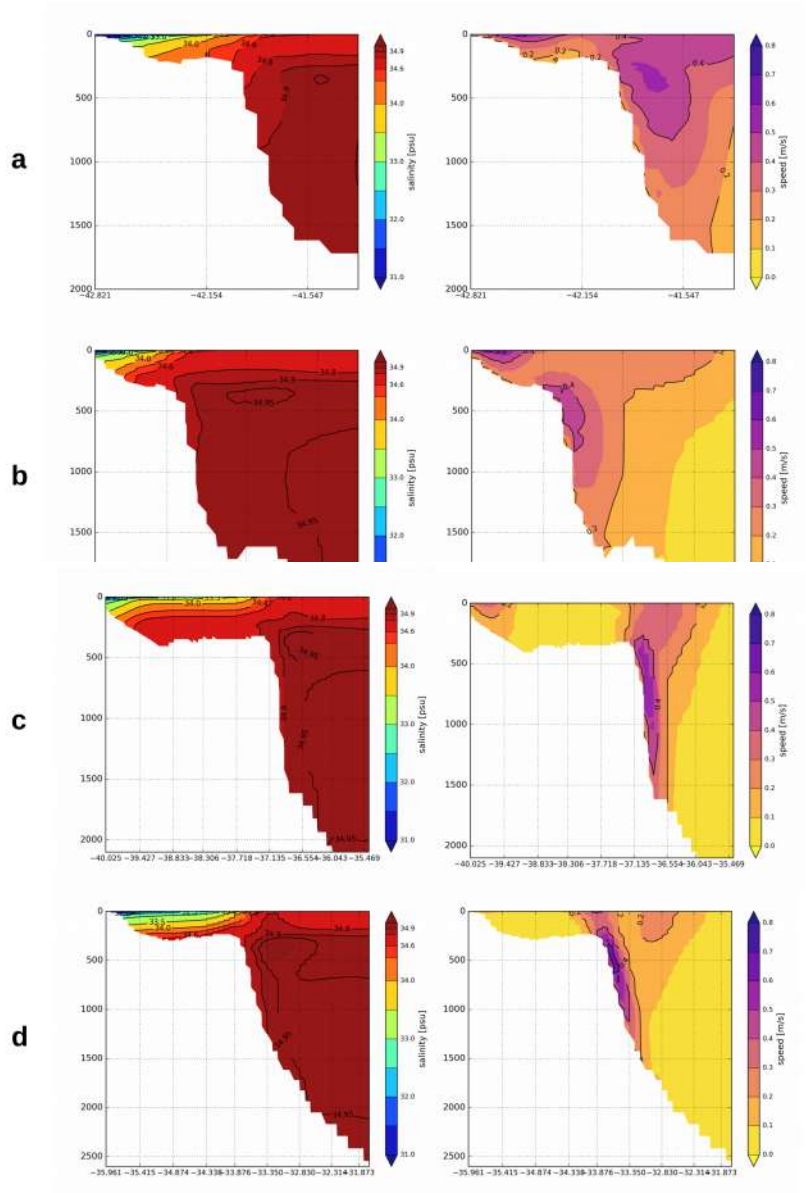

Figure 2.19: *F*rom upper to lower panel: Sections 'a','b','c','d'. The first column shows the salinity field while the second column shows the velocity component perpendicular to the section.

2.3.2 Seasonal variability on South-East Greenland shelf

In this section the seasonal variability of the boundary current system is described. Firstly, the seasonal anomalies over the 2008-2017 period are computed by averaging over the same depth range as the one shown in the previous section, namely 0-200 m and 200-400 m, to highlight the surface-intensified currents and the slope current running on the edge of the continental shelf.
Figure 2.20 shows the velocity seasonal anomalies for spring (AMJ), summer (JAS), fall (OND) and winter (JFM), averaged within the 0-200 m layer for the 2008-2017 period. In Figures 2.21 and 2.22, seasonal anomalies for temperature and salinity are presented, for the same depth range and period.
The same fields are shown as mean within the 200-400 m depth range (Fig. 2.23, 2.24 and 2.25), to capture the features of the slope current running on the edge of the continental shelf. EGCC velocity anomalies show two different pattern in winter/summer and in spring/fall.
In winter and summer the signature is a clear speeding/slowing of the EGCC and concurrently of the fraction of the EGC/IC current that have a component coming from the recirculating Irminger Current. On the other hand, in spring and fall, the EGCC speed is lower and higher respectively, and the anomaly appears to emerge north of Sermilik fjord (Fig. 2.20) On-shelf anomaly salinities show two clear patterns in the winter/summer and in spring/fall.
In summer, a band of high-salinity water is found all over the shelf, progressively increasing and going to the inner part.
In winter, the signal ha the same pattern but opposite magnitude: a fresh band is found on the East Greenland shelf. Spring and fall show instead a two-core pattern with opposite salinity anomalies: one north of Kangerdlugssuaq Through and the other one on the shelf outside the Sermilik fjord.
In summer and fall (JAS, OND), on-shelf and off-shelf temperatures are uniformly higher than average, with a slight increase in temperature toward the south and in the Sermilik Through. In winter and spring (JFM, AMJ), temperatures are colder than average in the entire domain of interest.
To address if modeled seasonal temperature fields are well represented and support a reliable representation of the current system hydrography, a comparison between our model Sea Surface temperature (SST) and available satellite observations is

here presented.

Climatological seasonality is well represented by the model: both in the observations and in the model winter and summer [(b) and (d) of Figure 2.26 and 2.27 have the uniformly cold and warm anomalies in the whole region. The magnitude of modeled summer and winter anomalies is comparable to the observed ones. The overall behavior of spring and summer anomalies [(c) and (e) of Figure 2.26 and 2.27 is well represented on the shelf: the pattern of the simulated anomalies resembles the pattern of the AVHRR data.

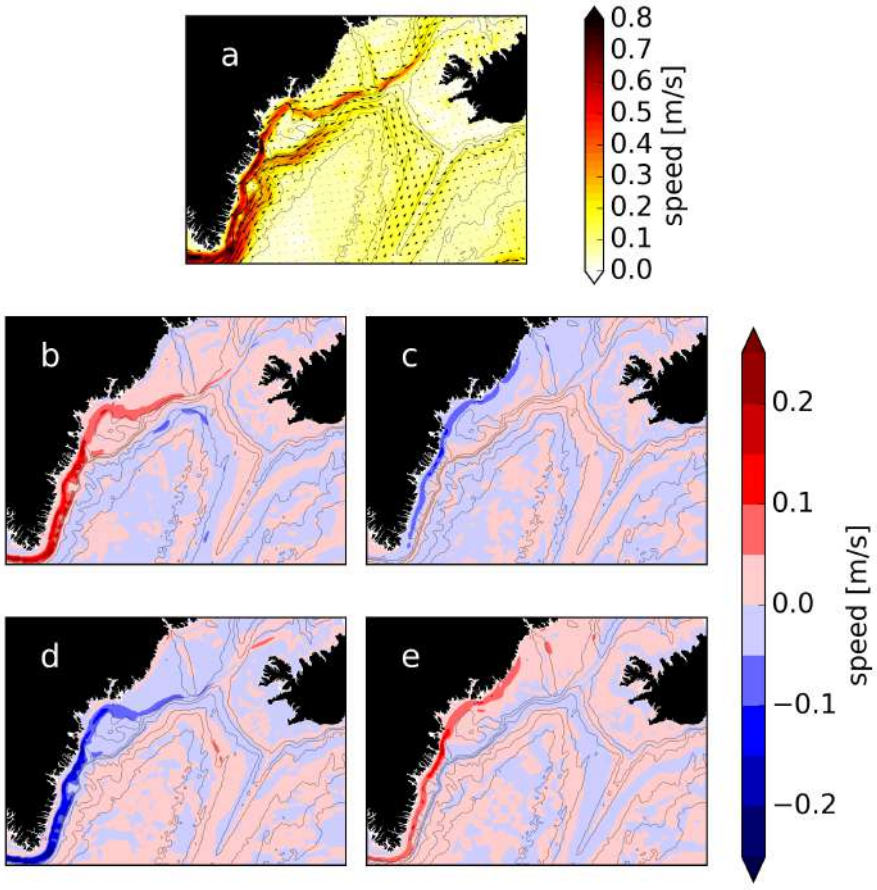

Figure 2.20: *M*ean speed (a), winter anomalies (DJF, b), spring anomalies (MAM, c), summer anomalies (JAS, d) and fall anomalies (OND, e). Each plot is 0-200 mt averaged for the period 2008-2017.

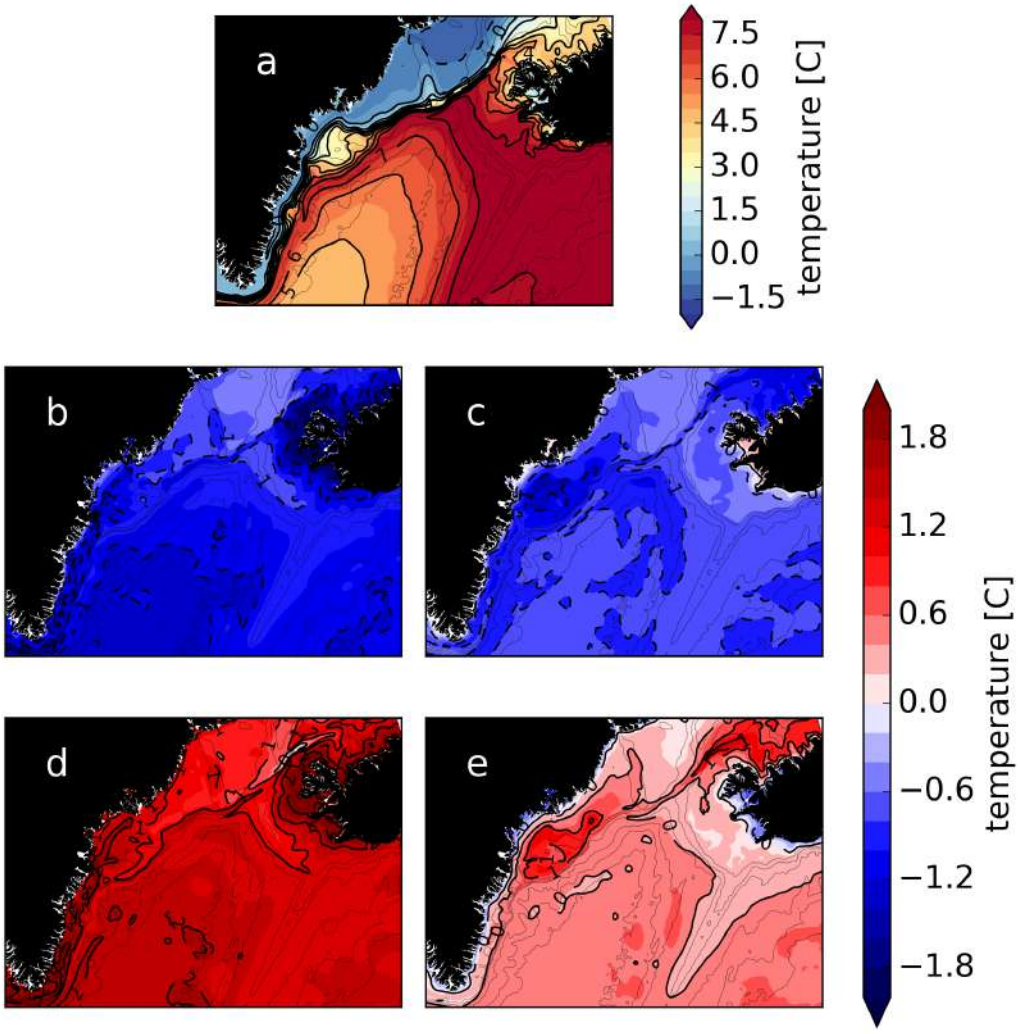

Figure 2.21: *M*ean temperature (a), winter anomalies (DJF, b), spring anomalies (MAM, c), summer anomalies (JAS, d) and fall anomalies (OND, e). Each plot is 0-200 mt averaged for the period 2008-2017.

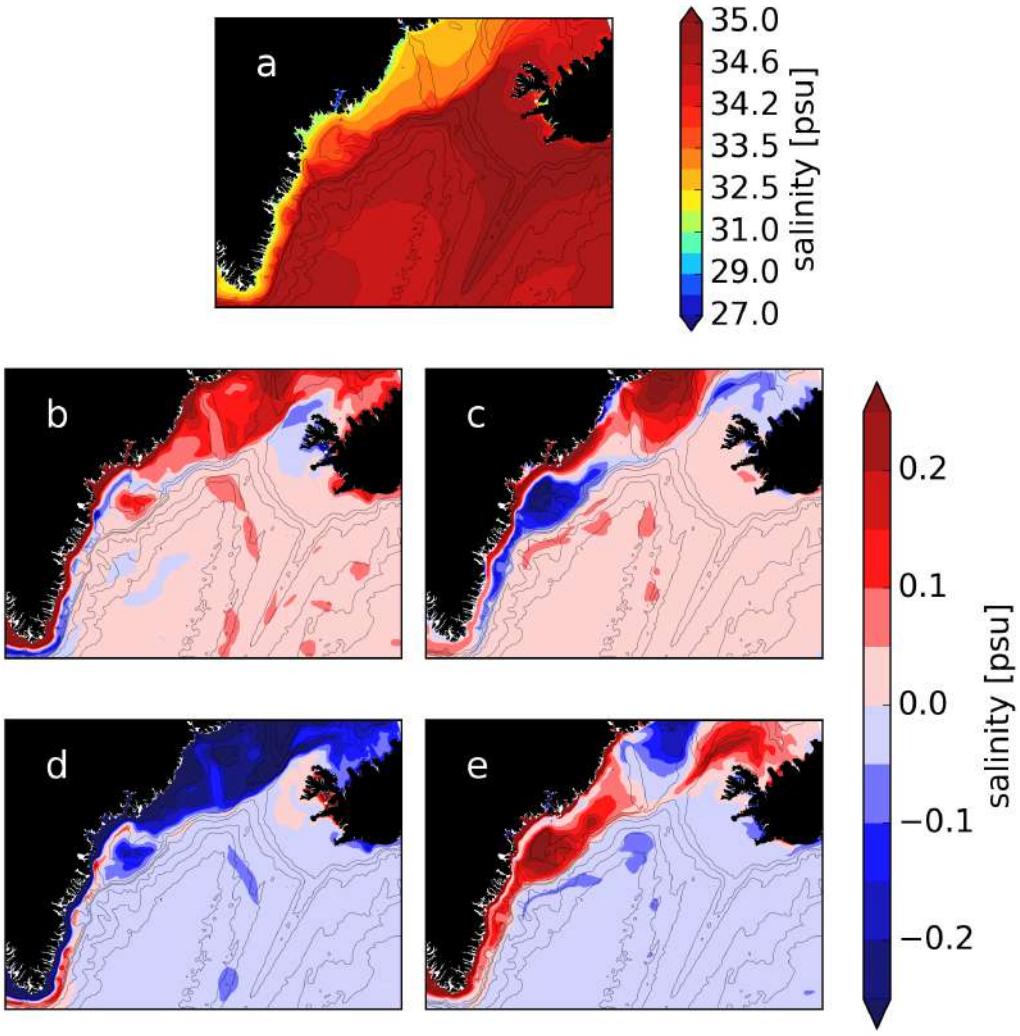

Figure 2.22: *M*ean salinity (a), winter anomalies (DJF, b), spring anomalies (MAM, c), summer anomalies (JAS, d) and fall anomalies (OND, e). Each plot is 0-200 mt averaged for the period 2008-2017.

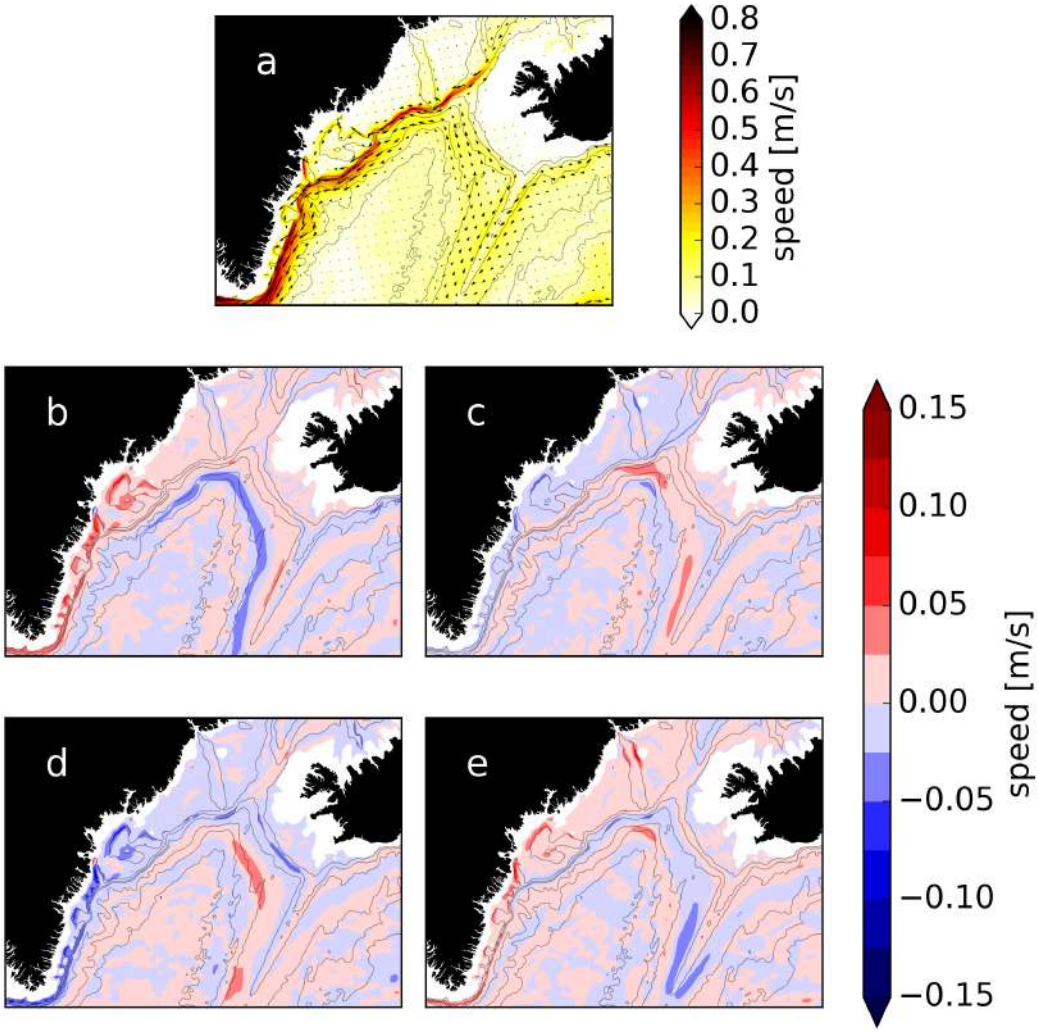

Figure 2.23: *M*ean speed (a), winter anomalies (DJF, b), spring anomalies (MAM, c), summer anomalies (JAS, d) and fall anomalies (OND, e). Each plot is 200-400 mt averaged for the period 2008-2017.

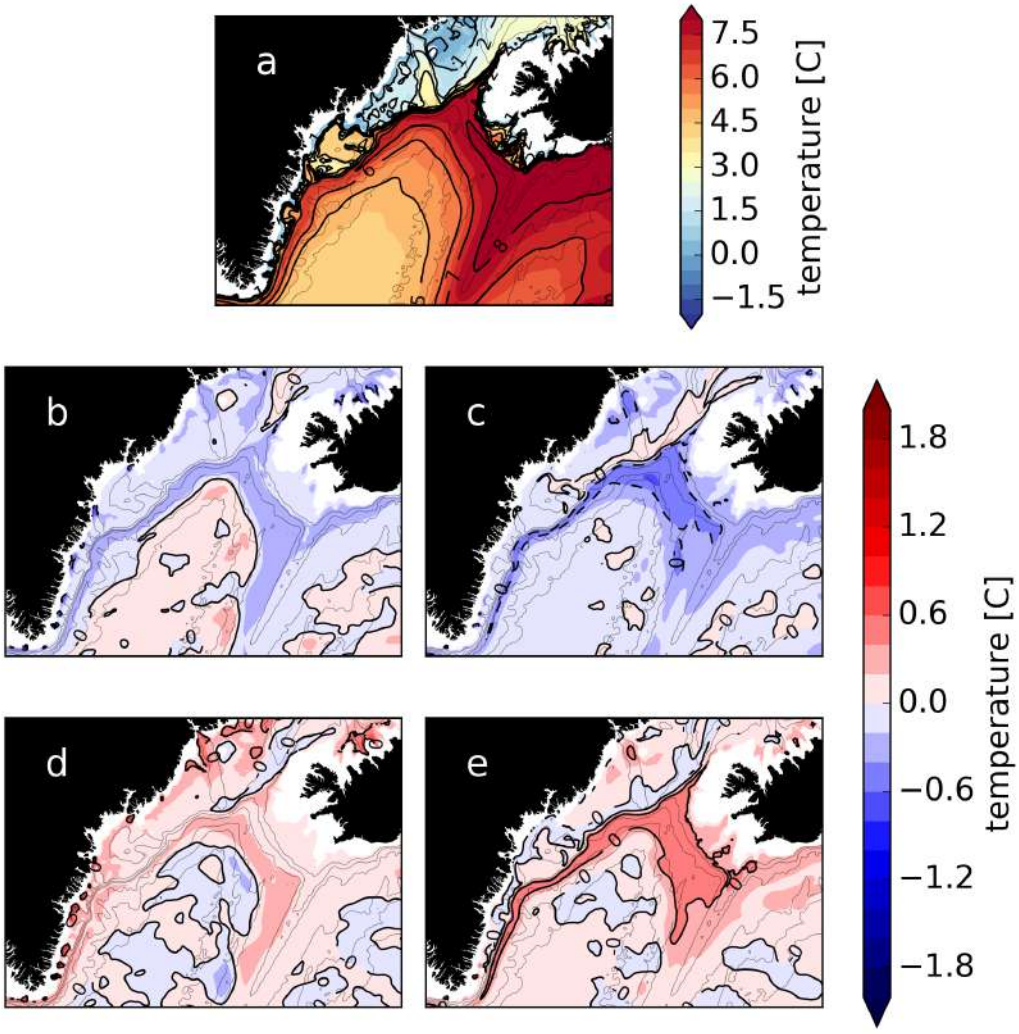

Figure 2.24: *M*ean temperature (a), winter anomalies (DJF, b), spring anomalies (MAM, c), summer anomalies (JAS, d) and fall anomalies (OND, e). Each plot is 200-400 mt averaged for the period 2008-2017.

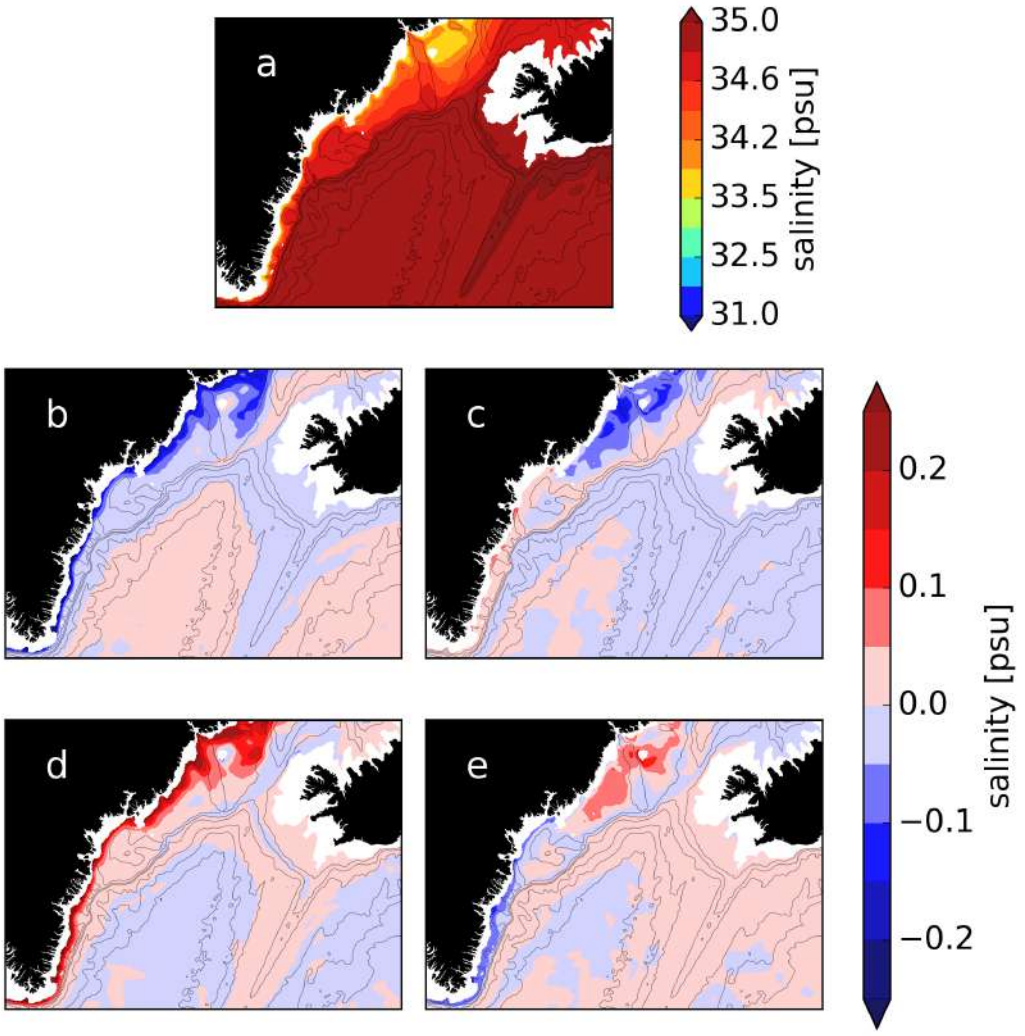

Figure 2.25: *M*ean salinity (a), winter anomalies (DJF, b), spring anomalies (MAM, c), summer anomalies (JAS, d) and fall anomalies (OND, e). Each plot is 200-400 mt averaged for the period 2008-2017.

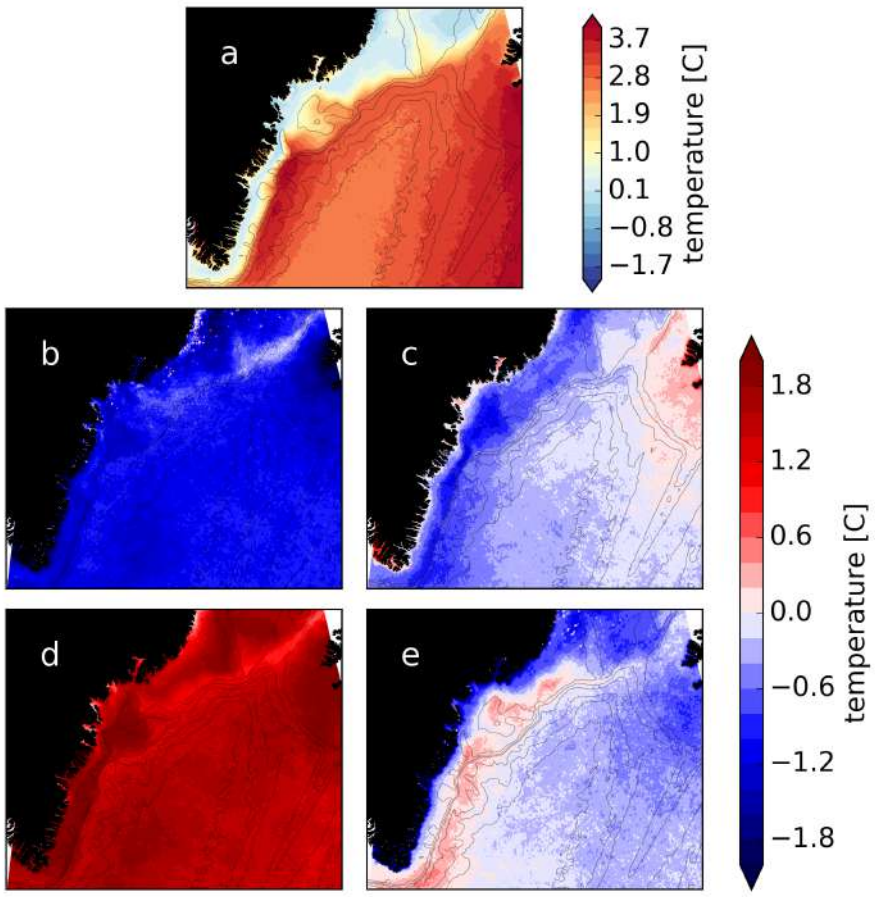

Figure 2.26: *A*VHRR mean SST (a), winter anomalies (DJF, b), spring anomalies (MAM, c), summer anomalies (JAS, d) and fall anomalies (OND, e). Each plot is averaged for the period 2008-2017.

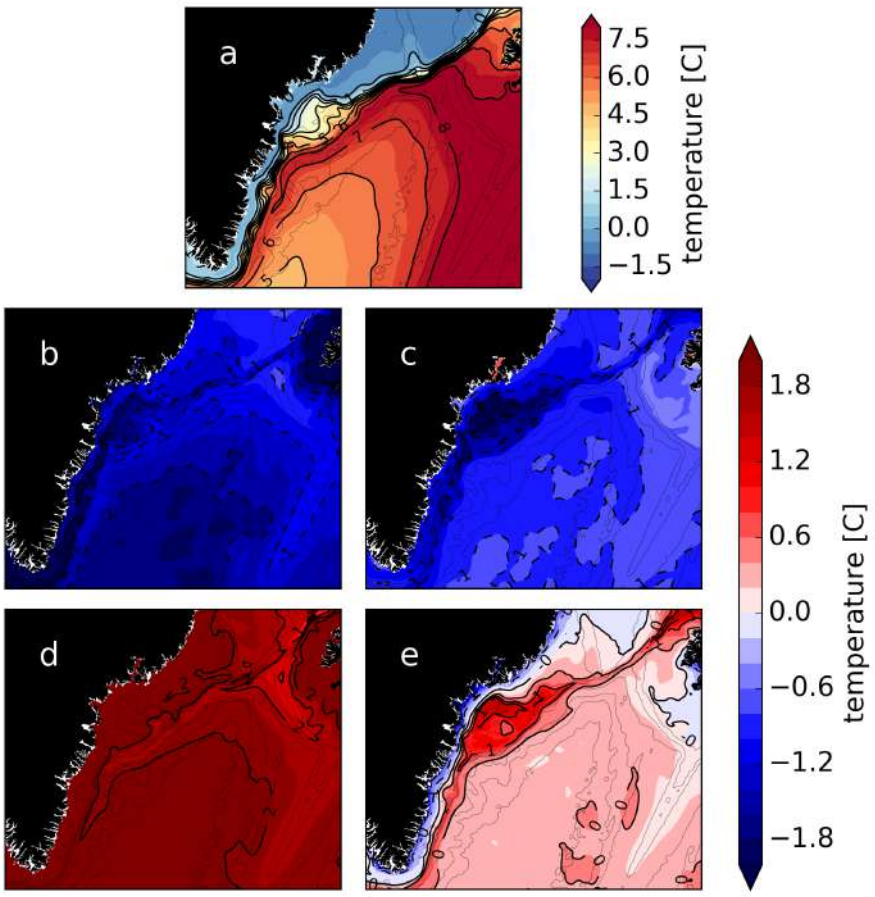

Figure 2.27: *M*odeled mean SST (a), winter anomalies (DJF, b), spring anomalies (MAM, c), summer anomalies (JAS, d) and fall anomalies (OND, e). Each plot is averaged for the period 2008-2017.

Nevertheless model temperature magnitude differ from observations: they appear stronger in all seasons and in particular in both spring and fall (up to 1 °C). In the following paragraphs the seasonal analysis in the four different sections (as in Fig. 2.7) is presented. It is worth noting (Fig. 2.28) that the current seasonal anomalies are not bigger than 4 cm/s resulting in more or less the 5-10% of the actual currents, leading to small differences in the current velocities through the year.

In Figure 2.28 we can see that, in spring and summer and in both the southern sections 'd' and 'c', the EGCC exhibits a slow down and an inshore shift, while

in winter and fall the current speeds up, moving offshore. Section 'b' lies where the continental shelf has one of its widest location. The EGCC current here is located far inshore and it's detached from EGC/IC. Also here the EGCC looks slowed down in spring and summer and sped up in winter and fall. In summer, it extends down within all the water column, while in fall is confined at the surface. In the northern-most section 'a', the seasonal signal is similar to the mean structure (see Fig. 2.12), even though a little bit less marked than in the other sections: Figure 2.28 indicates that the current is slower during spring and summer, but faster in winter and fall.

The EGC/IC pattern in section 'd' at Cape Farewell shows a slow down in winter and fall and a speed up in spring and summer. This seasonal signature can be seen along all the water column and the magnitude of this anomalies is similar in all the seasons. In section 'c' the anomalies of the EGC/IC show a slowing in summer and fall, and a speeding up in the other two seasons. The EGC/IC current anomalies in section 'b' and 'a', the northern-most, the EGC/IC pattern is more complicated. The two core of anomalies observed in the sections (e.g. spring in section 'a') can be explained by a shifting or expanding/shrinking of the current. Indeed we observed a two core velocity in Section 2.3.1 regarding the EGC/IC, hypothesized to be due to a shift in the current. Here the anomalies support this hypothesis, showing in the positions of the enhanced equator-ward flow the opposite anomalies. The temperature field presents a surface anomaly in all the sections (Fig. 2.29), warm in summer and fall, and cold in spring and winter. Since the EGCC is surface- intensified, those are the anomalies that the current carries equator-ward. Other temperature anomalies that can be seen are smaller than 0.3 °C and become significant only in summer and winter on the shelf, where the water appears to be respectively colder and warmer than usual. This suggests that in summer (winter) there is more (less) intrusion of AW on the shelf. Maximum seasonal salinity anomalies are about 0.1 psu. In all sections, we can observe an equal but opposite behavior between summer/winter and spring/fall. The EGCC in summer and spring in all sections moves saltier water than the mean current. While in winter and fall, it exhibits a freshening. In winter, also the waters on the shelf exhibit a freshening, while in fall it is not clearly seen. This suggests an enhanced intrusion of AW on the shelf during summer.

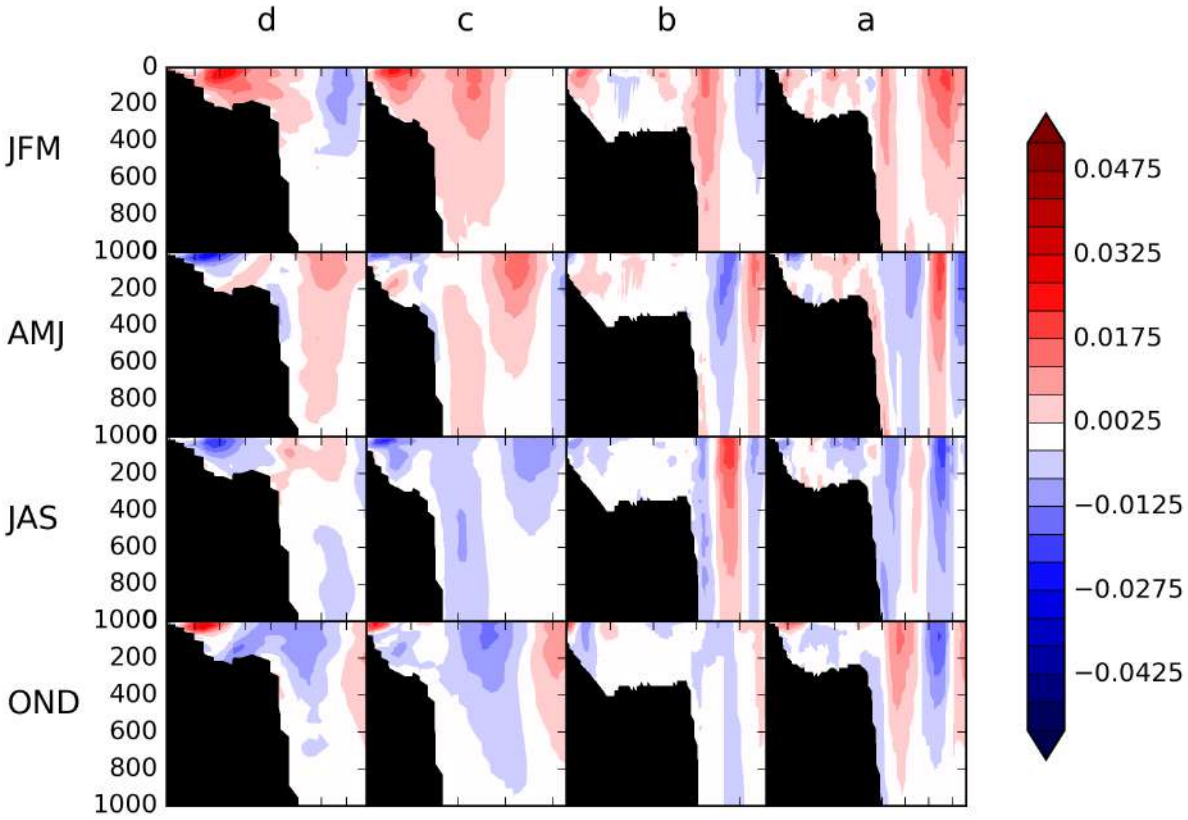

Figure 2.28: *S*easonal current anomalies calculated subtracting the climatology mean from the climatology season. From right to left we have section 'a','b','c' and 'd' and from upper row to lower row we have: winter (JFM), spring (AMJ), summer (JAS) and fall (OND) anomalies. Data are in m/s.

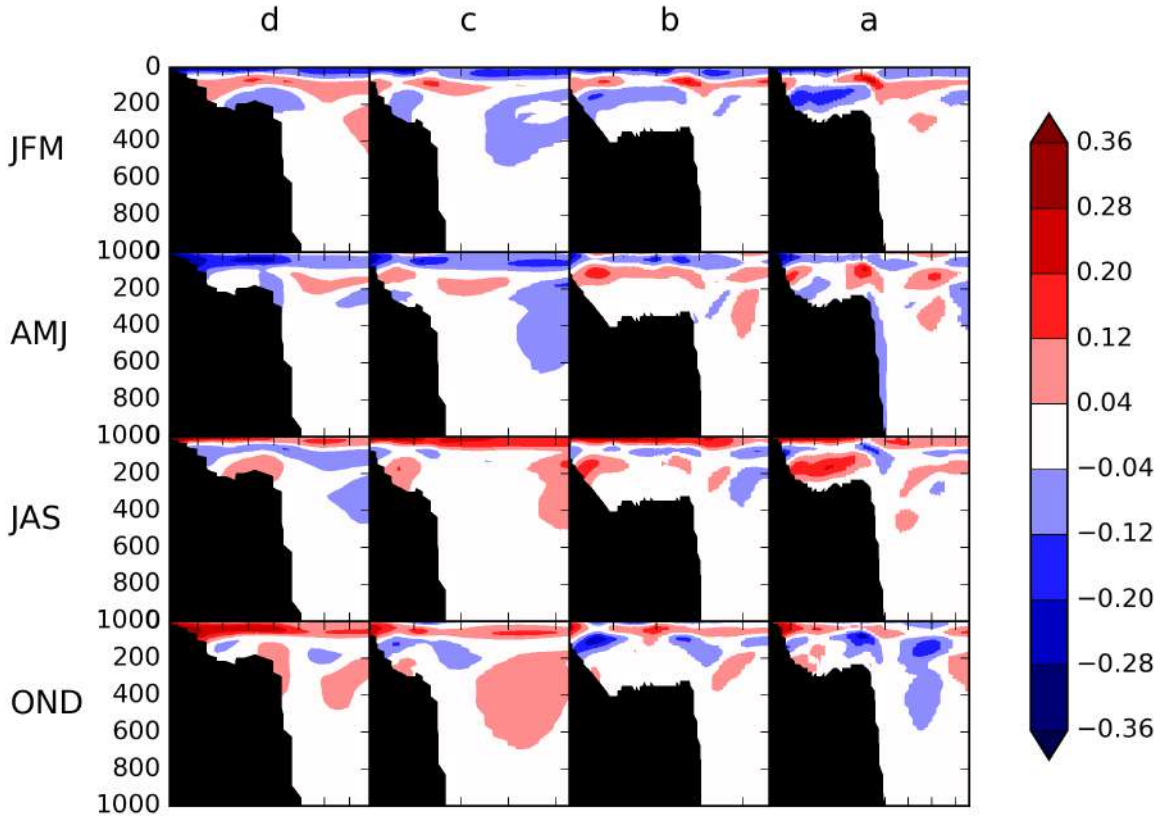

Figure 2.29: *S*easonal temperature anomalies calculated subtracting the climatology mean from the climatology season. From right to left we have section 'a','b','c' and 'd' and from upper row to lower row we have: winter (JFM), spring (AMJ), summer (JAS) and fall (OND) anomalies. Data are in °C.

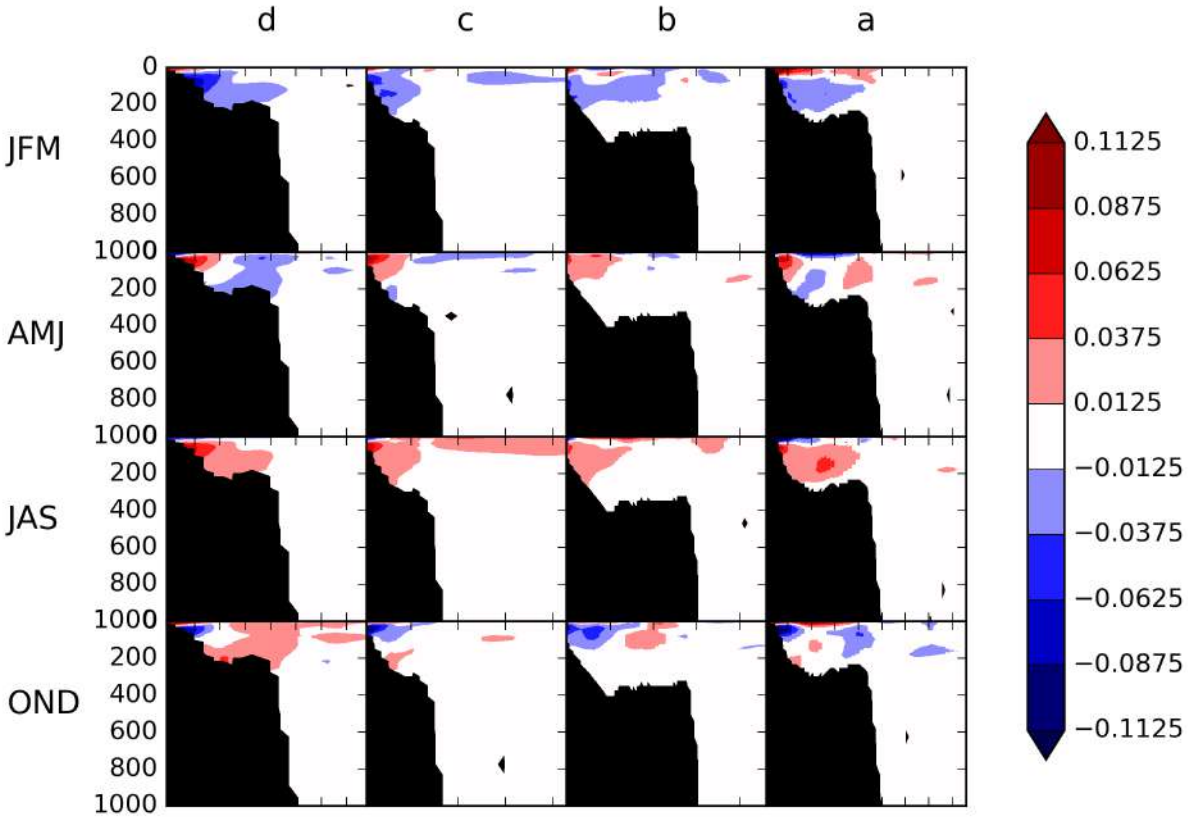

Figure 2.30: *S*easonal salinity anomalies calculated subtracting the climatology mean from the climatology season. From right to left we have section 'a','b','c' and 'd' and from upper row to lower row we have: winter (JFM), spring (AMJ), summer (JAS) and fall (OND) anomalies. Data are in psu.

Here we present the first seasonal analysis of the EGCC seasonality of volume and freshwater transport along the SE Greenland shelf. Using the same definition criteria for defining the currents boundaries as in the previous sections, we computed the volume and freshwater transport as before (Eq. 2.1 and 2.2), with reference salinity chosen to be 34.9 psu. In the next plots we show the climatological seasonality of the volume and freshwater transports associated with the EGCC. Figure 2.31 shows the volume transport in the four seasons; here we observe that maximum transport occurs in winter, while the minimum transport in summer.

EGCC (Sv)	60°N (CF)	61°N	63°N	65°N (DS)
total mean	2.05 ± 0.7	2.36 ± 0.43	1.36 ± 0.43	0.17 ± 0.21
winter mean	2.8 ± 1.13	3.1 ± 0.5	2.11 ± 0.43	0.07 ± 0.2
summer mean	0.76 ± 0.23	1.41± 0.18	0.68 ± 0.35	0.11± 0.09
OBS summer mean	1.16	1.54	0.93	0.8

Table 2.4: Total, summer and winter modeled mean volume transport from the 2008-2017 period over the 4 sections. In the last row is presented the mean from observations.

This suggest that all the shipboard measurements in literature underestimate by a factor of 2-3 the EGCC transport since they are mostly taken in summertime. 53Between sections we see great differences in the mean volume transport: it increases from 0.17 ± 0.21 Sv at Denmark strait to about 2 Sv at Cape Farewell. This is probably due to the recirculating waters from off-shelf that feed the EGCC. This is not so evident in the observations, but the observational dataset is scarce in time and, having very few observations, it is not possible to make a direct quantitative comparison. The volume and freshwater transport comparison between the model and the mean of the available observational dataset (data have been previously shown one by one in Table 2.1 and 2.2) is presented in Table 2.4 and 2.5. It appears that we underestimate (in average by 35%) the summer transport, obtaining though a great result in modeling the right magnitude of transport. In Plot 2.26 we can see in detail the behavior of the volume throughout the shelf and the climatological year. Similar conclusions can be drawn by looking at the freshwater transport in Figure 2.32 and in Table 2.5.
Consequently, we also underestimate the freshwater transport in summer. In Figure 2.7 we can see in detail the behavior of the freshwater transport throughout the shelf and the climatological year.

EGCC (mSv)	60°N (CF)	61°N	63°N	65°N (DS)
total mean	67 ± 19	86 ±16	53 ±18	10 ± 12
winter mean	87 ± 27	111 ± 19	82 ± 21	3 ± 1
summer mean	40 ± 13	61 ±10	32 ±16	8 ± 6
OBS summer mean	62	77	56	26

Table 2.5: Total, summer and winter modeled mean freshwater transport from the 2008-2017 period over the 4 sections. In the last row is presented the mean from observations.

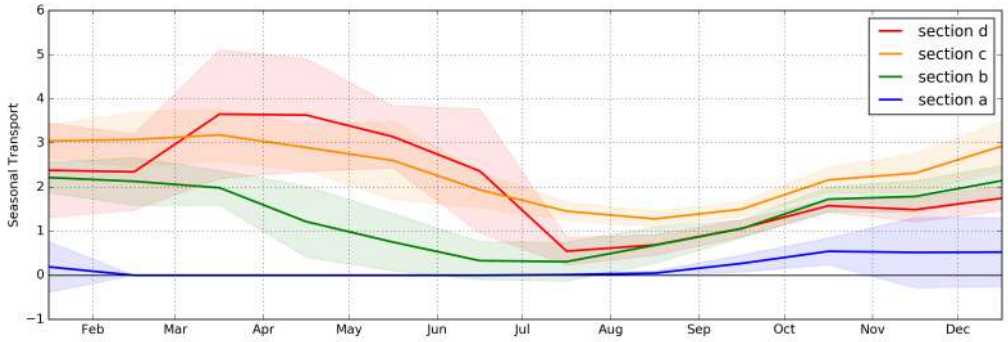

Figure 2.31: *C*oastal current volume transport for the four sections along the SE Greenland shelf. Bold line is climatological mean for each section and the colored shadow is the standard deviation. Data are in Sverdrup.

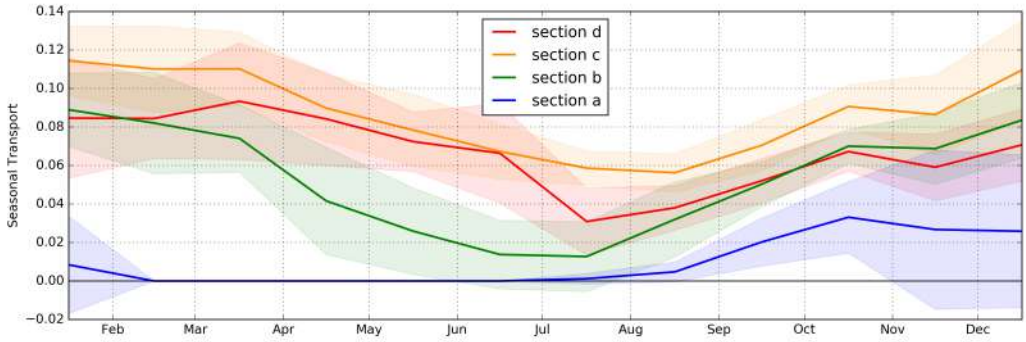

Figure 2.32: *C*oastal current freshwater transport for the four sections along the SE Greenland shelf. Bold line is climatological mean for each section and the colored shadow is the standard deviation for the mean. Reference salinity is 34.9 psu. Data are in Sv.

It is interesting to note though that both in observations and in the model, section 'c' has a stronger freshwater transport than section 'd', while the volume transport is more or less of the same magnitude. This can be explained by looking the structure of the currents in section 'c' and 'd'. In section 'c' the EGCC and EGC are almost merged together, while in section 'd' they detach in two clearly distinguishable cores. The difference in magnitude can be explained by the interplay of the currents between the two transects, where the EGC salts the EGCC along the path. Here we compare the seasonal cycle of volume and freshwater at Cape Farewell, with the first ever seasonal observational dataset, from OSNAP campaign [28].

The reference paper for this comparison is Le Bras et al. 2018 [9]. Since the OSNAP available dataset ranges from August 2014 to August 2016, the same time-series is considered from the numerical simulation in order to make a direct comparison. Mean volume and freshwater transports and their seasonal ranges for the EGCC at Cape Farewell are quoted in Table 2.4 and 2.5. Model results and observations show some discrepancies: first of all, the mean transports appear to be larger with higher variability between minima and maxima.

Sv	Min	Max	Mean
OBS 2014-2016	0.66 (June)	1.1 (December)	0.9 ± 0.1
MODEL 2014-2016	0 (July)	5.02 (March)	1.97
MODEL 2008-2017	0.54 ± 0.31 (July)	3.65 ± 1.46 (March)	2.05 ± 0.68

Table 2.6: *O*bserved and modeled (2014-2016 and 2008-2017) minimum, maximum and mean Cape Farewell EGCC volume seasonality.

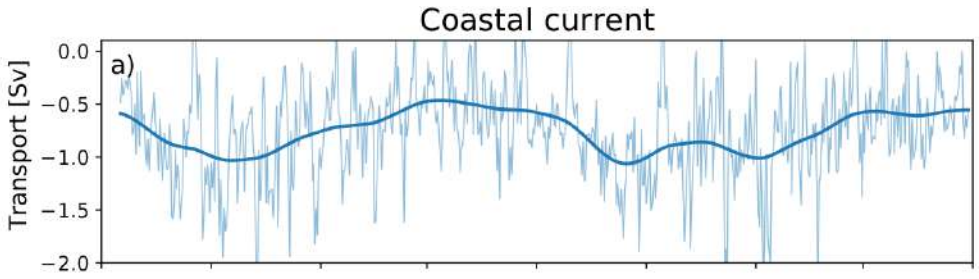

Figure 2.33: *E*GCC volume transport and measured by the OSNAP Cape Farewell moorings from August 2014 - August 2016.

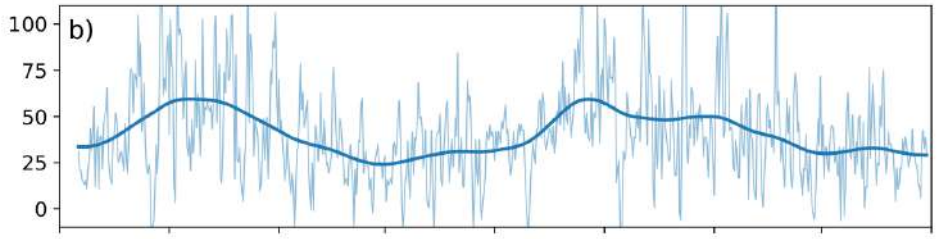

Figure 2.34: *E*GCC freshwater transport and measured by the OSNAP Cape Farewell moorings from August 2014 - August 2016.

We observe a staggered seasonality comparing model and observed EGCC transport, and, while in observations the maximum occurs in November and the minimum in May (Fig. 2.33 and 2.34), in our model they occurred respectively in

Sv	Min	Max	Mean
OBS 2014-2016	32 (June)	60 (December)	46 ± 6
MODEL 2014-2016	0 (July)	104 (March)	55 ± 22
MODEL 2008-2017	30 ± 17 (July)	93 ± 30 (March)	67 ± 19

Table 2.7: *O*bserved and modeled (2014-2016 and 2008-2017) minimum, maximum and mean Cape Farewell EGCC freshwater seasonality.

March and September (Fig. 2.31 and 2.32). In trying to understand what is causing the variability and the model delay in reproducing it, we follow the approach used in [9] and we try to compare it to the sea ice concentration in that section. Sea ice concentration at Cape Farewell peaks and exhibit the same variability in both in observation and in the model, so the difference we observe is only in the coastal current transport, both in magnitude and seasonality. Additionally, comparing Figure 2.36 and Figure 2.37 we exclude that the behavior of model 2015 it is exceptional, since the climatology 2008-2017 exhibit the same peaks in the same months. Le Bras et al. 2018 argue that the correlation they observe between sea ice and transport means that there is a cause-effect relationship, either (I) EGCC transport changes lead sea ice or (II) sea ice leads EGCC transport changes. However from the model we do not observe a correlation in the seasonal cycle of sea ice and EGCC transport.

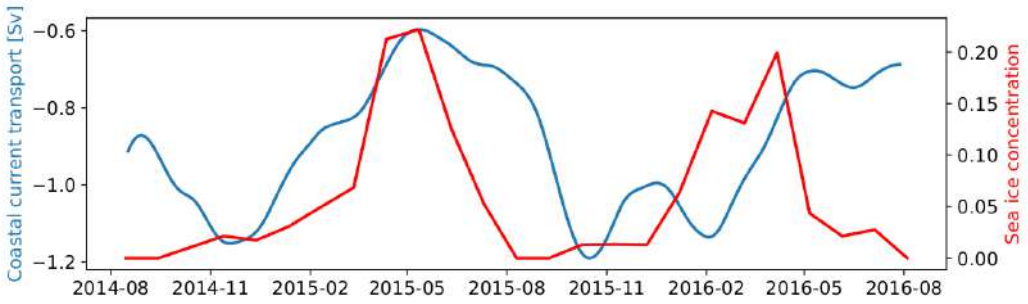

Figure 2.35: *F*rom [9]. OSNAP sea ice concentration on the shelf over the moored array (red, right axis) and EGCC volume transport (blue, left axis).

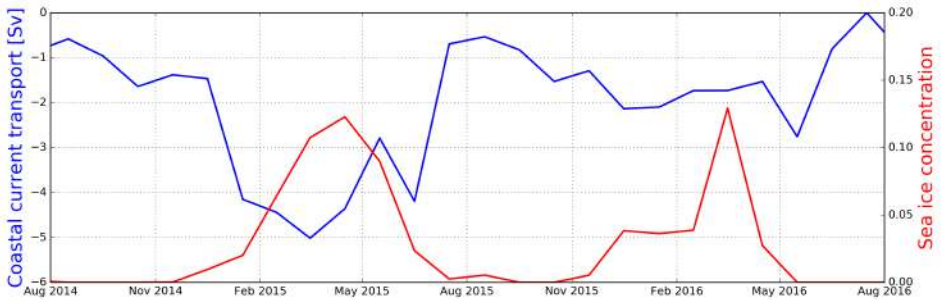

Figure 2.36: *G*LOB16 sea ice concentration and EGCC volume transport over section 'd' at Cape Farewell for the period 2014-2016.

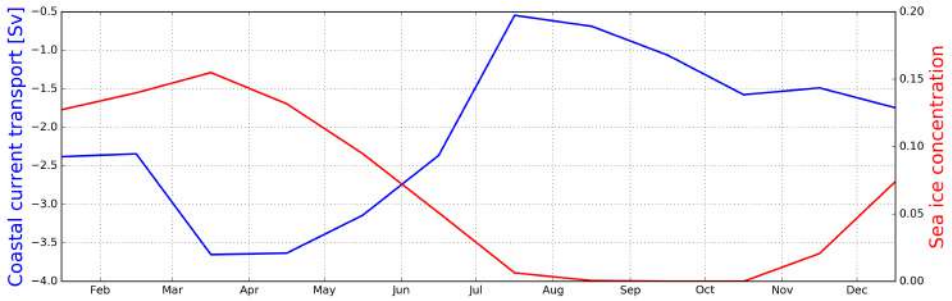

Figure 2.37: *G*LOB16 sea ice concentration and EGCC volume transport over section 'd' at Cape Farewell climatology 2008-2017.

Beforehand a seasonal analysis from observational dataset for the EGCC temperature, salinity and velocity was not available, so this is the first ever comparison

between a global ocean model and a seasonal data in this region. We will be using both modeled 2014-2016 data and the modeled decade 2008-2017. The whole decade is used as control, to infer if the 2014-2016 period is similar to the climatology. With the same dataset we compared in the previous paragraphs the freshwater and volume transport and here we show the comparison regarding the seasonal temperature, salinity and velocity fields. As in the Cape Farewell transport and mean fields analysis, here the reference paper for this comparison is Le Bras et al. 2018 [9]. In Figure 2.38, the seasonal anomalies for first full year of data are shown. The same anomalies from the model output for the same period of time are displayed in Figure 2.39. Comparing the seasonality, we observe that the anomalies have the correct amplitude: current anomalies go from -0.1 to 0.1 m/s, salinity anomalies from -0.2 to 0.2 psu and temperature anomalies range from -2 to 2 °C. Winter (JFM) is well represented by the model: the EGCC is saltier, slower and cold. The slope current in winter exhibit higher velocity, it is fresher than usual and cold (Figure 2.38 and 2.39). In fall (OND), the coastal current is the fastest and the shelf water is the freshest (Fig. 2.38) and the whole region of interest experiences a warming. In the modeled data, things are different: in fall the water characteristics are very similar to the winter one, while water with observed fall characteristics is reproduced in summer (Figure 2.39). In spring and summer, observations have similar properties so they have been merged in Figure 2.38, which shows that the water over the slope becomes warmer and saltier, while the two seasons have actually opposite behavior in the model. All the seasons have been analyzed also for the entire decade 2008-2017, showing that the seasonal pattern seen in 2014-2015 is not peculiar, but resembles the signature seen in the climatological seasonality (Fig. 2.39 and Fig. 2.40). What can be extracted from this is that the EGCC modeled summer and observed fall share the same features, an EGCC that is faster, fresher and warmer with respect to the climatological mean.

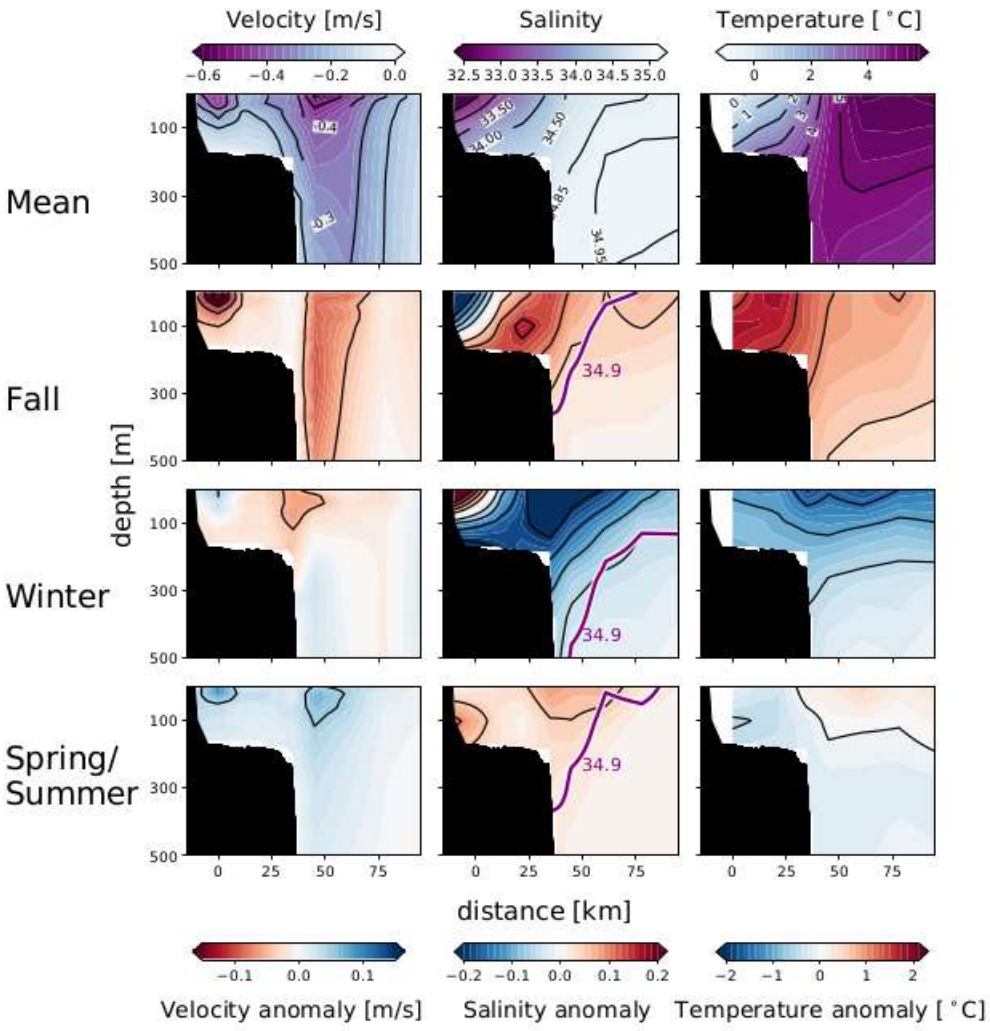

Figure 2.38: *P*lots from [9]. Velocity (left), salinity (center) and potential temperature (right) annual mean (top row) and anomalies (lower panels) based on the OSNAP Cape Farewell mooring data from the first full year.

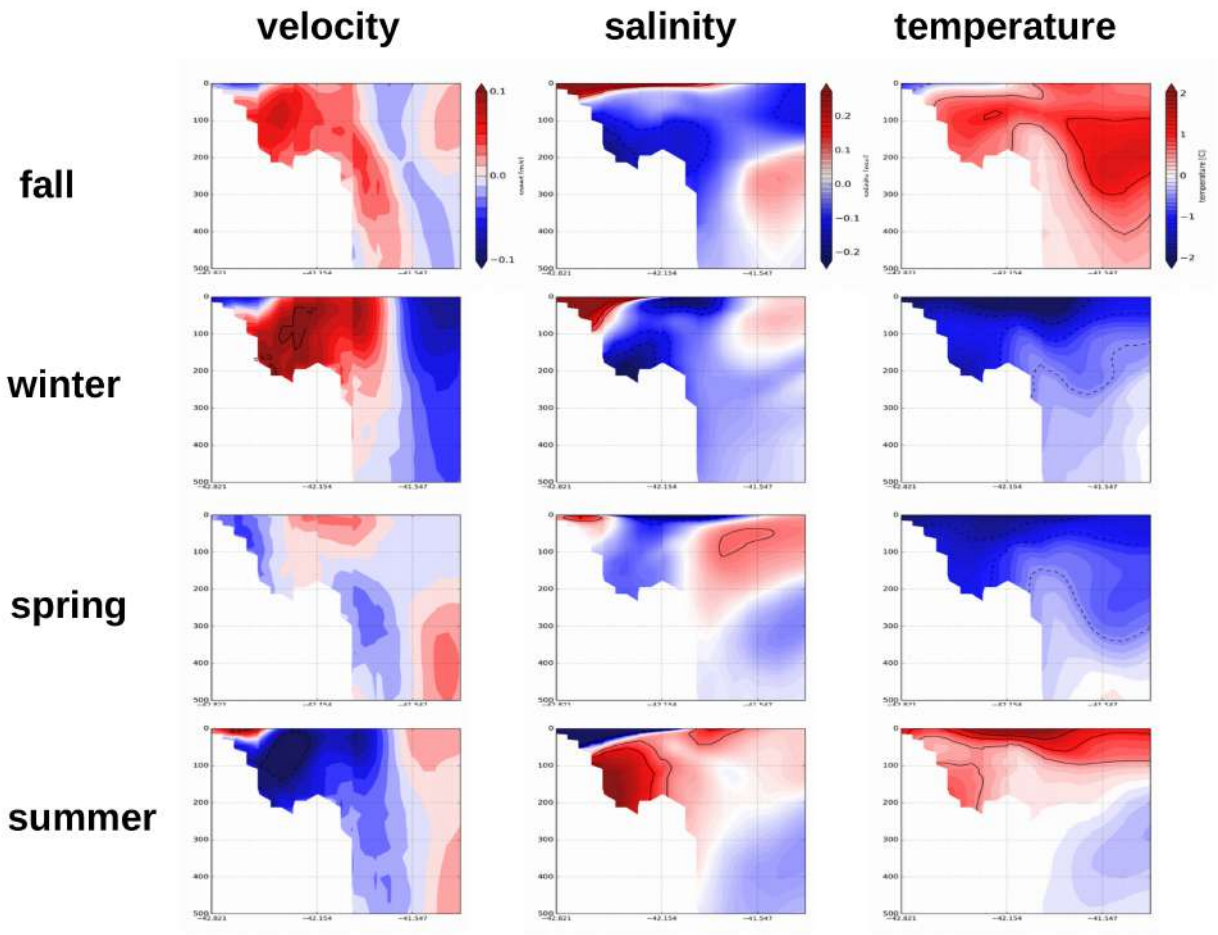

Figure 2.39: *V*elocity, temperature and salinity for fall (upper row) winter (second row),spring (third row) and summer (last row) anomalies from GLOB16 output between October 2014 - September 2017

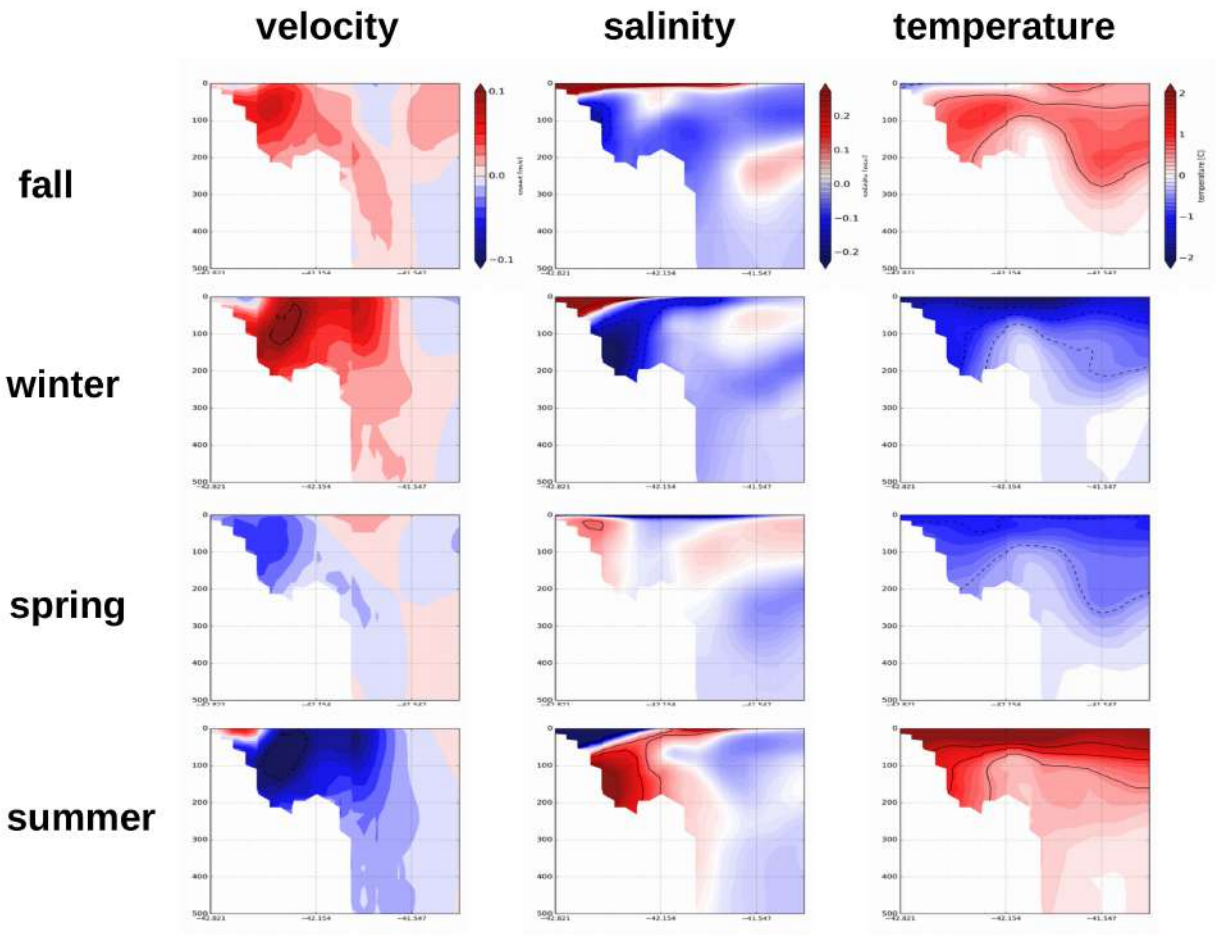

Figure 2.40: *V*elocity, temperature and salinity for fall (upper row) winter (second row), spring (third row) and summer (last row) anomalies from GLOB16 output between January 2008 - December 2017

2.4 Discussion and conclusions

In this chapter, we investigated the mean and the seasonal variability of the SE Greenland coastal currents, with a focus on the East Greenland Coastal Current (EGCC), making use of the output of the GLOB16 configuration in the decade 2008- 2017 and available observational datasets. The model configuration used in this study is based on the NEMO framework and has an horizontal resolution of 1/16°, allowing us to resolve the currents as they flow along the shelf. Firstly we assessed the ability of the model in reproducing the mean state on the currents that flow along the shelf. Three different currents on the SE Greenland shelf were recognized as the surface- intensified East Greenland Coastal Current (EGCC), the East Greenland Current (EGC) that merges downstream of Sermilik fjord to form the East Greenland Current/Irminger Current (EGC/IC). Model mean temperature and salinity showed warm and salty waters outside the shelf and cold, fresh water on the east Greenland shelf. As expected the EGC/IC current show an Atlantic-influenced water mass, with mean T $>$ 5°C and S $>$ 34.6 psu while the coldest water mass has temperature lower than 0 °C with a salinity that ranges from 31.5 to 33.5.

We found salty and warm water also in the subsurface waters, far inshore of the shelf-break supporting the knowledge of flow being diverted toward the inner shelf, bringing with it AW influence from the EGC/IC system.

Spatially the EGCC is confined to a shallow depth on the inner part of the shelf, while EGC/IC is found on the shelf-break with maximum velocities extending till 500 m deep. It has been observed in the sections located at 63-65 °N a equatorward flow centered at 500 m on the shelf-break, attributed to the Spill Jet described by e.g. by Pickart et al. (2005) [4].

Additionally, we show that the model is able to reproduce the right magnitude of both volume and freshwater mean transport for the 2008-2017 period. Accordingly with observations, the transports increase flowing southward from section 'a' until section 'd'. This difference in transport come from various branches of EGC/IC feeding the EGCC recirculating on the shelf.

The high resolution model used in this study provides an accurate simulation of the shelf in the mean state, being able to model not only the right properties that each current carries, but also the structure of the EGC/IC that branches and

recirculate on the shelf. These branches change the volume and properties of the EGCC, feeding it as it flows along the shelf. We analyzed the seasonal variability of EGCC temperature, salinity and velocity on the shelf.
Regarding salinity, in summer (winter), a band of high(low)-salinity water is found all over the shelf, progressively increasing going in the inner part. Spring and fall show a two-core pattern with opposite salinity anomalies: one north of Kangerdlugssuaq Through and the other one on the shelf outside the Sermilik fjord.
Summer and fall temperatures on-shelf and off-shelf are uniformly higher than average with a slight increase in temperature toward the south and in the Sermilik Through while in spring and winter on-shelf and off-shelf temperatures are uniformly colder than average. Mean and seasonal SST for the same period have been validated through the comparison with AVHRR satellite data.
Since the mean seasonal anomalies associated with the EGCC are not bigger than 4 cm/s resulting in more or less the 5-10% of the actual currents,they lead to small differences in the current velocities through the year. The same thing happens with salinities (smaller than 0.1 psu) and temperatures (smaller than 0.3°C).
Summer water properties (temperature and salinity) were validated along the shelf using the milestone paper from Sutherland and Pickart 2008 [10], while summer transport (volume and freshwater) has been validated through a complete review of the literature. In particular at Cape Farewell (near 60°N) we have been able to compare year-round volume and freshwater transport, and salinity and temperature fields.
These comparisons show that the model is able to reproduce the general mean and seasonal state of the currents, salinity and temperature. In particular the model is able to represent summer condition (transport and fields) all over the shelf, and year-round conditions at Cape Farewell. Indeed, the comparison between OSNAP data and model data show, firstly, that even though 2015-2016 have been exceptional years (characterized by enhanced deep convection in the Irminger Sea , [35]), model seasonal features in the period 2014-2016 are very similar to those averaged over the whole decade.
Both modeled volume and freshwater transports peak in March and have the minimum in July, suggesting that winter transport is stronger than in summer, and that the summer-time campaigns always underestimate the annual mean freshwater transport. The same seasonality in transport is observed in a model by Bacon

et al.,2014, that simulated an EGCC persistent throughout the year with maximum winter transport occurring in February.

The combination of moored measurements and their model output was enough to address the seasonal evolution of the EGCC at only one particular location. A new result of this study is the evidence of the seasonality all over the shelf. Another important result of this study is the partial disagreement between our analysis and the observed transport seasonality at Cape Farewell. The observed transport maximum occurs in June and exhibit its minimum in November, while with our model we observed a staggered seasonality, peaking in March and having its minimum in July. On the other hand, studying the EGCC salinity and temperature we observe that properties are well represented, even though modeled summer water have the same properties as observed in fall.

An immediate extension of the current analysis would consist in addressing the discrepancies found in the transport variability, in order to understand the processes behind the shifted variability at Cape Farewell.

In summary, with the available observations (2008-2017) and Cape Farewell seasonality (2014-2016), we validated the (I) shelf modeled mean and summer estimates, (II) the Cape Farewell seasonal evolution and (III) the mean and seasonal SST on the shelf and the Irminger Sea.

This work represents a step forward in the understanding of the SE Greenland complex current system as it progresses along the South-East Greenland shelf year-round.

The global model GLOB16 can be further employed to answer large-scale scientific questions that still remain open. As an example, an extension of this work could make use of this global model to address the origin and fate of the EGCC, that still remains uncertain.

Chapter 3

Mechanisms and processes responsible for the observed temperature variability on the SE Greenland shelf

3.1 Introduction

Two water masses reside on the SE Greenland shelf: Polar Water (PW), originated for the most part in the Arctic Ocean, and Atlantic Water (AW), advected from the Irminger Sea [12].
In this analysis we consider as PW all the water masses colder than 2°C and fresher than 32 psu and as AW those waters with T $>$ 5°C and S $>$ 34.6 psu [10].
The interaction between these two water masses on the shelf is a critical factor in setting the water masses found within SE Greenland's glacial fjords [12].
The relative partitioning of these water masses changes both seasonally (Chapter 2) and inter-annually [3], as shown by changes in the Sea Surface Temperature on the shelf, and the mechanisms driving such changes are still unclear [36].
Changes in the atmospheric variability [36], in the East Greenland Coastal Current transport and the offshore sub-polar gyre circulation [37] are likely to concur to the seasonal and inter-annual changes of the water masses flowing on the shelf.
While in Chapter 2 we showed how GLOB16 configuration is able to represent the mean and seasonal variability of water masses and hydrography on the SE

Greenland shelf, here an analysis of the inter-annual variability is presented in the decade 2008-2017 tog study of the mechanisms responsible of the observed variability.
Specifically in Section 3.2 we present observational datasets in addition to the ones introduced in Chapter 2. In section 3.3 a validation of the inter-annual variability is presented y both on the shelf and in the Irminger Sea Interior. We will focus next on mechanisms and processes responsible for the observed temperature variability on the shelf.

3.2 Observational datasets

Two more datasets are used in this Chapter for sea-ice and Irminger Sea Interior temperature variability. The EN4 dataset [38] is used to analyze the Irminger Sea Interior (ISI) seasonal and inter-annual temperature variability, while the Scanning Multichannel Microwave Radiometer (SMMR) dataset to validate the concentration of sea ice on the shelf. The EN4 dataset of the Met Office Hadley Center is a collection of ocean temperature and salinity profiles obtained across the global oceans over the period 1900 to present, to which a series of quality control checks have been applied.
It consists of two products:

- Subsurface ocean temperature and salinity profile data obtained from the WOD09, GTSPP, Argo, and ASBO collections with data quality information;

- Monthly potential temperature and salinity objective analyses calculated from the quality controlled profile data with uncertainty estimates.

Here the gridded monthly Objective Analyses (OA) from 2008 to 2017 have been used in the region shown in Fig. 3.1. Even though the OA may be affected by interpolation processes, the dataset is subjected to quality control procedures and inter-comparisons to identify and remove duplicates.

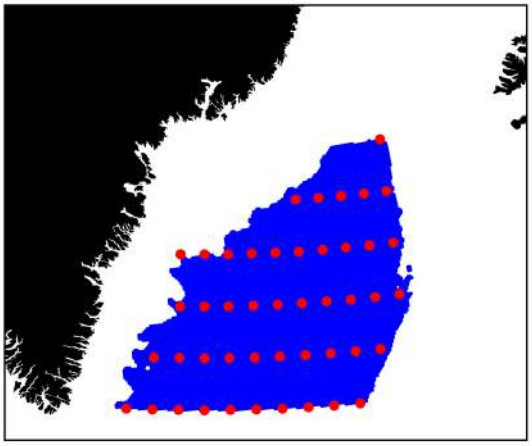

Figure 3.1: *A schematic showing region analyzed as the Irminger Sea Interior (ISI), defined as the region north of 60 °N where the bathymetry depth exceeds 1000 mt. The color blue represent the model region used, and the red scatter represents the EN4 dataset, with a horizontal resolution of 1° x 1°. Continents are depicted in black.*

Sea ice Concentration (SIC) is defined as the fraction of sea covered by ice for each model grid point, varying between 0 and 1, where 1 means complete coverage. In this Chapter we use the following datasets:

- SIC from Nimbus-7 SMMR and DMSP SSM/I-SSMIS Passive Microwave Data, Version 1 (NASA, [39]);
- SIC from Nimbus-7 SMMR and DMSP SSM/I-SSMIS, Version 3 (Bootstrap, [40]).

The datasets are both gridded on the SSM/I polar stereographic grid (25 x 25 km) and have 1 month temporal resolution. They are derived using measurements from the Scanning Multichannel Microwave Radiometer (SMMR) on the Nimbus-7 satellite and from the Special Sensor Microwave/Imager (SSM/I) sensors on the Defense Meteorological Satellite Program's (DMSP) -F8, -F11, and -F13 satellites. Measurements from the Special Sensor Microwave Imager/Sounder (SSMIS)

aboard DMSP-F17 are also included. These datasets are based on the brightness temperature information collected from the same satellite sensors, with the only difference in the processing algorithm, where the NASA Team employs the ratios of brightness temperatures and the Bootstrap Team makes use of an interpolation between clusters of pure ice types.
The Bootstrap sea ice concentration dataset is believed to be more useful for modeling and process studies in the polar regions because it is generally free of residual errors that could not be removed by conventional techniques [40].
In this Chapter we will use both in order to capture possible discrepancies in using one or another.

3.3 Results

The inter-annual variability validation on-shelf and outside the shelf is here firstly presented, then the inter-annual mechanisms and processes responsible for the observed changes in temperature on the SE Greenland shelf during the decade 2008-2017 are assessed.

3.3.1 Inter-annual variability validation

Observations on the SE Greenland shelf are scarce in space and time due to difficulties in reaching the shelf, that is accessible only in summer when the absence of sea ice allows ships to access the coast. So a comprehensive description of the inter-annual temperature variability on the whole SE Greenland continental shelf has never been performed using observations.
The only local exception is the OSNAP program (detailed in Section 2.3, [28]), an observing system that consists, among other measurements system, of moorings deployed at Cape Farewell, southern Greenland, that allow a continuous local collection of data since 2014.
We here validate the model shelf temperatures in the decade 2008-2017 with the available observations. The goal is to understand if GLOB16 is able to reproduce the observed temperature variability year by year on the SE Greenland shelf and into the Irminger Sea interior, in order to address the causes that can drive the observed changes in shelf temperature within this period. To validate the model

temperature in the Irminger Sea Interior (ISI), we firstly use the EN4 dataset in the selected area (as in Fig. 3.1).

The Hovmoller diagram from January 2008 to December 2017 temperature as computed by GLOB16 is shown in Figure 3.2, averaged on the area in Fig. 3.1. For the same region and time-range in Figure 3.3 the temperature from the EN4 dataset is presented. The model represents temperature changes reliably: both the mean seasonal and inter-annual variability cycle timing are well reproduced. Interannually GLOB16 is in agreement with the EN4 dataset: a progressive cooling started in late 2014 and resulting in three years of deep convection is evident from both Fig. 3.2 and 3.3.

However, some discrepancy are present regards the magnitude: for example we observe a temperature summer surface maximum of ∼9°C while GLOB16 models a maximum of ∼7°C, showing that the gradient between the surface and the temperature at depth is steeper in the observations. Another difference is evident if we look at the variability around 200 m of the water column: in the model all the seasonal changes appear to occur above this depth, while in the observations the seasonal cycle extends from the surface to as deep as 400 meters. This is due to an higher stratified deep column water, caused by the mixing parametrization in the ocean component of the model, that in turn causes a reduced mean convection in the ISI. This feature is known to cause some discrepancies with observations, e.g. in Labrador Sea [22], where the model accentuates the deep convection.

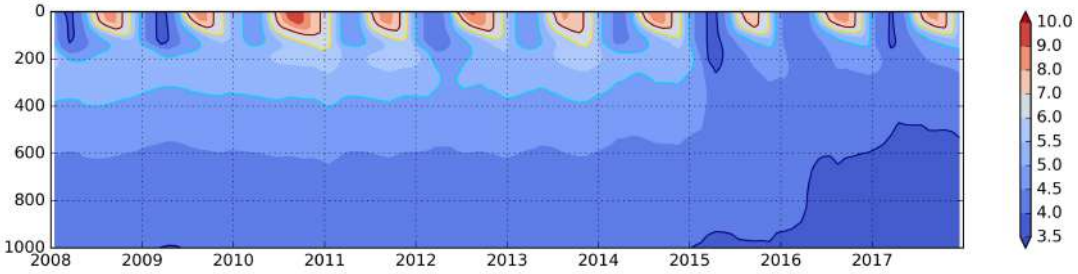

Figure 3.2: *EN4 dataset temperature Hovmoller diagram for the January 2008-December 2017 period, averaged on the region depicted in 3.1. White line represents 5° C contour, black line 4° C and red line 6° C.*

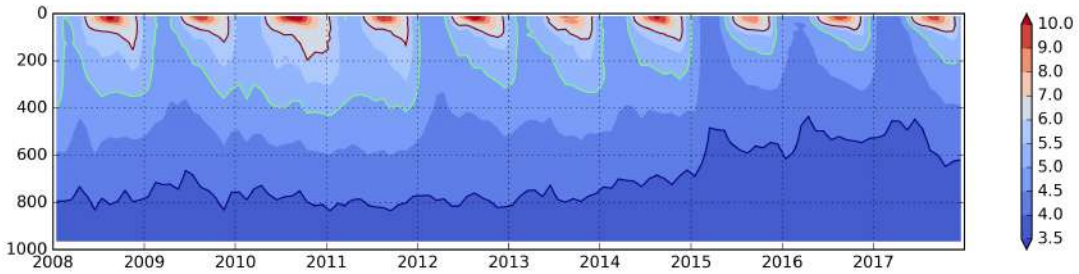

Figure 3.3: *GLOB16 temperature Hovmoller diagram for the January 2008-December 2017 period, averaged on the region depicted in Fig. 3.1. White line represents 5° C contour, black line 4° C and red line 6° C.*

To further confirm the interannual variability, we employed the LOCO mooring time-series([41], black dots in Fig. 3.4), that collected data from 2004 to 2016 in the middle of ISI, at around 59.5 °N and -39 W and here we compare the years where model and observations overlap.
In Fig. 3.4 and 3.5 we show the averaged temperature over 0-1000 m from GLOB16 at the same location and from the LOCO mooring respectively.
In Fig. 3.5 the output of the de Jong et al. 2016 [41] 1D model based only on

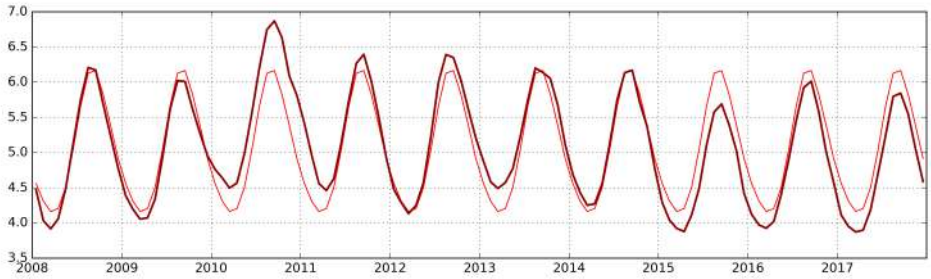

Figure 3.4: *0-1000 m averaged temperature at the LOCO location. Dark red line is the actual variability and red line is the repeated mean 2008-2017 seasonal cycle, in order to easily recognize when a year is warmer or colder than the 2008-2017 climatology.*

heat fluxes from atmosphere (red line) is also shown, and compares well to the variability from the LOCO mooring. GLOB16 is in agreement with both observations from the LOCO mooring and the 1D model the warmest year in the range 2008-2017 was 2010 and the coldest 2015.

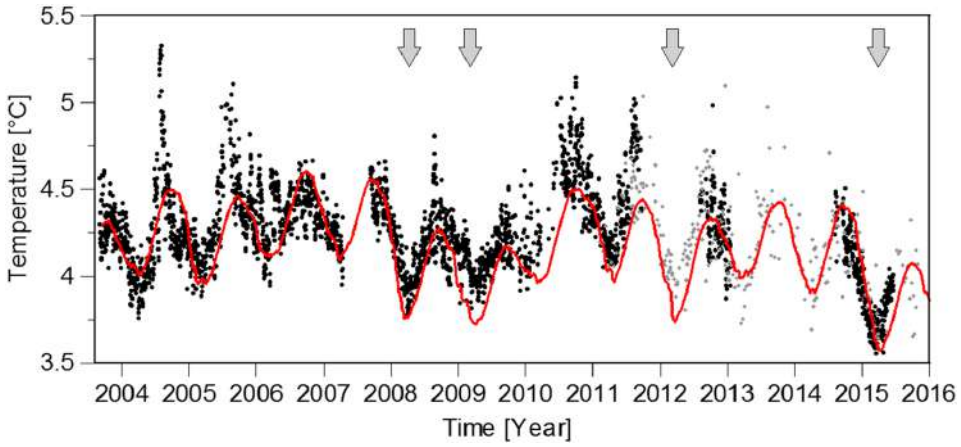

Figure 3.5: *Plot from [41]. 0-1000 m averaged temperature in the LOCO mooring. Red line is the variability computed from the 1d model for heat fluxes. Black dots are the actual data from the mooring and gray lines are ARGO data used to fill in the gaps of the mooring dataset.*

In 2014, 2015, 2016 a strong winter cooling over the Irminger Sea with a concurrently exceptional deep convective mixing, and the emergence of anomalously low SST ([42]). The deep convection events in 2014-2016 has been exceptionally larger than the 2003-2015 mean, when the local mixing removed the stratification of the upper 1400 m of the water column. This exceptional signature is clearly visible in winter in both model and observations, where the cooling is enhanced in the years of deep convection. In Fig 3.6, the temperature changes averaged over 0-1000mt along with the mean mixed layer in the ISI region are shown.

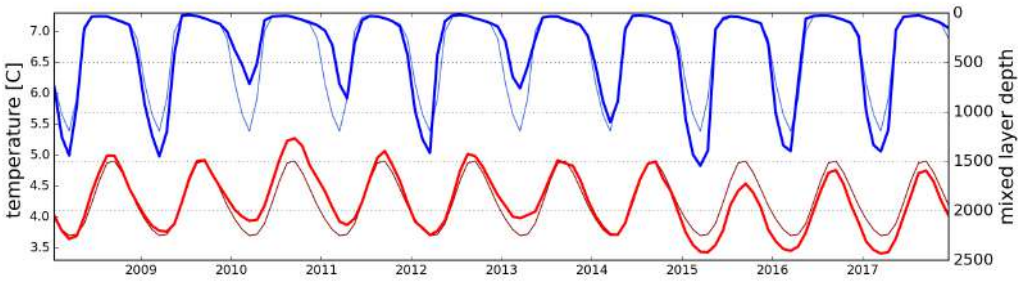

Figure 3.6: *Temperature variability (red bold line), climatology (dark-red) and mixed layer depth variability (blue bold line), climatology (dark-blue) for the time-series from 2008 to 2017 average on Irminger Sea Interior region.*

It is notable that the mixed layer experiences a deepening in the period 2014-2016, proving that the model is able to reproduce the features above presented that are associated with the deep convection years, as represented in the EN4 dataset. The additional coherence between the data and the 1D model from [41](red line in Fig. 3.5) supports the notion that this anomalous temperatures (e.g. the ones in 2010 and 2015) were driven by atmospheric forcing [42].
We conclude that the model is able to reproduce the main features of temperature seasonality, and also to represent the inter-annual variability and deep convection years in the Irminger Sea Interior. Therefore we use the GLOB16 configuration as a numerical tool to investigate the processes and mechanisms that can cause the aforementioned variability.
Sea ice concentrations from satellite are available for the whole shelf year-round; for this reason they have been employed to validate the shelf region on inter-annual time-scales. In Fig 3.7, the orange box shows the region over which sea ice from the observations is averaged. The GLOB16 and observed variability of SIC are shown in Fig. 3.8 and 3.9 respectively. The two seasonal cycles peak at the same time, where minima typically fall in September and maxima in March. 2016 appears to be an anomalous year for sea ice on the shelf in both the model and observations: 2016 minimum is prolonged in time in both, and while model shows a complete lack of sea ice for six months, the observations indicate little or no sea ice for the same amount of time.

2008-2012 SIC exhibits a summer maximum that does not have any visible trend. However, starting from 2012 it is present a progressive reduction of SIC summer presence, that persists till 2017.
The model reproduces the progressive reduction of the sea ice concentration maximum in the region that has been also observed from satellite. Observed maximma are smaller than modeled ones. While observed SIC is never higher than 0.5, the simulated maxima reach 0.8 during 2008-2012.
This can be ascribed to an increased sea ice transport through Denmark Strait in the model as shown in the next section (Fig. 3.26).
Nonetheless, the seasonality and inter-annual variability are well represented, allowing us to be able to use the sea ice to study the mechanisms causing the temperature variability. Having a wider SIC seasonal cycle does not affect significantly the following analysis, since we focus on the inter-annual changes and

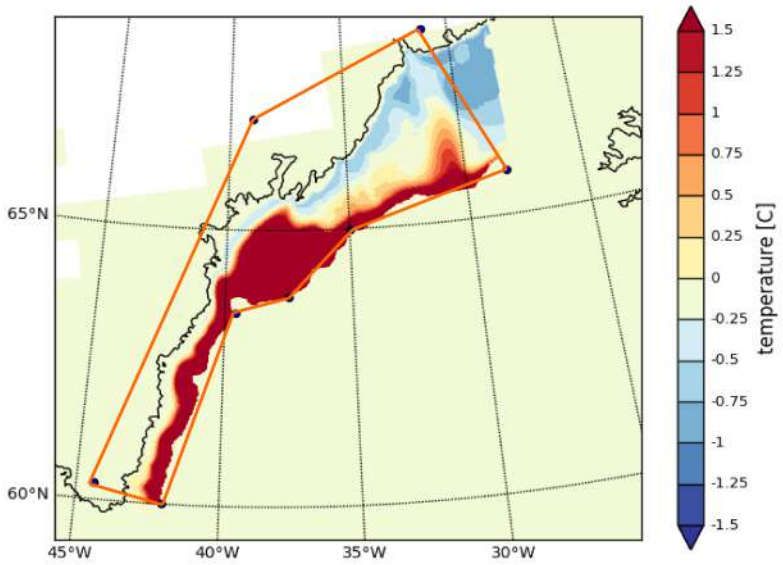

Figure 3.7: *Colors represent the temperature averaged between 0-1000 m on the shelf region during the 2008-2017 period. Orange lines define the box over which we computed sea ice concentration.*

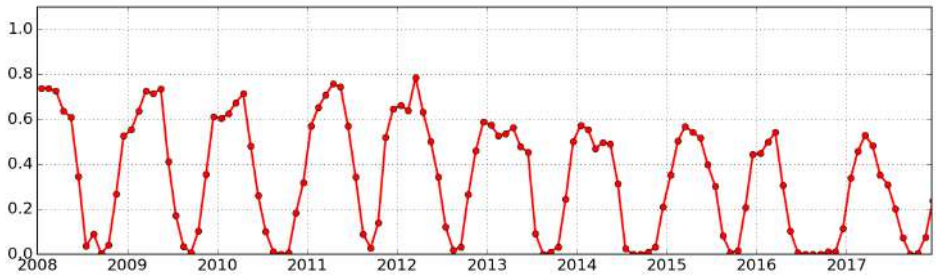

Figure 3.8: *GLOB16 sea ice concentration on the SE shelf.*

anomalous years, that are still well represented in the model.

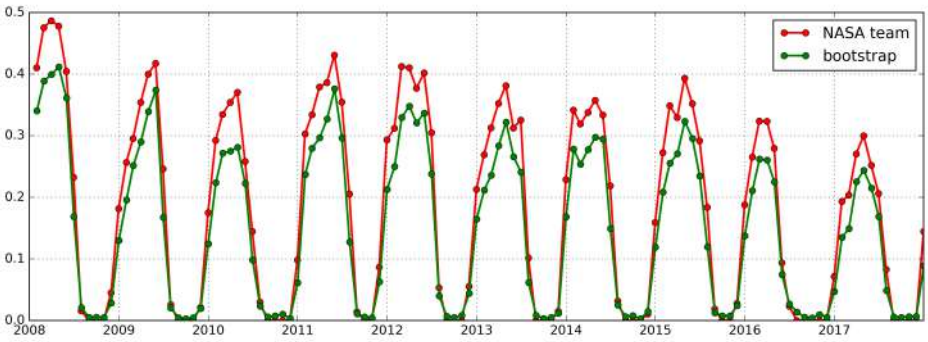

Figure 3.9: *Sea ice concentration from satellite observations (NASA and Bootstrap) on the SE Greenland shelf.*

3.3.2 Inter-annual variability mechanisms and processes

Having compared the GLOB16 configuration to observations in the decade 2008-2017 on the SE Greenland area, we now investigate the possible drivers and their role in leading the temperature inter-annual changes observed by the model and the data.

In order to quantitatively assess the relative contribution of the drivers in leading the temperature variability modeled on the shelf, a box (depicted in Fig. 3.10) is designed on the model, encasing the shelf from 60°N to 69°N. The whole decade 2008-2017 is analyzed, with a focus on the anomalous years highlighted above.

In constructing the box, its lateral boundaries have been carefully chosen in order to include the shelf and the slope current flowing along the shelf, and to be not too far away from the shelf break (that is around 400 mt deep) in order to capture the inflow coming from the Irminger Current into the shelf.

Hereafter, we will refer to the north section as DSS (Denmark Strait Section), to the south one as CFS (Cape Farewell Section) and the sum of the lateral transects (L1, L2, L3 and L4) are referred to as LS (Lateral Section).

To derive the equation of mass budget over the box, we need to consider the change of mass per unit time flowing through the volume. We defined a volume V, bounded by area A on every surface of which the normal direction is described by the unit vector n.

For a generic vector flux F, Gauss theorem converts surface integrals to volume integrals:

$$\iiint (\nabla \cdot F) dV = - \iint F \cdot n dA \tag{3.1}$$

Considering Gauss's theorem as applied to the mass flux, defined as $F_M = \rho u$, and considering that the conservation equation of mass that takes the form [43]:

$$\nabla \cdot (\rho u) = \frac{\delta \rho}{\delta t} \tag{3.2}$$

we obtain the conservation of mass equation in integral form (see [43] for an in-depth discussion):

$$\frac{\delta}{\delta t} \int_V \rho dV = \oint_S (\rho \boldsymbol{u}) \cdot n dA \tag{3.3}$$

The equation 3.3 above shows that the net mass inflow normal to boundary (RHS) is equal to the rate of change of mass (LHS). The RHS of equation 3.3 can be

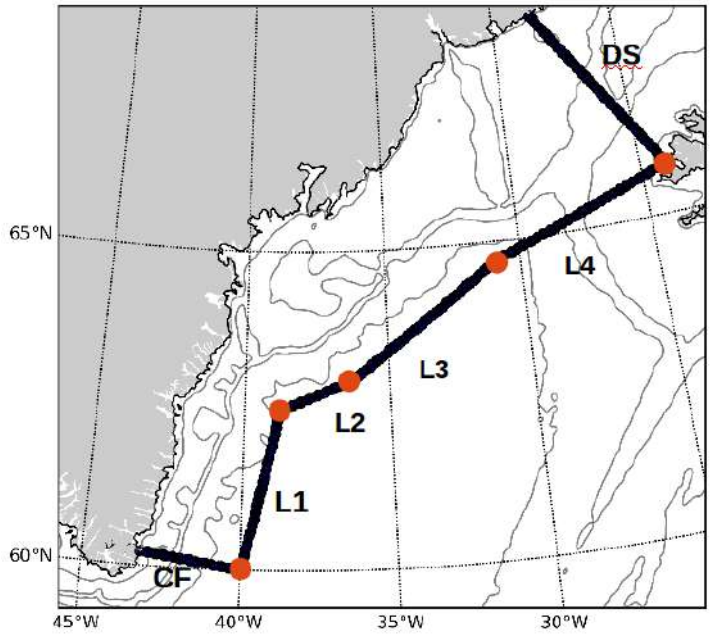

Figure 3.10: *Black dots represent the boundaries of the box encasing the shelf. Red dots represent the intersection between each transect. Thin black lines are bathymetry contour for 50, 400, 1000 and 2000 mt.*

additionally decomposed in F_m^{bdy}, the divergence of the mass flux from the side-boundaries, and $F_m^{surface}$, the net total mass flux entering the ocean from the surface, sum of evaporation, precipitation and run-off from land. In the stationary case, the time-varying terms equal zero ($\frac{\delta M}{\delta t} = 0$), so that the boundary flux is equal to the surface flux. Considering the terms above presented the resulting equation for mass can take the generic form:

$$F_M^{boundary} + F_M^{surface} = F_M^{storage} \tag{3.4}$$

On the other hand, the heat budget of the whole water column from surface to bottom is given by the following equation:

$$\frac{\delta(\oint_S \rho H^{i,o} \cdot ndA)}{\delta t} + \nabla \cdot (\oint_S \rho H^{i,o} \cdot ndA) = -\nabla \cdot F_H^{surface} + \rho\epsilon \tag{3.5}$$

where the superscripts i, o in Equation 3.5 stand for 'ice' and 'ocean'. The term $H^{i,o}$ is then the heat stored per unit mass (J/kg^{-1}) in the system, that comprises

the latent heat stored in ice, and the sensible heat stored in ice and ocean, and it expands to:

$$\oint_S \rho H^{i,o} \cdot ndA = (\rho C_p \theta)^o + (\rho C_p \theta)^i + (\rho L)^i$$

where θ is the potential temperature, ρ is the density of the body($\rho^o = 1035\frac{kg}{m^3}$; $\rho^i = 900\frac{kg}{m^3}$), c_p is the body specific heat capacity ($c_p^o = 4218\frac{J}{kg \cdot C}$; $c_p^i = 3000\frac{J}{kg \cdot C}$ and L is the latent heat of freezing of seawater.
The density approximations for water and ice are a sensible choice since, with the exception of only a small percentage of the ocean,density in the World Ocean varies by no more than 2% from this value (from Gill, 1982 [44], page 47). Specifically, Equation 3.5 is composed by:

- $\frac{\delta(\oint_S \rho H^{i,o} \cdot ndA)}{\delta t}$, is a heat flux ($W/m^3$) and represents the rate of change of the total stored heat within the defined boundary: $F_H^{storage}$. In stationary cases it is considered equal to zero.

- $\nabla \cdot (\oint_S \rho H^{i,o} \cdot ndA)$ is the divergence of the total ice and ocean sensible and latent heat flux crossing the boundary: $F_H^{boundary}$, (W/m^3).

- $-\nabla \cdot F_H^{surface}$, is the convergence of the surface flux formed by the sum of the radiative and turbulent heat fluxes at the surface, $F_H^{surface}$.

- $\rho\epsilon$ is the internal rate of dissipation of kinetic energy into heat, $F_H^{internal}$, here considered negligible, since in the arctic has been found to contribute to the total heat budget with a value of 0.025% [43].

In order to obtain the heat budget over the box, we integrate Equation 3.5 with respect to the volume V and after some assumptions (see [43] for an in-depth discussion) the equation that expresses the heat budget of the box can be expressed as:

$$F_H^{surface} = -\iint [(v' \rho c_p \theta')^{i,o} + (v' \rho L)^i] dsdz + F_H^{storage} \tag{3.6}$$

Where, ρ is the density of the body, c_p is the body specific heat capacity, v' is the anomaly term of the velocity v fromt the area-mean and L is the latent heat of freezing of seawater. The first term of the RHS of Eq. 3.6 is formed by the side-boundary sensible ice $(v' \rho c_p \theta')^i$, the sensible ocean $(v' \rho c_p \theta')^o$ and the latent ice $(v' pL)^i$ heat fluxes. We note that the sea ice sensible flux is very small compared

to the others, (about 1 %) and it is usually neglected. Between the remaining liquid sensible heat flux and sea ice latent heat transport, the dominant contribution in the Arctic Ocean is the sensible ocean heat [43]. The discussion will focus on this term.

Some uncertainties must be taken into account when computing mass and heat budget within the NEMO model. NEMO is a Boussinesq model, meaning that the governing equations conserve volume, rather than mass, and so do not properly represent expansion or contraction of the water-column. The steric effect is therefore not explicitely represented. More precisely, the mass which is conserved is the Boussinesq mass, $M_o = \rho_0 V$, where ρ_0 is 1035 kgm^{-3}. In others words, the Boussinesq mass, M_0, can be related to the total mass of the ocean seen by the Boussinesq model M, via the steric contribution to the sea level, η_s, a spatially uniform variable, as follows:

$$M_0 = M + \rho_0 \eta_s A \tag{3.7}$$

It has been already demonstrated that this approximation does not represent a serious error with respect to the flow field calculated by the model [45], but this is a well known source of uncertainties. Another source of systematic error is that we have assumed here that the total ocean surface, A, does not change when the sea level is changing. Lastly, in calculating the budgets through the side-boundaries, we considered the total area of the boundaries constant in time. In reality the computation of z_0, the first layer of the vertical coordinate z should be corrected by a term η, the local sea surface height, that changes in time, leading to a modified z_0 as:

$$z_0^* = z_0 + \eta \tag{3.8}$$

The approximation $z_0^* = z_0$, can be also a source of uncertainty.

We now consider the mean of the 2008-2017 climatological year for both mass and heat budget. In Figure 3.11 the net side-boundary ($F_M^{boundary}$) and surface ($F_M^{surface}$) components of the mass budget are shown.
The averaged in time and space boundaries contribution is 73 ± 61 mSv (red line, Fig. 3.11), while the surface contributes −40 ±13 mSv (blue line, Fig. 3.11). The

boundaries exhibit a enhanced standard deviation throughout the climatological year since the advection of waters presents a big inter-annual variability in the decade considered. The mean seasonal cycle of the contributors appears to be opposed: the boundaries have a positive maximum in April of 373 mSv and a negative minimum in August of -372 mSv, while the surface has a minimum in June of -60 mSv and a maximum in October of -11 mSv.
The mass storage term has been found to be negligible, ranging between -1 mSv and +1.5 mSv (not shown) with a mean of 0.05 mSv.
The total average does not sum up perfectly to zero, and this is explained by the above described assumption we made in calculating the budgets.

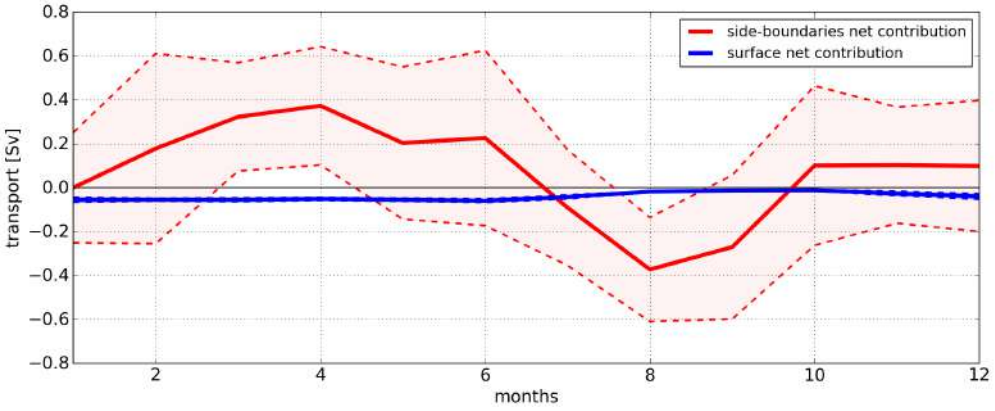

Figure 3.11: *Side-bundaries ($F_M^{boundary}$, red line) and surface ($F_M^{surface}$,blue line) net volume variability (in Sverdrup) for the period 2008-2017. Light-shaded areas and dashed lines show the standard deviation for every month.*

In Figure 3.12 we now show the net side-boundary($F_H^{boundary}$) and surface ($F_H^{surface}$) components of the heat budget. The mean values are 17 ± 27 TW for the side-boundaries net contibution and -15 ± 24 TW for the surface contribution. The seasonal cycle variability for the side-boundary term is almost identical to the mass budget one, consistently to the fact that the heat transport is mostly lead by volume changes. The maximum is found in April (lateral boundary term) and July (surface term) with a value of 38 TW and 22 TW respectively, and the minimum in August (side boundary term) and December (surface term) with a value of -7 TW and -44 TW, respectively (red and blue line in Fig. 3.12).

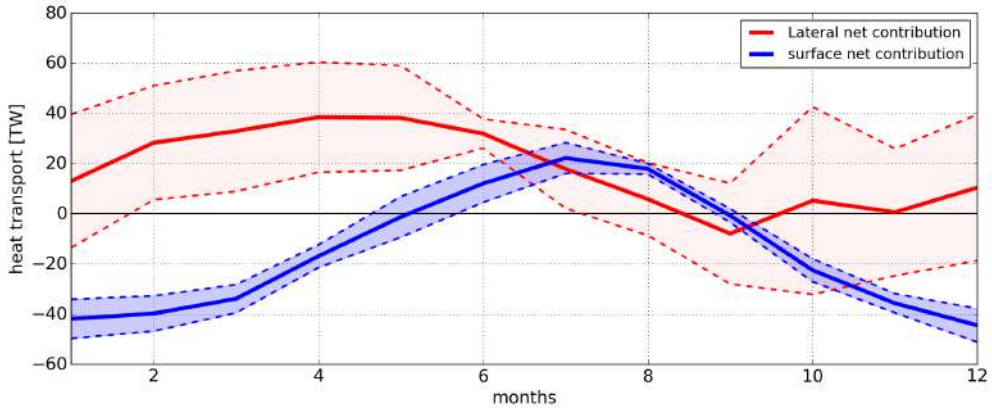

Figure 3.12: *Side-bundaries ($F_H^{boundary}$, red line) and surface ($F_H^{surface}$, blue line) net heat variability (in PW) for the period 2008-2017. Light-shaded areas and dashed lines show the standard deviation for every month.*

On average, in the period 2008-2017 the advection of waters is an order of magnitude bigger than the surface term, suggesting that the magnitude is mainly lead by the boundaries variability.

To analyze the inter-annual variability the first step consists in identifying anomalous years in the 2008-2017 decade, i.e. that exhibit a big deviation from the 2008-2017 mean, and then evaluate the role of the aforementioned processes in leading the observed changes.

In Fig. 3.13 the mean anomaly of each year is presented, aiming to capture the spatial distribution of the anomalies. We observe that in 2010 (a 'warm' year) and 2015 (a 'cold' year) the anomalies extend all over the shelf and in the ISI, while in the following years (2011 and 2016) opposite anomalies in the shelf and over ISI are present.

Since in some years an opposite behavior is noticeable between the shelf and the open ocean temperatures, the 2008-2017 temperature time-series in these regions is analyzed. The shelf has been further divided in an upstream and downstream region (as shown in Fig. 3.14), to capture the differences in the properties of the shelf north and south of Sermilik fjord. This latitude has been chosen as a demarcation line to both equally divide the shelf, and to allow us to evaluate the variability of the waters that feed the Sermilik fjord (numerically implemented in Chapter 4).

The time series of temperature is shown for the 2008-2017 period, as a spatial average over 0-400mt in depth and over three different regions: ISI (as in Fig. 3.1a), 'upstream' and 'downstream' (as in the colored regions Fig.3.14)(Fig. 3.15). The same time series where the mean seasonal cycle has been subtracted is shown in Fig. 3.15b to highlight the anomalies. ISI is here shown because it is likely a source of temperature variability on the shelf. We want to see also if the correlation changes significantly between ISI and 'upstream' and ISI and 'downstream'. ISI region has been chosen as the region north of 60 °N where the bathymetry depth exceeds 1000 mt.

We find that both regions on the shelf are strongly correlated to the variability of the Irminger Sea interior, due to the waters on the off-shore part of the shelf, that are recirculating from the Irminger Current, carrying the temperature and salinity properties from the ISI.

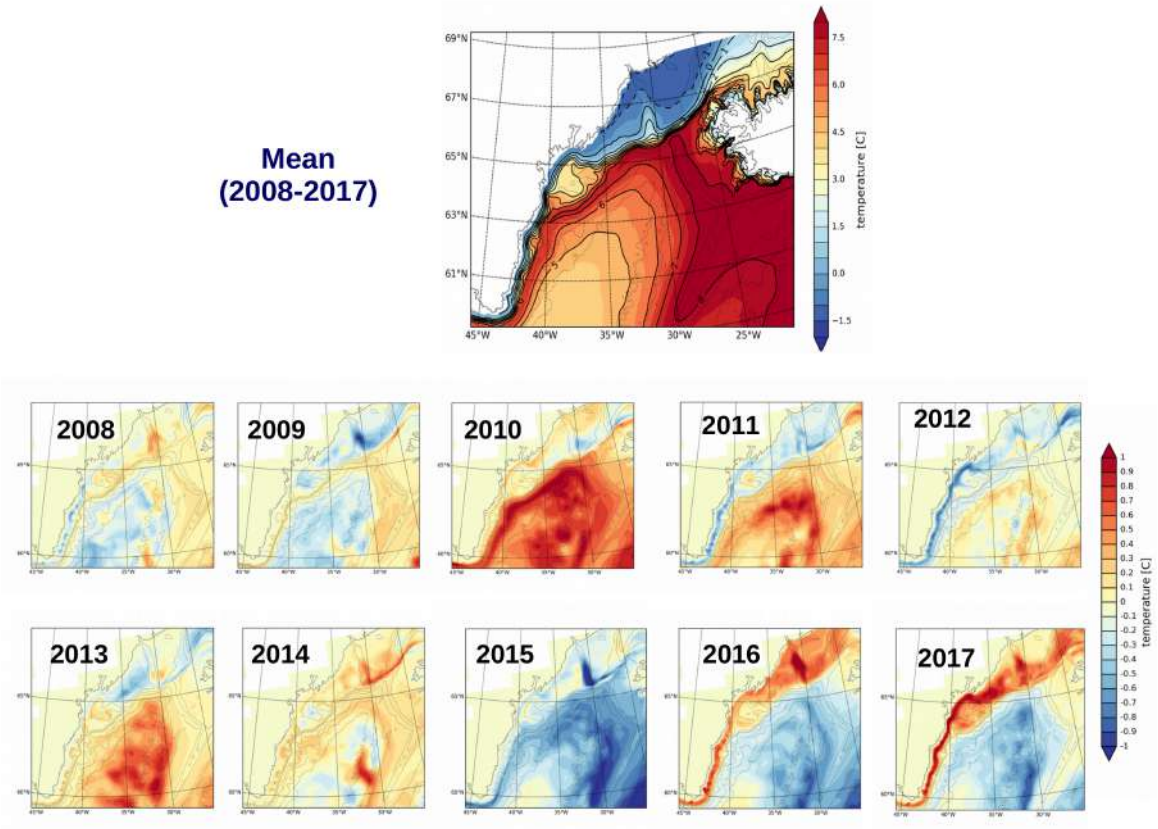

Figure 3.13: *Upper panel shows mean temperature averaged over the first 250 mt for the period 2008-2017. Lower panels show the yearly anomaly with respect to the mean for each year 2008-2017.*

To better understand the variability due to other factors than the Irminger Current, we selected an 'in-shore' region on the shelf, removing from the same analysis those regions on the shelf deeper than 250 meters. In this way we exclude a fraction of the AW component that typically sits on the slope of the shelf, that can mask the PW variability coming from North when averaged. Additionally, in doing so, we separate those water that are able to intrude in Greenland Fjords such as the Sermilik fjord, and most likely affect the sea-ice margins. The contour of the region is indicated in Fig.3.14 and the results are shown in Fig. 3.16. The red line, indicating the Irminger Sea Interior variability, is the same in all plots.

We observe that the variability of the 'in-shore' region is different between the

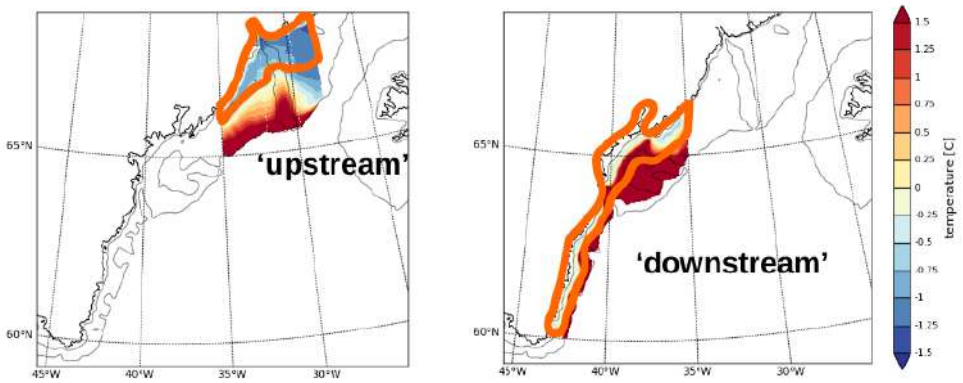

Figure 3.14: *Temperature averaged over 0-100 m for the period 2008-2017 for 'upstream'(left panel) and 'downstream' (right panel) regions. Black lines identify 400 meters contour bathymetry. Orange line defines region were the shelf is shallower than 250 m.*

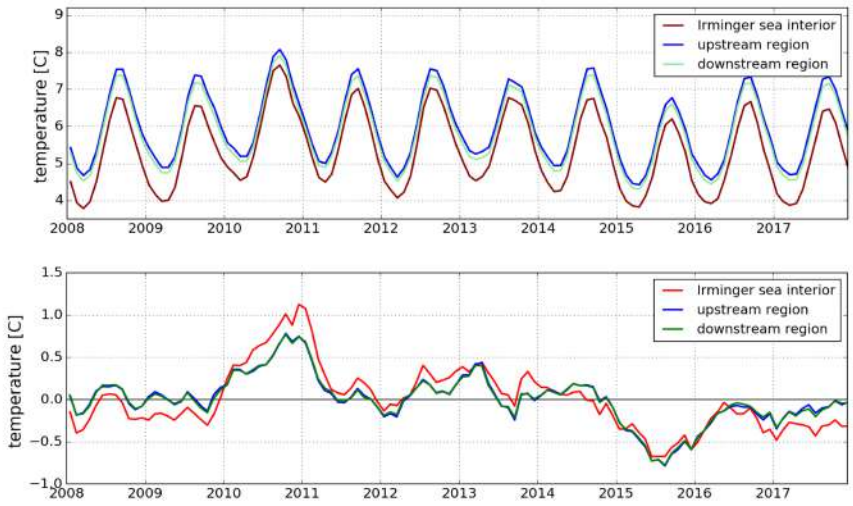

Figure 3.15: *Irminger sea interior (red), upstream region (blue) and downstream region (green) (a) temperature variability in the first 400 meters and (b) temperature anomalies in the first 400 m.*

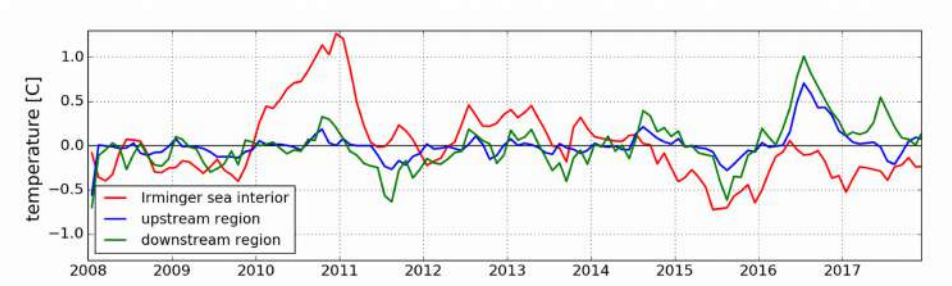

Figure 3.16: *Irminger sea interior (red), upstream 'inshore' region (blue) and downstream 'inshore' region (green) (a) temperature variability in the first 400 mt and (b) temperature anomalies in the first 400 m.*

'complete' shelf regions and the ISI. For various years (e.g. 2008, 2009, 2012-2014), the inshore part shows the same temperature changes as the Irminger Sea Interior, but for some other years (e.g. 2010, 2016) the difference is higher, suggesting that another mechanism concurs to drive the temperature variability in that area. We thus select specific years, either in which (I) the anomaly is high in the whole shelf or (II) the anomaly in the 'in-shore' region differs greatly from the one from the ISI region.

Years 2010 and 2015 exhibit a positive and negative anomaly over both the shelf and the ISI region (Fig. 3.15-3.16) . In 2011 and 2016 the variability in the 'in-shore'part diverges greatly from the ISI variability.

In order to take into account the potential role of the recirculating Irminger Current that comes from the Irminger basin in advecting heat onto the shelf, we evaluate the exchange of heat fluxes with the atmosphere over the ISI region, mainly in years 2010 and 2015, years that exhibit a temperature anomaly that ranges from the shelf to the Irminger Basin (Fig. 3.13).

Fig. 3.17 shows. We show heat fluxes averaged spatially over the Irminger Sea Interior for extended winter months, namely December January, February and March in Figure 3.17.

In 2010 we observe that the heat fluxes over ISI (green bars) exhibit a positive anomaly (i.e. more heat than 2008-2017 average is absorbed by the ocean) that is associated with higher temperatures in the ocean. Similarly, 2015 exhibits the same qualitative correlation between heat fluxes and temperature anomalies but with opposite anomaly sign: 2015 has negative heat flux anomaly and lower than

normal temperatures in the ocean. This means that the high and low temperature observed in 2010 and 2015 are associated with anomalously warmer and colder atmospheric temperatures at the surface in winter. This is in perfect accordance with 2015 being the first year of anomalous convection of this period in ISI, that is being caused by these anomalous heat fluxes (Fig. 3.17) [35]. We also see that, even though 2016 and 2017 have been years of deep convection in the ISI, they are not associated with great anomalies in the heat flux exchange from the atmosphere, consistently with observations [42].

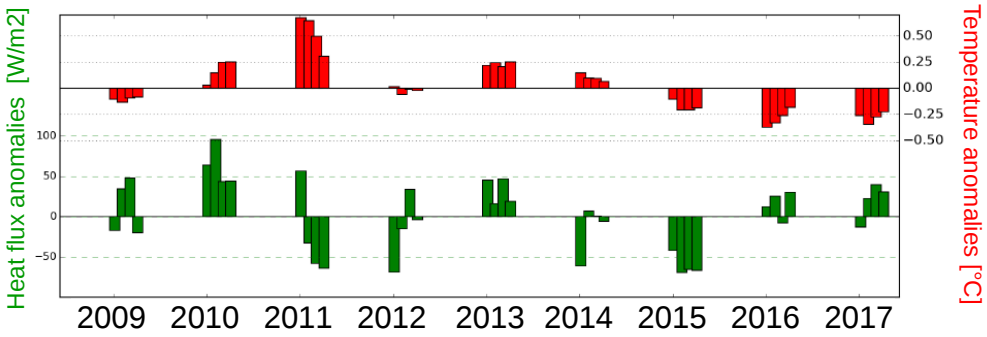

Figure 3.17: *Atmosphere-ocean surface heat fluxes (green bars) and 0-400 mt ocean temperatures (red bars) for December, January, February and March of each year from 2009 to 2017, averaged over ISI region.*

Analyzing the mass budget components singularly, in Fig. 3.18 is shown the volume net contribution of each transect in determining the content of the shelf. The sum of them is $F_M^{boundary}$. All the different contributions are here shown as positive in order to compare them, even though the net Cape Farewell is negative, as outward from the box. The outward volume through CFS is the sum of LS and DSS components. Not only the amount of waters entering from LS is one order of magnitude bigger the one coming from DSS, but also the CFS variability is strongly correlated to the LS variability, due to the way the box is constructed. It is worth noting that not all the majority of waters entering the box flows over the shelf,that helds the EGC, flowing southward along the slope. In Fig. 3.19 the decomposition of the net lateral volume in its components (L1, L2, L3, L4) is presented. The majority (around 60%) of the lateral water enters from north

through L4, followed by the contribution of L3 and L1. L2 section gives a small contribution due to its position, size and direction.

The total amount of water that passes through this box has a positive trend

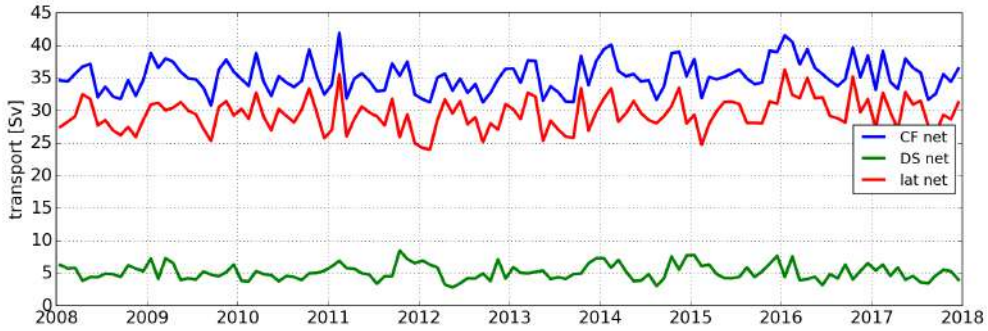

Figure 3.18: *time series of net volume transport through Cape Farewell (blue), Lateral (red) and Denmark Strait (green) for the period 2008-2017.*

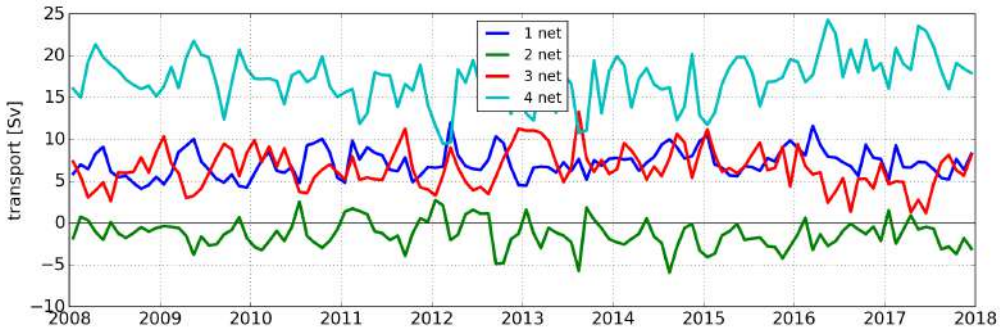

Figure 3.19: *LS net volume variability for the period 2008-2017 decomposition in L1 (blue), L2 (green), L3 (red) and L4 (lightblue) components.*

(around 7% from 2008 to 2017), due primarily to the LS term, while the DSS contribution does not show a clear trend. A small fraction (1-2 Sv) of the Irminger Current entering L4 goes up north through DSS and thus does not affect the shelf properties. The positive inward IC trend can be explained by the recent strengthening of the subpolar gyre [46].

In Fig. 3.20 the 2008-2017 heat fluxes variability from atmosphere-ocean exchange (blue line), lateral and DS sides intake of advected heat (red and green line respectively) are shown. To shed light on the relative role of each component in

driving variability, the same plot but for anomalies is presented in Fig. 3.21. The anomalies here shown are low-pass filtered through an 8-month running-average in order to highlight the inter-annual variability.

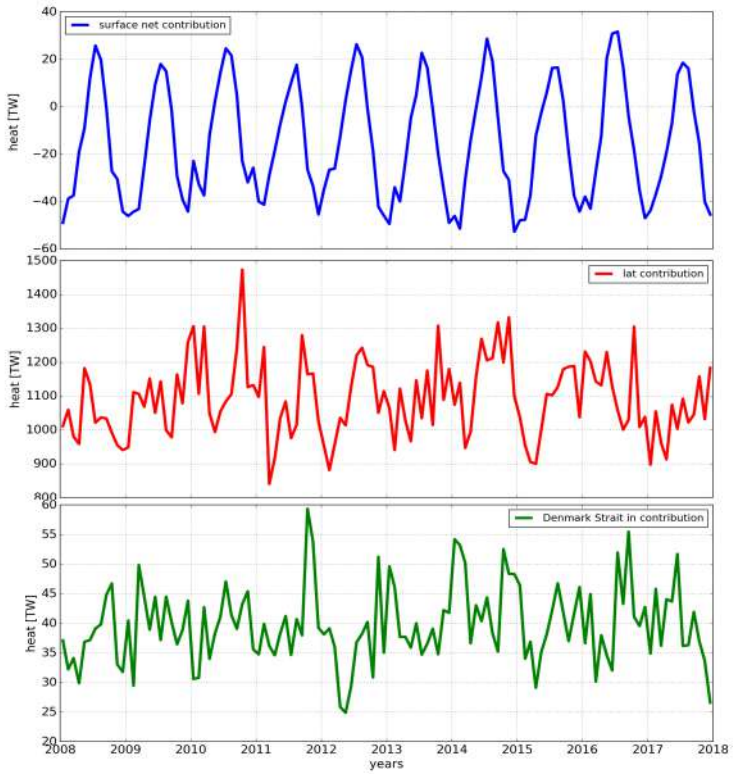

Figure 3.20: *Surface heat budget for each year of the 2008-2017 period (thin colored lines) and for the 2008-2017 mean (black bold line). Values are in TW.*

The next step is to isolate only the water that is able to go on the SE Greenland shelf, and may cause the observed anomaly and the 'in-shore' deviation. Therefore only the 0-250 mt portion of lateral boundaries is considered (Fig.3.23).
Similarly, in Fig. 3.24 the heat transport of those waters that we expect to go on the shelf is shown: we chose cold (T $<$ 3°C) and shallow ($<$ 250 meters) waters. Both poleward and equator-ward waters are considered, since it is present a quasi-stationary eddy (Fig. 3.22) in the shallowest part of the shelf that must be ruled out from computation.
We observe that in the model DS waters exhibit a volume variability that ranges

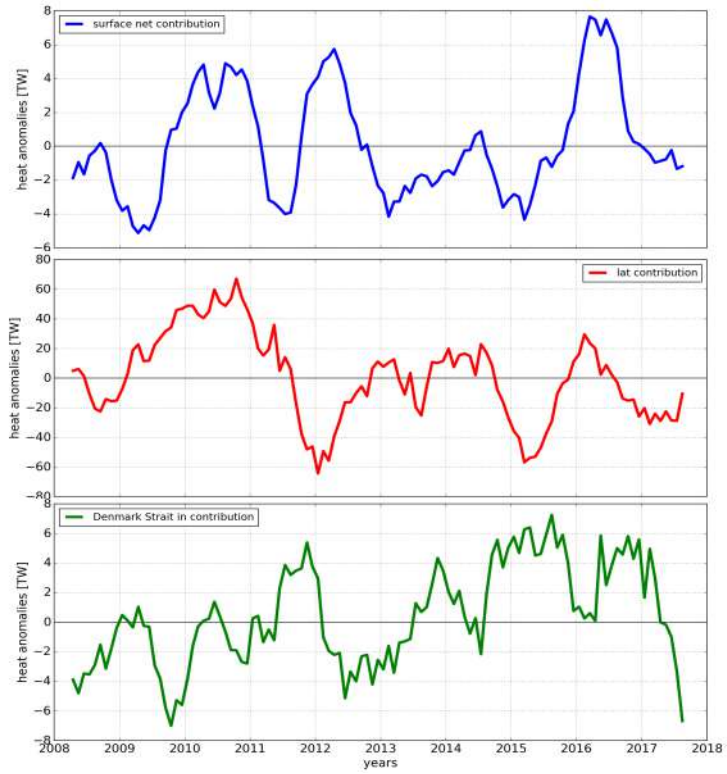

Figure 3.21: *Surface heat budget for each year of the 2008-2017 period (thin colored lines) and for the 2008-2017 mean (black bold line). Values are in TW.*

from 2 to 4, with an average of 3 Sv in the 2008-2017 period. Steur et al. (2016, [47]) quantified the upper Denmark Strait volume transport in 2011-2012 to be around 2 Sv, and the total to be less than 5 Sv. The model therefore appears to overestimate the transport during that period, but still gets the order of magnitude and the right seasonality of the volume.

Focusing on the years of interest, i.e. 2010-2011 and 2015-2016, we investigate which are the processes that potentially drive the temperature anomalies observed over the shelf (Fig. 3.13). Starting with the lateral side (Fig.3.23), we see that 2010 shows a positive anomaly, meaning more heat is advected in the box by the IC, while 2011 is a year of transition between a positive and a negative anomaly, with a mean value that's around the mean climatology. On the other hand, 2015 shows an enhanced negative anomaly, while 2016 exhibits a variability that is

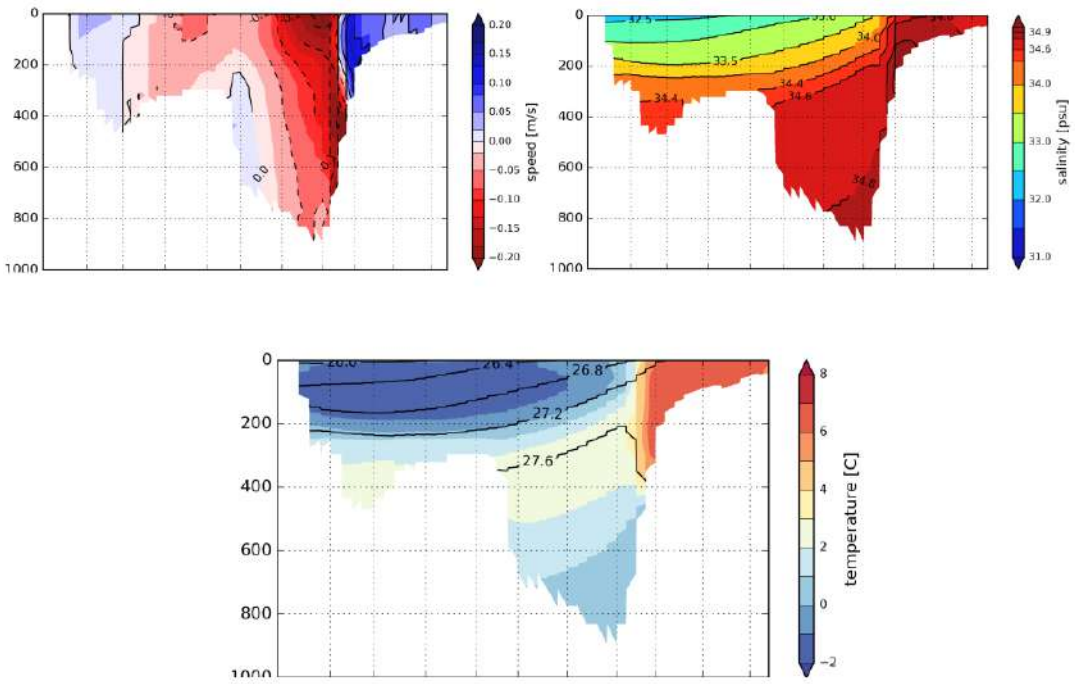

Figure 3.22: *Velocity (upper left panel), temperature and density contours (lower central panel) and salinity (upper right panel) at Denmark Strait transect averaged from 2008 to 2017.*

consistent with the 2008-2017 climatology.

For the advection of heat through DS over the whole period a clear positive trend is visible, starting from mid-2013 until 2017. In both 2010 and 2011 the anomaly is negative (with a mean value of −4 TW), meaning that a small amount heat is advected through DS. This can be explained by less amount of water, or colder water. From the volume transport through that region it is clear that the process behind such negative anomaly is the lesser advected water form the DS.

During 2015, DS transport anomaly is slightly positive (with a mean value of +2 TW) and still consistent with the 2008-2017 climatology, while in 2016 (and at the beginning of 2017) we have a positive anomaly averaged to +7 TW.

However, 2016 is also characterized by strong negative anomaly of sea ice export (Fig. 3.26), leading to 6 months of sea ice absence on the shelf (Fig. 3.25). This absence of sea ice is reflected on the enhanced sea-atmosphere heat fluxes (dark-blue line in Fig. 3.21) on the shelf, causing the waters on the surface to absorb

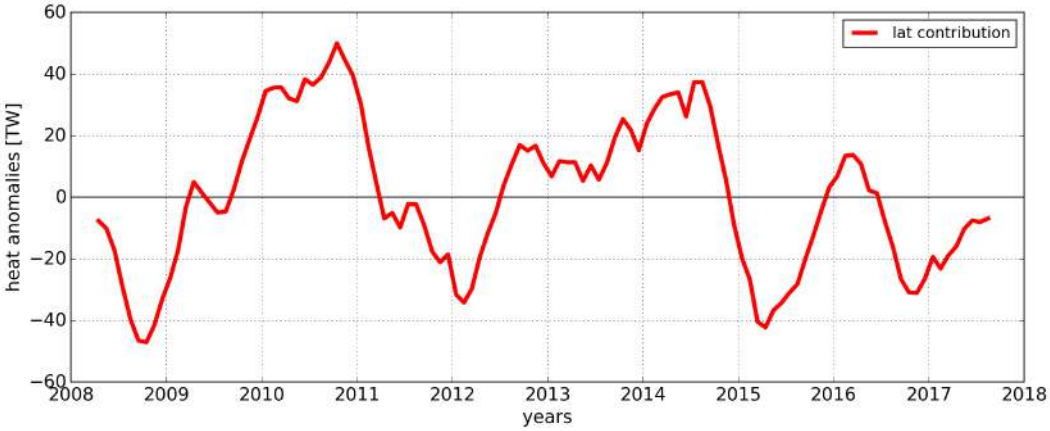

Figure 3.23: *Shallow (0-250 mt) waters heat transport anomaly computed over the lateral sections. Anomalies are computed by subtracting the 2008-2017 climatology to the variability.*

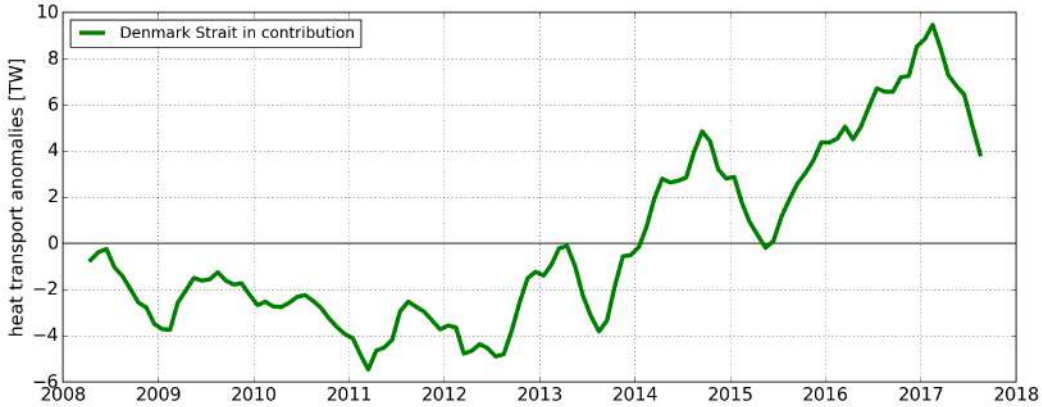

Figure 3.24: *Cold (T<3 C) and shallow (0-250 mt) waters heat transport anomaly computed through Denmark Strait. Anomalies are computed through Denmark Strait by subtracting the 2008-2017 climatology to the variability.*

more heat than average. This confirms the hypothesis that 2010 and 2015 are years where the shelf is mainly driven by the AW coming from the IC and years 2011 and 2016 are driven by water and ice anomalies advected from Denmark Strait.

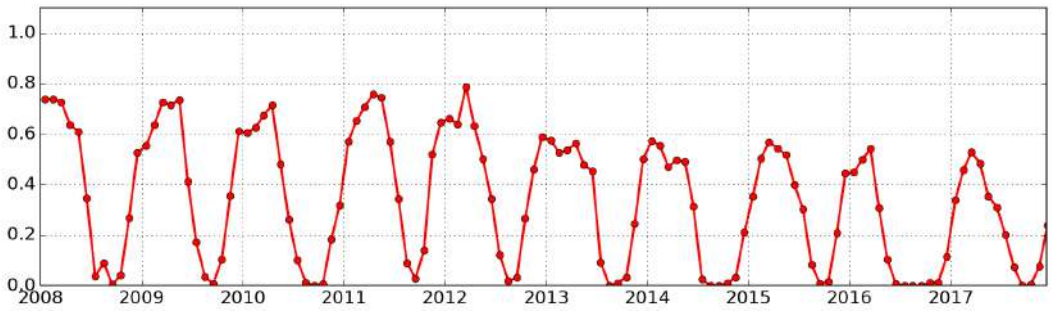

Figure 3.25: *Sea ice concentrations averaged over the SE Greenland shelf.*

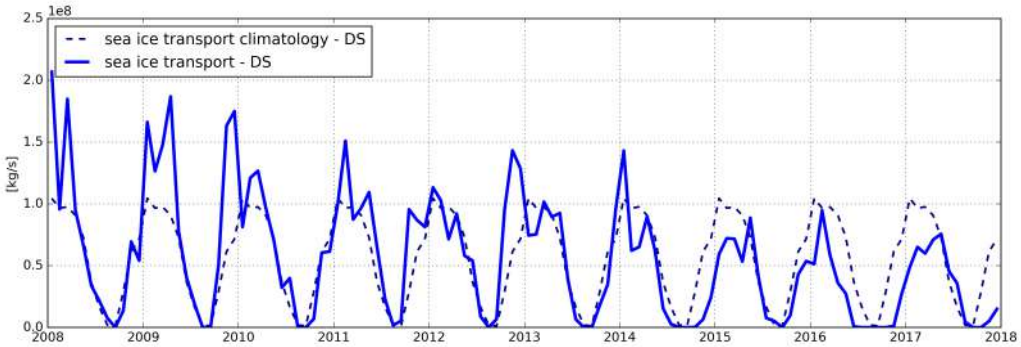

Figure 3.26: *Sea ice mass transport through Denmark Strait. Blue bold line indicates volume variability, while dark-blue dotted line the seasonal climatology 2008-2017.*

3.4 Summary

A global configuration of the NEMO ocean model, GLOB16, has been validated and used to provide the first description of the hydrography and dynamics of South-East Greenland Shelf on inter-annual variability during the period from January 2008 to December 2017. We have shown that GLOB16 is able to replicate the temperature variability on inter-annual timescales, capturing exceptional years of deep convection in the Irminger Sea and the associated changes in temperature. Furthermore, the model is able to represent the variability of ocean temperature and atmospheric heat fluxes over the ISI region and the variability of the sea ice advected from the Arctic ocean on the shelf.

We also found negative significant trends in sea ice concentrations on the shelf, confirming that our model, forced with the JRA55-do atmospheric reanalysis, replicates the unique features that link the Arctic and the sub-polar Atlantic variability on the SE Greenland shelf. Even though some minor discrepancies are present in replicating the convection in the ISI region and the correct magnitude of the sea ice presence on the shelf, our analysis shows that the model configuration is a proper tool to analyze the major drivers of the simulated inter-annual temperature variability on the SE shelf.

We focused on years 2010, 2011, 2015 and 2016, when the behavior of temperature on the shelf departs significantly from the climatology 2008-2017 in order to identify the processes causing the observed variability. We found that both the incoming Irminger Current variability and the advection of waters and sea ice through Denmark Strait into the shelf are associated with temperature anomalies on the shelf. In the first case, during years 2010 and 2015, anomalous positive (negative) atmospheric heat fluxes over the Irminger Sea Interior cause the ocean to warm (cool) due to enhanced (diminished) exchange with the atmosphere. This causes the mixed layer depth to increase (decrease) resulting in exceptional years of deep (shallow) convection in the ISI region and warm (cold) waters advected on the shelf through the recirculating IC.

The main drivers of the variability in years 2011 and 2016 are the advected anomalies from the Arctic. Heat transport variability in these years is strongly anomalous through the Denmark Strait, and in 2016 it is associated with little or no sea ice mass transport and a lack of sea ice on the entire shelf.

A further aspect we would like to address in the future is the definition of a temperature and salinity structure of the East Greenland Coastal Current in different regimes of variability (e.g. Arctic ocean-driven, atmosphere-driven) to understand the changes occurring on the SE Greenland shelf. However, having used only one decade in this analysis this can not be performed since the length of the time series does not allow us to analyze more than one year with particular conditions. An extension of the current analysis would be to analyze a longer time-series from the output of the numerical experiment, that is available from 1975 to present, and to expand the mechanisms analysis.

Chapter 4

Numerical simulations of the Sermilik fjord dynamics with an high resolution model

4.1 Introduction

Greenland glacial fjords are characterized by a marine-terminating glacier that represent a connection between the Greenland Ice Sheet (GrIS) and the ocan outside. They are a critical feature of the Greenland coast, importing oceanic heat and exporting meltwater into the ocean. Greenland glacial fjords are usually long and narrow (50-100 km long and 5-10 km wide), and the properties of the water inside the fjords resemble the water masses the are found on the continental shelf right outside them. [48]
On the South-East Greenland shelf, properties of the water inside the fjords are highly affected by those on the shelf, where cold, fresh water of Arctic origin (Polar Water) overlies warm, salty water of Atlantic origin (Atlantic Water). The ocean current system on the SE Greenland shelf is characterized by the presence of the East Greenland Current (EGC), formed by the Arctic-origin, that flows southward along the shelf-break next to the Atlantic-origin, salty and warm Irminger Current (IC).
The EGC merges with the recirculating portion of the Irminger Current to form a flow that is often referred to as the East Greenland/Irminger Current. On the inner shelf, the East Greenland Coastal Current (EGCC), possibly branching from the EGC south of the Denmark Strait or further

upstream, advects cold, fresh water equator-ward towards Cape Farewell ([49], [50], [12]).
GrIS discharge is important for the freshwater budget of the North Atlantic, and potentially impacts the global ocean, through the Atlantic Meridional Overturning Circulation [29]. The recent glaciers retreat and mass volume loss over the last decades, resulted in a significant increase of the input of freshwater into the fjord. The increase in freshwater input modifies fjord hydrology and influences the dynamics, and gets particular relevant in a changing climate. Since most of the freshwater discharged from Greenland passes through the fjords, investigating the glacier melt rates and its properties is critical to understand the dynamics within the fjord [51].
However, the dynamics of glacial fjords is still poorly understood. First of all, they are found in remote regions, thus obtaining data is difficult and costly, and also challenges posed by calving glaciers and icebergs are present. In situ observations of the dynamics within the fjords are difficult for a variety of reasons: runoff into glacial fjords is not directly measured, but estimated with regional models and reanalysis that often differ significantly (e.g.,ref7 ref8) and the glacier-driven circulation due to the input freshwater, having often have weak velocities, it is hard to measure. Additionally, glacial fjord dynamics are complicated by diverse time-dependent flows, like tides and externally forced circulations, that can mask the signal of glacier-driven flow [52].
For these reasons numerical models are employed as a key tool in investigating the processes in such small and remote areas.
In this chapter, we present a high-resolution regional ocean model, implemented to better understand the processes that control properties and circulation within the fjords and the exchanges with the shelf water, crucial to assess the ocean's role in triggering the acceleration of Greenland's outlet glaciers and the export of melt-water.
The regional configuration employs a horizontal resolution of $1/48^\circ$ with 98 vertical levels with the objective to properly reproduce the ocean characteristics and dynamics inside the fjord. Our interest focuses on the Sermilik fjord located in south-eastern Greenland where a relatively long-record of observations are available.
The Sermilik fjord is one of the largest fjords in the South-East coast of Greenland, it stretches inland in a roughly northern direction and splits

into two branches at its head. Its waters are fed by glaciers Helheim Fenris and Midgard. Helheim glacier is the fastest flowing glacier along the eastern edge of Greenland Ice Sheet and one of the island's largest ocean-terminating rivers of ice. It accounts for $\sim 20\%$ of the ice sheet's mass discharge [53].
Sermilik fjord is the narrow connection between the continental shelf waters in the western Irminger Sea to the inner glaciers. Greenland's glacial fjords share many basic features with river estuaries of lower latitudes, but, unlike those, liquid freshwater from the ice sheet is exported into the ocean via a system of rising buoyant plumes driven by submarine melting and sub-glacial discharge. These plumes rise near the glacier front, entraining ambient water, until they reach the surface or their level of neutral buoyancy.
The Sermilik fjord is directly connected to the continental shelf without a sill, whereas they are typically found in Greenland glacial fjords, and is characterized by a peculiar bathymetry outside its opening with by deep troughs. These two features help channeling warm Irminger Current water toward the Greenland coast.
A critical part of the glacier discharge is the freshwater discharged in solid form as calving icebergs, and other inputs of freshwater at the surface include terrestrial runoff, precipitation, and sea ice melt, not included in this analysis.
Additionally, some in-situ measurements are available and can be used as comparison with numerical experiments. For these reasons the Sermilik fjord has been chosen to study and numerically simulate the mechanisms governing the exchange of mass and heat between the ocean and the fjord itself.
The chapter is structured as follows. In the next section, a description of the Sermilik fjord dynamic from observation is provided, followed by a description of regional ocean model and experiment designs. Then, we present the main results, and summary and discussion follows in the last section.

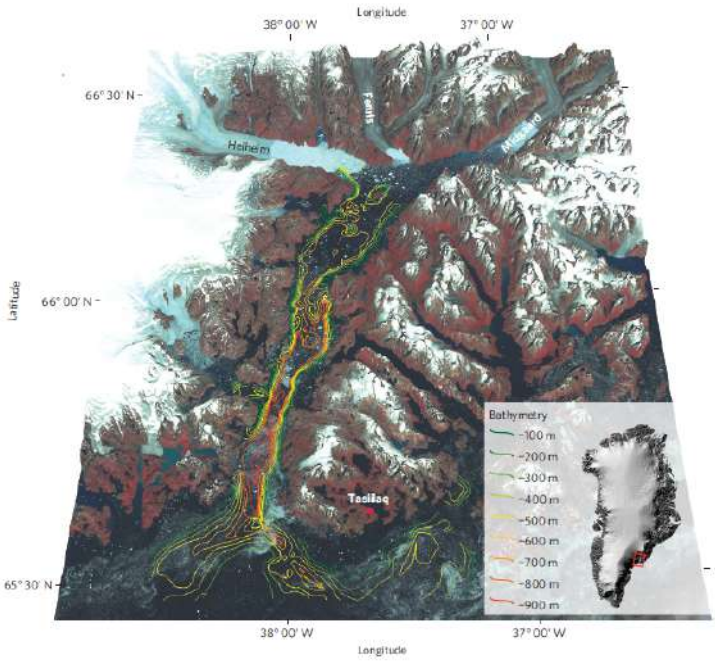

Figure 4.1: *Sermilik fjord from satellite with bathymetry superimposed. [54]*

4.2 Sermilik fjord circulation

Here we summarize the dynamics of the Sermilik fjord circulation, (e.g. as in [48], [52]).
The fjord circulation is influenced by a number of factors: tides, buoyancy forcing from the glacier, iceberg, surface fluxes, along-fjord winds [55] and the exchange with the continental shelf. The dominant dynamical processes of this circulation are identified in the buoyancy-driven circulation, the intermediary circulation and the deep-water renewal, as schematized in Figure 4.2.

- Freshwater discharged from glaciers forces a **buoyancy driven circulation** that is analogous to the estuarine circulation found in many estuaries and fjords. Unlike typical estuarine systems, two component of the total discharge, the sub-glacial discharge and the submarine melt, involve the discharge of freshwater at depth and result in turbu-

lent plumes that entrain ambient water as they rise. Buoyancy-driven flows in Greenland's fjords have a strong seasonality because they depend on the discharge of surface melt at the base of the glacier, that changes seasonally. Sermilik fjord buoyancy forcing from glacial inputs is likely to have an opposite seasonality from the shelf forcing in the Sermilik fjord region.Surface runoff from the ice sheet will only form when air temperatures are above freezing, which is primarily June-August (e.g., [56]). Modeling studies indicate that submarine melting of glaciers increases with sub-glacial discharge (e.g., [57], [58], [59]) which suggests that the seasonality of submarine melting might match that of runoff.

- **Intermediary circulations** identifies the shelf-driven flows that occur above the sill depth. They are driven by density variations outside the fjord, which can originate from along-shore winds (upwelling or downwelling) or density anomalies advected past the mouth of the fjord. Intermediary circulation are highly effective at flushing the waters above the sill depth and can be an order of magnitude larger than estuarine flows [60]. The southern-east Greenland shelf region is characterized by the presence of intense along-shore winds that result from low-pressure systems encountering Greenland's steep topography. These winds, usually from the north-east, cause downwelling outside the Sermilik fjord. Additionally, they exhibit a strong seasonality: in non-summer months there are frequent highly energetic events, while the winds are weaker and the energetic events less frequent during summer [[52]. It is worth noting that also strong down-slope events are present on the Sermilik fjord, due to katabatic winds that accelerate over the steeper slopes of Greenland [55]. Even though these down-slope wind events influence the circulation of the fjords, they are sporadic, while along-shore winds are nearly continuous throughout the year. For this reason, their influence in the fjord dynamic will be considered negligible in this analysis.

- **Deep water renewal**, below the sill depth, occurs periodically by the inflow of denser water from the shelf over the sill, which entrains relatively fresher water from above. For Greenland's glacial fjords, where

sub-glacial discharge and submarine melting introduce freshwater at depth, one might expect the residence time to be reduced in respect to that of a non-glacial fjord, due to the entrainment of deep water into the buoyant plumes. The understanding of processes governing the renewal of water in the fjords as well as the transport of heat toward the glacier and export of glacially modified waters is limited, and estimates of deep-water residence time for the waters below the sill ([61], [62]) show diverging conclusions ranging from monthly to yearly time-scales.

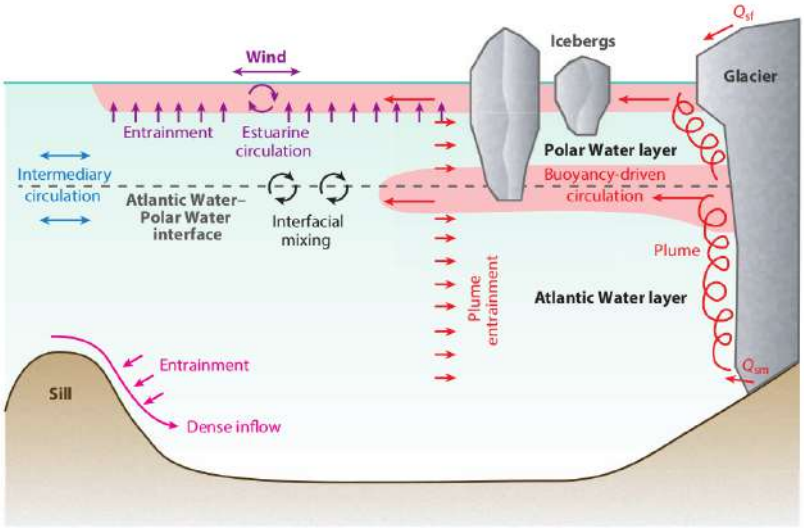

Figure 4.2: *A schematic representing the different circulations in a Greenland glacial fjord. Red indicates the buoyancy-driven circulation resulting from the submarine melting/discharge and surface runoff. In purple the estuarine circulation resulting from surface runoff and in blue the intermediary circulation. Pink indicates the circulation generated by the dense inflow over the sill involved in the deep water renewal. From [48].*

The Sermilik fjord-scale circulation is likely determined by the interaction of the intermediary flows with the buoyancy-driven flows. At present there is no simple theory that combines these two circulations and predicts which mode may dominate in a articular fjord, but a strong seasonality in fjord conditions has been observed ([52], [61]) leading to a separation of the yearly conditions in a summer regime and non-summer one, as demarcated

by dashed vertical lines in Figure 4.3.
In winter, the fjord exhibit a two-layer system, with peak stratification between 150 and 250 m, while in summer they observe the fjord to be more strongly stratified and with a stratification that increases toward the surface. In particular, during summer and fall months, the fjord waters above 200 m appear to be modified by mixing with both submarine melting and runoff, suggesting that the upper layer is a mixture of deep AW (upwelled through mixing) with glacial freshwater. On the contrary, in winter and spring, there is no modification due to runoff and, in the upper layer, fjord water characteristics resemble the shelf PW ones. The intermediary circulation in Sermilik fjord have been observed through numerous mid-fjord velocity measurements (9,17,20). In particular, [61] showed that in non-summer months (from September to May) the glacier melt rate varies substantially and depends on externally forced ocean flows that rapidly transport changes on the shelf towards the glaciers' margins. These velocity pulses are associated with shelf pycnocline fluctuations. Shelf density fluctuations, in turn, are primarily associated with alongshore shelf winds ([61]).
On the other hand, [52] showed that in summer months these shelf-forced flows are much less energetic during the summer. This coincides with a reduction in wind forcing from the shelf. Since the Sermilik fjord is characterized by a strongly stratified water column, it have been observed that intrusions of glacially modified water are found at mid-depths, typically between the AW and PW layer, both in winter and in summer ([63]), as shown in Fig. 4.4.

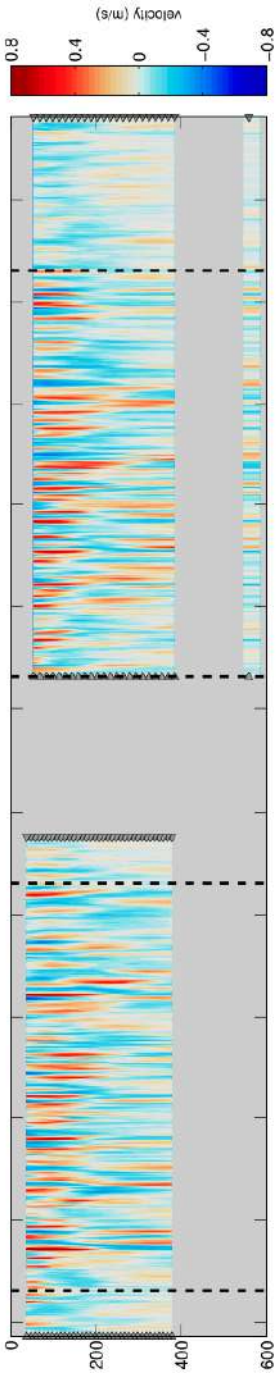

Figure 4.3: *Two-year records from mid-fjord moorings from September 2011 to August 2013. Colors are along-fjord velocity, with positive values toward the glacier and negative toward the fjord mouth. Black dashed lines separate the summer and non-summer seasons. Plot is taken from [52]*

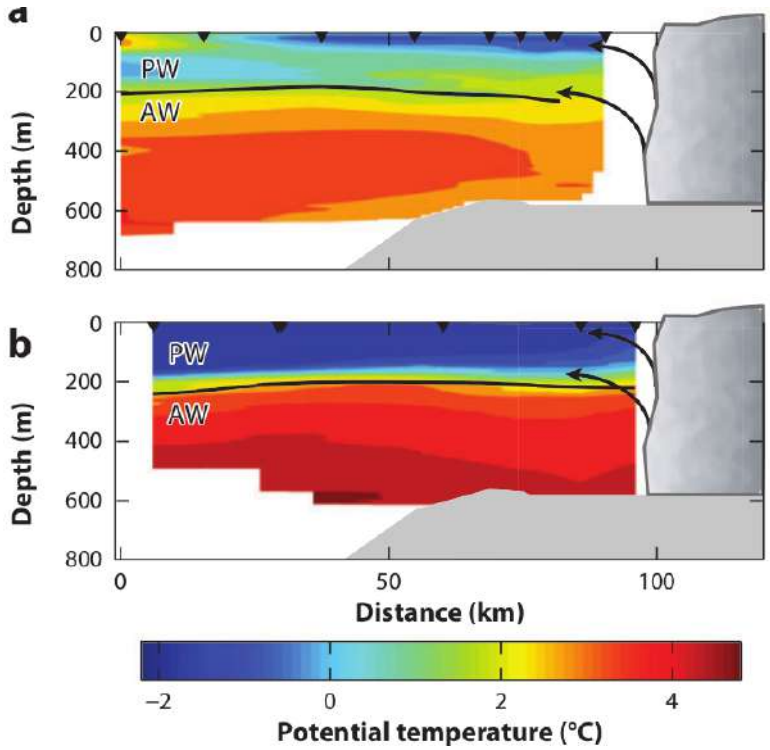

Figure 4.4: *Potential temperature distribution from an along-fjord section of Sermilik Fjord in August 2009 (a) and March 2010 (b). Black arrows indicate the intrusions of glacially modified waters. From [48]*

4.3 Methodology and experiments design

4.3.1 SURF model characteristics and work-flow

In order to implement a regional model in the fjord area at spatial resolution adequate to resolve the fjord dynamics, we used the numerical platform of the Structured and Unstructured Relocatable ocean model for Forecasting (SURF, [64]).
SURF is designed to be embedded as the 'child' in any region of a large-scale 'parent' ocean configuration at lower spatial resolution. The 'parent' model provides initial and lateral open boundary conditions to the child one. It is possible to include multiple one-way nesting with increasing resolution consecutive nested models, starting from the large-scale parent model. Each child model can have different numerical discretization and physical parameterizations.
SURF includes three basic components: an ocean component with a structured grid hydrodynamic model based on the NEMO framework [**?**]; an ocean component with an unstructured grid hydrodynamic model based on the Shallow water HYdrodynamic Finite Element Model (SHYFEM) model [65]; a wave model based on the third-generation spectral wave model SWAN.
For our regional implementations,we decided to use the NEMO modeling framework (updated to the version 3.6) to be consistent as much as possible to the GLOB16 configurations. In our applications, the horizontal grid is a regularly spaced latitude/longitude grid in a spherical coordinate system: it has coordinates aligned with parallels and meridians with constant spacing in latitude and longitude directions. The grid spacing ratio is set to 3, meaning that the child domain has a grid spacing that is one third the size of the of the parent domain, resulting in a horizontal resolution of $1/48°$, around 1 km in the Sermilik fjord area on the vertical direction, we use z-coordinate 98 vertical layers. The levels distance increases from the surface to the bottom, following a smooth hyperbolic tangent transition.
In our numerical exercises, the vertical eddy viscosity and diffusivity coefficients are computed following the Richardson-number dependent scheme of Pacanowski and Philander (1981). Unresolved vertical mixing processes are represented by a background vertical eddy diffusivity of $1.2x10^{6}m^{2}s^{-1}$ and eddy viscosity of $1.2x10^{-5}m^{2}s^{-1}$. In regions where there might be unsta-

ble stratification, the enhanced vertical diffusion parameterization is used, where this coefficient are replaced by a higher value of $10m^2s^{-1}$. SURF employs the split-explicit free surface (also called time-splitting) formulation [66], that allows to solve the free surface equation and the associated barotropic velocity equations with a smaller time step than the time step used for the three dimensional prognostic variables.
Baroclinic velocities and tracers, depth dependent prognostic variables that evolve more slowly, are solved with a larger time-step $\Delta t = 100$ s; the barotropic part of the dynamical equations, instead, is integrated explicitly with a shorter time-step of 40 sec. The lateral open boundary conditions must be formulated separately for the barotropic and baroclinic modes. The algorithms used in SURF are the Flather scheme for barotropic velocities and sea surface height and the flow relaxation scheme for baroclinic velocities and active tracers. The vertical mixing is achieved using the turbulent kinetic energy (TKE) closure scheme ([67]).
Lateral sub-grid scale mixing for momentum and tracers is parametrized through a bi- laplacian operator. The general workflow of the SURF numerical platform as shown in Fig. 4.5. The model components, inputs data, numerical outputs and several pre and post-processing tools are reciprocally connected. For this study, the source code was ported on the CMCC HPC infrastructure (IBM iDataPlex SandyBridge) in order to access the necessary resources and speed up the simulations.
To implement the SURF configuration and generate the domain grid, the first step consists in the choice of the ocean physical parameters and domain definition, for setting the high-resolution NEMO configuration.
The second step is to provide the required input datasets to SURF preprocessing tool: (I) a bathymetry of the region of interest; (II) coastline; (III) a 'parent' model fields as initial and boundary conditions, together with the atmospheric forcing dataset that will be interpolated onto the child grid. Then, the numerical grid is generated and data are reformatted, in order to compute the atmospheric forcing, bathymetry, boundary and initial conditions datasets on the child grid through interpolation.
To perform the interpolation, a bilinear method is used in the horizontal. The pre-processing phase includes a sea-over-land (SOL) procedure, that extrapolates the 'parent' fields on the coastal areas where the parent model solutions are not defined. This applies also to atmospheric fields in order to

avoid land contaminations near the land-sea boundaries.

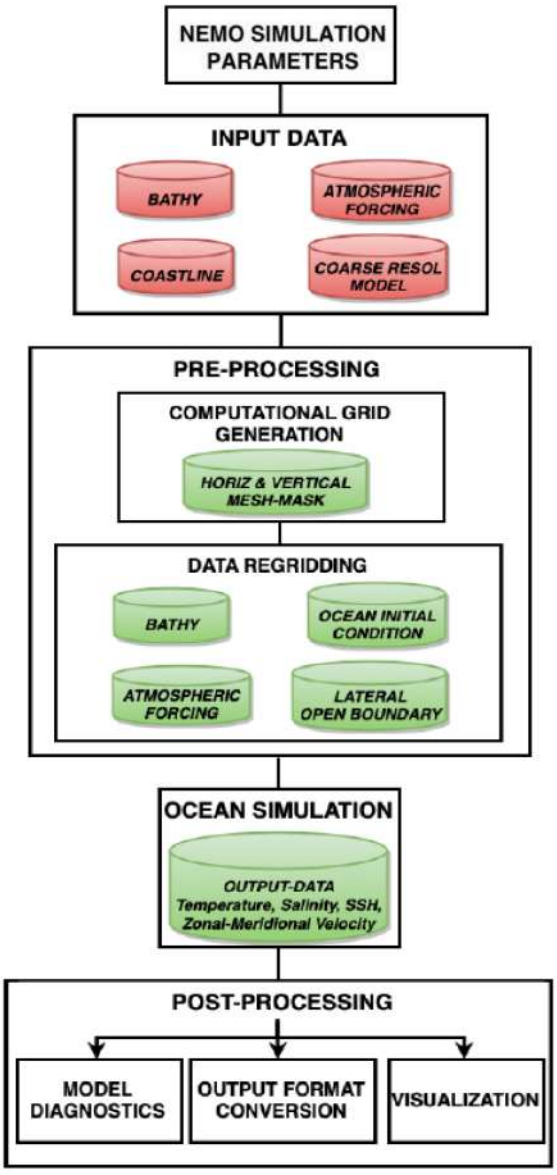

Figure 4.5: *Work-flow of the relocatable ocean model SURF based on NEMO model with the possibility to be coupled to ocean wave model. From [64].*

4.3.2 Experimental set-up

The relocatable modeling system SURF has been implemented in the Sermilik fjord region, encasing the fjord and part of the continental shelf, as shown in Figure 4.6.
Hereafter, High-RES identifies this experiment configuration. Based on the previous results suggesting that this configuration can properly describe the mean state and variability of ocean circulation on the continental shelf outside the Sermilik fjord, GLOB16 is taken as a 'parent' model and its output used to set the initial and boundary condition in SURF.

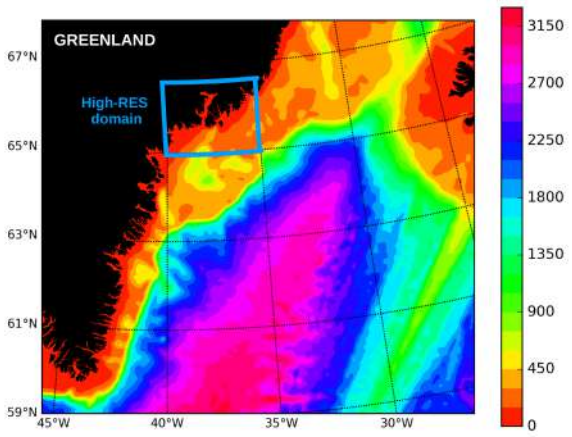

Figure 4.6: *GLOB16 bathymetry (GEBCO) over the whole southern-east Greenland shelf and Irminger Sea (in meters). The light-blue box encases the region of the high-RES experiment.*

The GLOB16 coastal bathymetry is based on the General Bathymetric Chart of the Oceans (GEBCO) One Minute Grid data-set [68], that properly represents the shelf topography, but it is not fine enough to adequately represent the sea floor inside the fjord. In the GLOB16 bathymetry indeed, the Sermilik fjord is too shallow compared to new products where it reaches depths of 900m. Additionally, GLOB16 bathymetry does not present the peculiar bathymetric features on the shelf outside the fjord, essential to form the pathways of AW into the fjord. For these reasons, the High-RES bathymetry is based on a new product, IceBridge BedMachine

Greenland version3, freely available at the National Snow and Ice Data Center (NSIDC, [69]). The output product is generated at 150 m resolution and its spatial coverage includes Greenland and the Arctic (from 60°N to 90°N and from 80°W to 10°E). This data provides a robust representation of the sea topography in the fjord, correctly representing its 3D geometry, and also the topographic features outside over the shelf. The product interpolated on the HighRES grid is shown in Figure 4.7 in comparison to GLOB16 bathymetry. The location of the lateral boundaries of the child domain was carefully chosen to minimize the differences with the bathymetry of the parent configuration, and reduce numerical errors due to the interpolation procedure.

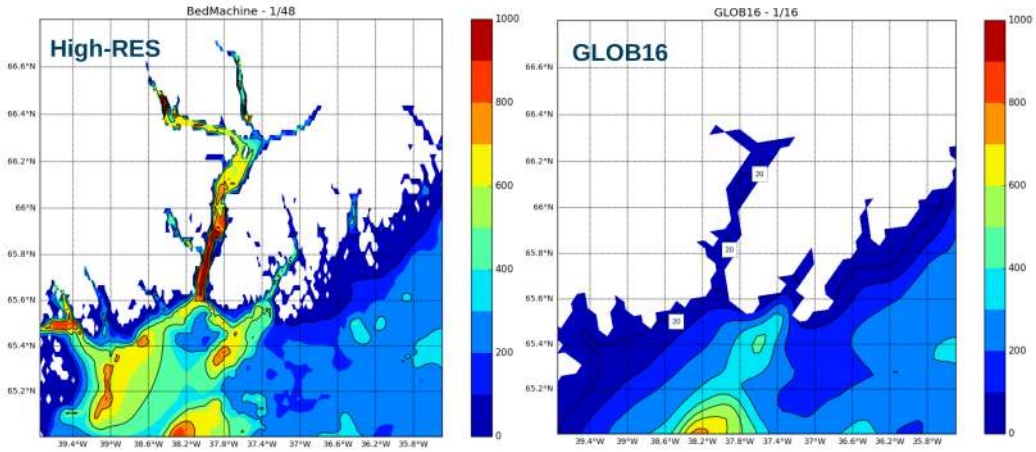

Figure 4.7: *Left panel shows the Sermilik fjord bathymetry as represented by the BedMachine product interpolated on a 1/48 grid (colorbar in meters). Right panel shows the bathymetry in the same region as used in GLOB16 (colorbar in meters).*

The High-RES domain extends from 35°W to 40°W and from 65°N to 66.7°N, for an area of 226 km longitude by 200 km latitude, with 205x107 grid points in the horizontal plane. As in the GLOB16 simulation, the child ocean is driven by the JRA55-do v1.3 surface-atmospheric dataset ([26]), with horizontal resolution of $\sim$ 55 km and temporal interval of 3 h. The spin-up time is defined as the time necessary by the child ocean model to reach a steady state value for the volume average kinetic energy starting from initial and lateral boundary conditions interpolated from the parent model. We have been observed that after a few days of simulation the fjord loses the memory of the IC on depths shallower than 400m. We have set the spin-up at 1 week, being in this way sure to disentangle the nested model from the initial conditions.
Table 4.1 summarizes the main characteristics chosen for the High- RES experiment in comparison with GLOB16. The High-RES experiment has been integrated for two seasons, summer and winter, for 120 days each. The inter experiment (High-RES-W) starts in December 2012, while the summer experiment (High-RES-S) in June 2013, aiming to reproduce a non- summer and a summer regime. Time periods are chosen in such a way that the study of both summer and winter seasons is allowed.

	GLOB16	**High-RES**
domain	global	regional-nested
horizontal resolution	1/16°	1/48°
horizontal resolution (km)	∼4km	∼1km
vertical levels	98	98
output frequency	daily	hourly
atmospheric forcing	JRA55-do	JRA55-do
bathymetry	GEBCO	BedMachine

Table 4.1: Input datasets and characteristics of High-RES and GLOB16 configurations on the SE Greenland shelf.

The years are chosen based on the availability of GLOB16 output. The initial conditions needed from the user are the temperature and salinity (T,

S), Sea Surface Height (SSH), meridional (V) and zonal (U) velocity components. We imposed the same T and S initial conditions all over the fjord, obtained by horizontally-averaging the GLOB16 vertical profiles over the fjord. SSH is directly extracted from GLOB16, and we imposed the V and U fields to be at a state of rest (i.e. velocity equal to zero).

4.3.3 Freshwater runoff implementation

The glacier-driven circulation is a critical factor to take into account when modeling the dynamics of a fjord. The original SURF framework does not include freshwater inputs from land into the ocean. Given the importance of the freshwater runoff in studying the fjord dynamics, we adapted the preprocessing procedure to include the option of inject a runoff into the ocean file as lateral boundary condition.
The treatment of the newly-implemented glacier runoff is based on the NEMO river runoff boundary condition routine, and include the possibility to add river runoff at the surface as generally done in ocean model, but also through a non-zero depth, and with temperature and salinity different from the surrounding ocean he number of model grid-points over which the runoff is spread horizontally and vertically, can be defined. If temperature and salinity are not specified through an input file, the runoff is assumed to be fresh (0 psu), and at the temperature of. the ocean grid box over which it is added. If the depth is not specifically set, the model assumes the depth to be zero, and the runoff is added to the top model cell of the water column. After being read in the temperature and salinity variables are multiplied by the amount of runoff to give the heat and salt content of the runoff.
The volume addition due to the runoff is added to the horizontal divergence. This increases the diffusion term in the vicinity of the mouth of the fjord, thereby simulating a momentum flux. The SSH is calculated using the sum of the horizontal divergence terms, and so the runoff indirectly forces an increase in sea surface height. Near the end of the time step the change in sea surface height is redistributed through the grid boxes, so that the original ratios of grid box heights are restored. In doing this water is moved into boxes below, throughout the water column, so the large volume addition to the surface box is spread between all the grid boxes. For the test exercises

and the experiments presented here, we assume a runoff with salinity of 0 psu, temperature of 0°C at a depth of 200 meters.

	1999	2000	2001	2002	2003	2004	2005	2006	2007	2008	Mean	
SnowModel simulated terrestrial runoff to the Sermilik Fjord including error, 10^9 m^3 y^{-1}	2.9 ± 0.4	5.1 ± 0.8	4.1 ± 0.6	5.2 ± 0.8	3.5 ± 0.5	5.2 ± 0.8	5.9 ± 0.9	5.1 ± 0.8	4.8 ± 0.7	4.2 ± 0.6	4.6 ± 0.7 (11%)	
SnowModel simulated precipitation (e.g., rain and snow accumulation on sea ice) at the Sermilik Fjord surface area (1103 km^2) including error, 10^9 m^3 y^{-1}	0.9 ± 0.1	1.2 ± 0.1	1.7 ± 0.1	1.7 ± 0.1	1.4 ± 0.1	1.4 ± 0.1	1.8 ± 0.1	1.4 ± 0.1	1.5 ± 0.1	1.3 ± 0.1	1.4 ± 0.1 (3%)	
Subglacial geothermal melting, 10^9 m^3 y^{-1}	0.01	0.01	0.01	0.01	0.01	0.01	0.01	0.01	0.01	0.01	0.01 (>0.03%)	
Subglacial frictional melting due to basal ice motion, 10^9 m^3 y^{-1}	0.5	0.5	0.5	0.5	0.5	0.5	0.5	0.5	0.5	0.5	0.5 (1%)	
Satellite-derived ice discharge from the Helheim Glacier including error, 10^9 m^3 y^{-1}	21.7 ± 3.3	22.7 ± 2.5	21.8 ± 2.2	26.8 ± 2.3	28.1 ± 3.8	28.0 ± 2.5	33.8 ± 2.8	25.9 ± 1.8	25.9 ± 2.1	24.3 ± 2.8	25.9 ± 2.6 (65%)	33.9 ± 4.1 (85%)
Satellite-derived ice discharge from the Fenris Glacier including error, 10^9 m^3 y^{-1}	–	2.3 ± 0.5	2.5 ± 0.5	2.6 ± 0.5	2.8 ± 0.5	2.9 ± 0.5	2.8 ± 0.5	2.2 ± 0.5	2.5 ± 0.5	2.4 ± 0.5	2.5 ± 0.5 (6%)	
Satellite estimated ice discharge from the Midgård Glacier including error, 10^9 m^3 y^{-1}	–	3.7 ± 0.7	3.9 ± 0.8	3.6 ± 0.7	4.2 ± 0.8	6.1 ± 1.0	7.9 ± 1.2	7.3 ± 1.2	7.5 ± 1.2	–	5.5 ± 1.0 (14%)	
Freshwater flux to the Sermilik Fjord, 10^9 m^3 y^{-1}	–	35.5 ± 4.6	34.5 ± 4.2	40.4 ± 4.4	40.5 ± 5.7	44.1 ± 4.9	52.7 ± 5.5	42.4 ± 4.4	42.7 ± 4.6	–	40.4 ± 4.9	

Figure 4.8: *Estimates of terrestrial runoff, rain and show accumulation on sea ice, geothermal melting, frictional melting, ice discharge from Helheim, Fenris ans Midgard glaciers. From [56].*

Even though this is not a realistic representation of the glacier runoff properties, a very fresh and cold water input allows us to identify the runoff effects on the water properties within the fjord. In GLOB16, the runoff is distributed all along the coasts (as shown in Fig. 4.9), and its monthly climatology is extracted from the JRA55-do dataset and computed over the 1975-2016 period. Regarding the amount and distribution of the runoff discharged in the Sermilik fjord in the High-RES configuration, the magnitude for both summer and winter months is derived from the data published by Mernild et al. 2010 ([70]).
Specifically, Mernild et al. 2010 provided value of the Sermilik runoff for the 1999-2008 period, based on satellite-observed ice velocities, estimated ice thickness and total ice discharges (iceberg calving plus submarine melting, Figure 4.8. The total mean freshwater flux to the Sermilik fjord is 35.5 $x10^9$ $[m^3y^{-1}]$. To obtain a summer and winter estimates for the fjord, we seasonally distribute the Merlind et al. 2010. Estimate (35.5 $x10^9$ $[m^3y^{-1}]$)

year-round using the GLOB16 normalized monthly discharge (as in Figure 4.9). In this way we extracted the value of 0.05 kg/m 2 s for winter months, and the value of 0.12 $kgm^{-2}s^{-1}$ for summer months. These values are then distributed over 4 grid-points at the head of the fjord, to mimic the Helheim glacier discharge. The four experiments performed are HRS, HRSr, HRW

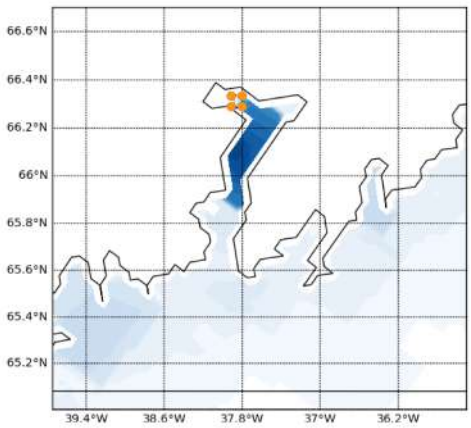

Figure 4.9: *Seasonal distribution of the runoff within the fjord. Color blue shows where the GLOB16 configuration puts the freshwater runoff, while the four orange dots show the position on which the high-RES runoff is imposed.*

and HRWr, which are respectively a summer simulation, a summer simulation with runoff, a winter simulation and a winter simulation with runoff. In Table 4.2, the details of the four experiments are shown.
Firstly, with the HRS and HRW experiments, we want to analyze the impact of summer and winter along-shore winds in forcing the intermediary circulation on seasonal time scale . Adding to those experiments an idealized runoff, in HRSr and HRWr, we want to investigate the effect of buoyancy-forcing as the additional freshwater at 0 psu and 0Â°C that is injected at 200 m. This depth has been chosen since from observations that is where the most of the glacier discharge is found in the Sermilik fjord. On the other hand, on these timescales (3 months) we do not expect to observe any modification due to deep-water renewal.

	HRS	**HRSr**	**HRW**	**HRWr**
resolution	1/49°			
bathymetry	BedMachine			
Initial condition	GLOB16; U,V: state of rest; T,S: SOL smoothed			
boundary conditions	Daily GLOB16			
Atmospheric forcing	3-hourly JRAA55-do			
period	June-September 2013 (120 days)	June-September 2013 (120 days)	December-March 2012/2013 (120 days)	December-March 2012/2013 (120 days)
runoff	NO	0.12 kg/m2s	NO	0.05 kg/m2s

Table 4.2: Summary of each experiment. Last two rows indicate the differences among the experiments' set-up.

4.4 Results

4.4.1 Summer (HRS) and winter (HRW) experiments

HRS and HRW are run with the same physical set-up in different periods. Therefore they differ by the initial conditions, the boundary conditions and have different atmospheric forcing. Both are forced by daily GLOB16 and 3-hourly JRA55-do forcing. The initial condition for both the simulation are shown in Fig. 4.10, created smoothing the temperature and salinity vertical profiles, extracted through the SOL procedure (see Section 4.2) from just outside the fjord at the first day of each simulation (Fig. 4.10).
The meridional and zonal velocities are set in a state of rest in the region within the fjord. In Fig. 4.12-4.13 the mean temperature, salinity and meridional velocity for experiments HRS and HRW are presented, for a meridional section 'along-fjord' and a zonal section 'mid-fjord' (as in Fig. 4.11). In Figure 4.12, the velocity structure exhibits almost a two-layer structure with a surface intensified current that flows towards the open ocean, and a current directed toward the glacier in the deeper layer. In winter, this current is located between 100 to 400m depth, while is found in the depth range of 50-300 min summer. Even though the vertical structure does not change significantly between summer and winter, the magnitude does: in winter the velocities are doubled in both directions.
Fjord temperature in winter exhibit the same vertical profile all over the fjord, while in summer there is a clear intrusion of warm waters from the shelf at $\sim$ 150m. From the zonal sections, we see that there is no evidence of any significant cross-fjord differences, maybe because the resolution is still not fine enough to resolve the east- west dynamics, looking both at the mean and at each hourly-output of the simulations (not shown).

Figure 4.15 shows the Hovmoller diagram of the meridional velocity, averaged along the cross-fjord section with isopycnals super-imposed. We observe a two-layer structure in both seasons. In winter the structure is more energetic and variable, having a pattern of reversing current every 3-12 days. As one might expect, in both experiments the reversals are associated with pycnocline fluctuations. The basic features of these pulses (or intermediary circulation) have been observed and here modeled correctly in both the HRS and HRW simulations.

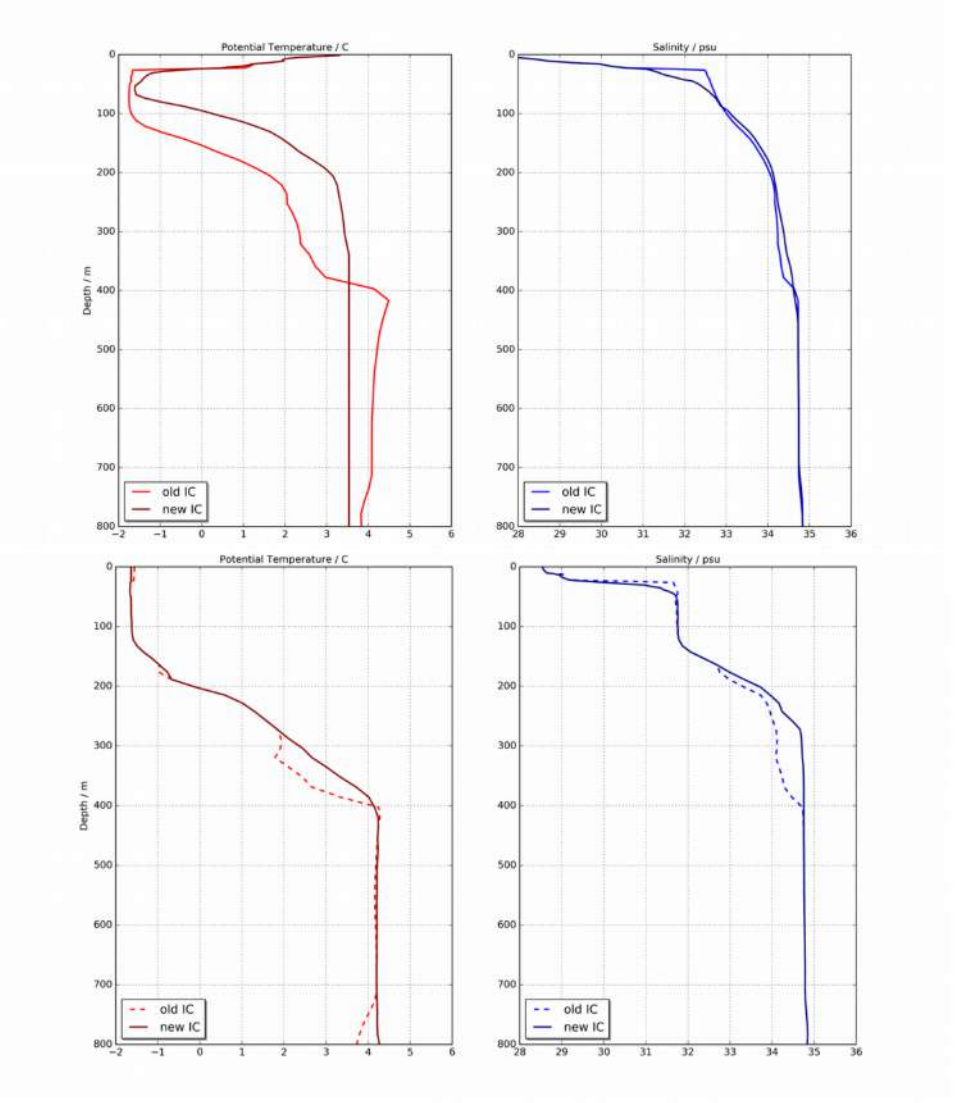

Figure 4.10: *Initial conditions for summer (upper panel) and winter (lower panel) experiments. Darker colors show the final and smoothed vertical profile extracted from the SOL procedure.*

When the PW layer thickens, associated with depressed isopycnals, a strong up-fjord flow develops above the interface and a weaker out-flow below. Velocity in each layer then reverses as the density field rebounds. Most of these reversal events are also preceded by along- shore, downwelling favor-

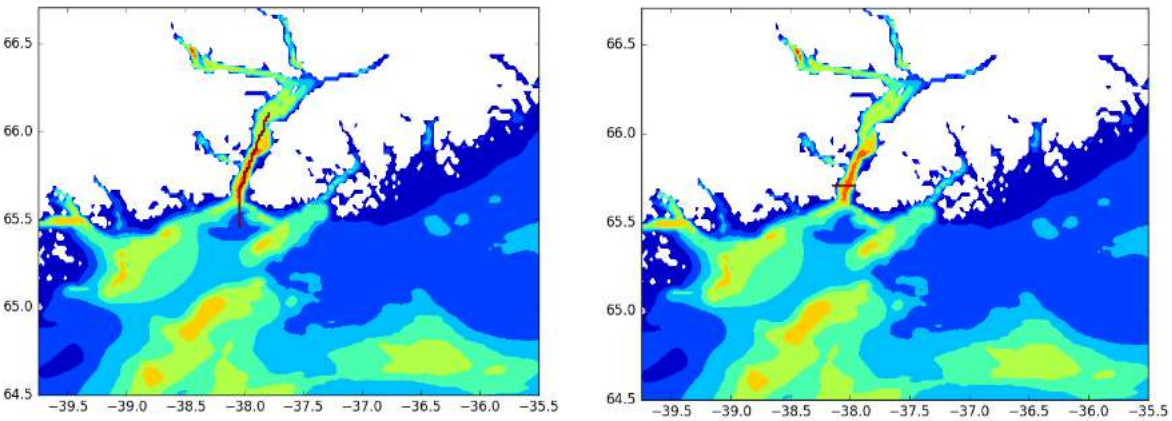

Figure 4.11: *Meridional (right panel) and zonal (left panel) 'along-fjord' section. Colors represent qualitative bathymetry.*

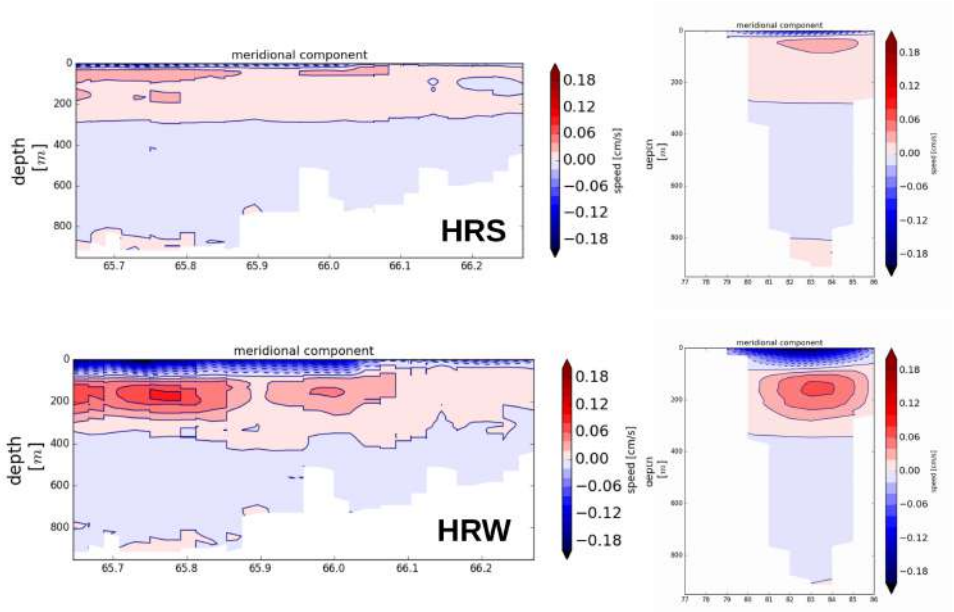

Figure 4.12: *Upper panels: mean summer meridional velocity for (left) along-fjord and (right) cross-fjord sections. Lower panels: mean winter meridional velocity for (left) along-fjord and (right) cross-fjord sections.*

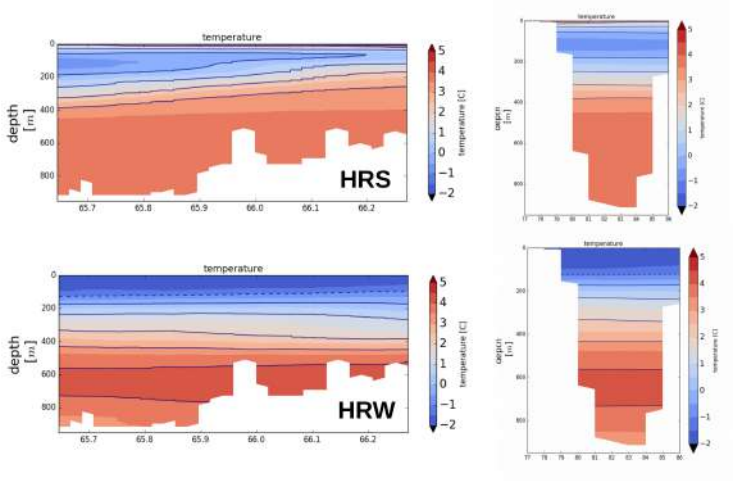

Figure 4.13: *Upper panels: mean summer temperature for (left) along-fjord and (right) cross-fjord sections. Lower panels: mean winter temperature for (left) along-fjord and (right) cross-fjord sections.*

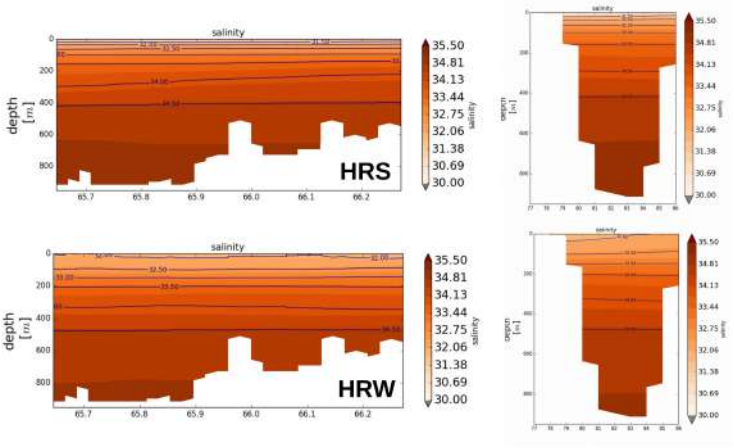

Figure 4.14: *Upper panels: mean summer salinity for (left) along-fjord and (right) cross-fjord sections. Lower panels: mean winter salinity for (left) along-fjord and (right) cross-fjord sections.*

able winds on the shelf (Fig 4.16,4.17). These winds depress isopycnals and raise the sea surface towards the coastline, resulting in the shelf/fjord set-up described above.
From Fig. 4.18 we observe the in-and out volume transport from the 'cross-shelf' section, whose difference is negligible (black line). Comparing it to Figures 4.16 and 4.17, we observe that the 'along-shore' winds are typically associated with an enhanced inflow (and outflow) in the fjord. Additionally,as observed in [52], we see that the mean toward the head of the fjord velocity (in Fig. 4.19) and thus the transport decays. Thus the atmospheric forcing on the shelf, which is strongest in the non-summer months, has a strong impact on the fjord transport.
Indeed, comparison between HRS and HRW show that the mean transport at mid-fjord and the relative standard deviation for the period double in winter. The meridional profiles in Figure 4.19 show that both the transport and the standard deviation decay more rapidly from a certain latitude, around 66.1°N. This is in accordance with [71] that, using iceberg drifters, shows that velocities are slower in the fjord, north of 66.05°N with correspondingly smaller standard deviation. That suggests that in the region, the circulation is not necessarily coupled with the intermediary circulation.

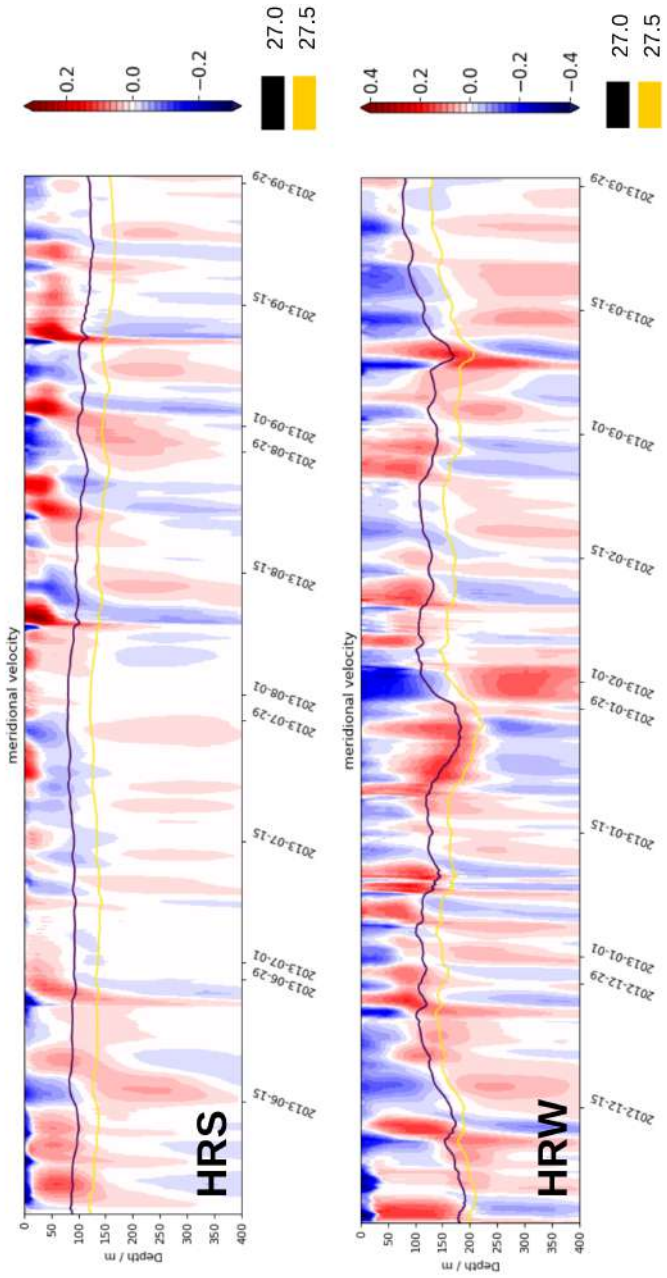

Figure 4.15: *Hovmoller diagrams for summer (upper panel) and winter (lower panel) meridional velocities, averaged on the 'cross-shelf' section. Black and yellow contour represent respectively the 1027 and 1027.5 kg/m3 isopycnals.*

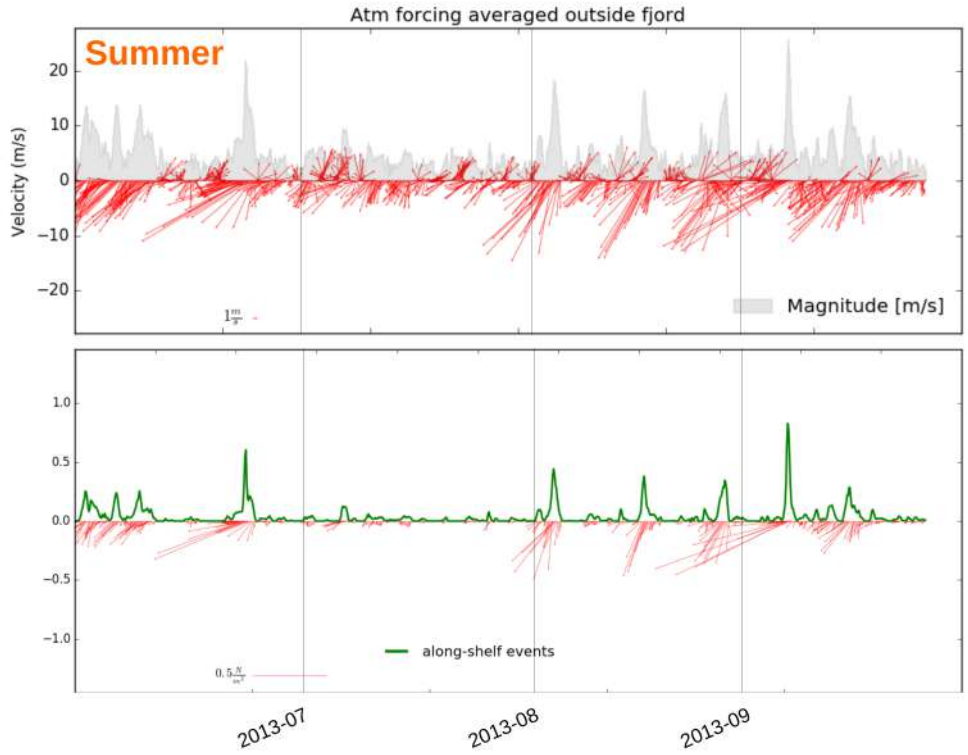

Figure 4.16: *Upper panel: summer atmospheric forcing averaged in a box of 3x3 grid-points located 45 km offshore outside of Sermilik fjord. In gray the absolute magnitude, while red arrows indicate the direction of the wind. Lower panel: summer velocity component along the principal axis (230 from north) at a point 45 km offshore outside of Sermilik fjord. Green line represent absolute magnitude, while red arrows the direction of the wind.*

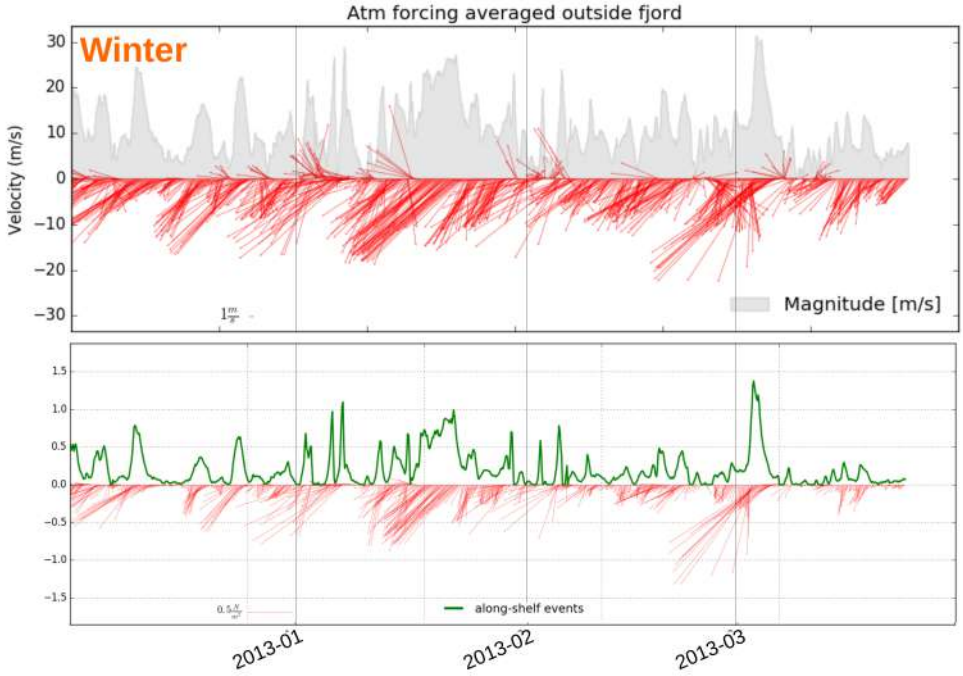

Figure 4.17: *Upper panel: winter atmospheric forcing averaged in a box of 3x3 grid-points located 45 km offshore outside of Sermilik fjord. In gray the absolute magnitude, while red arrows indicate the direction of the wind. Lower panel: winter velocity component along the principal axis (230 from north) at a point 45 km offshore outside of Sermilik fjord. Green line represent absolute magnitude, while red arrows the direction of the wind.*

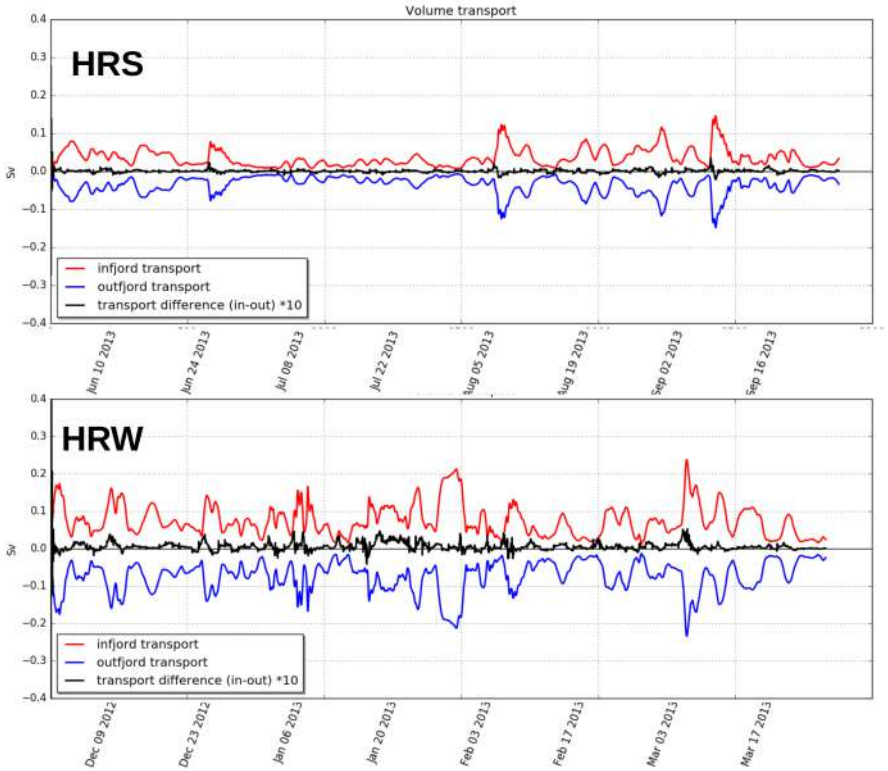

Figure 4.18: *Summer (upper panel) and winter (lower panel) in-fjord (red) and out-fjord(blue) volume transport from the cross-shelf section. Black lines indicate the transport difference between in and out multiplied by a 10 factor in order to be distinguishable from 0.*

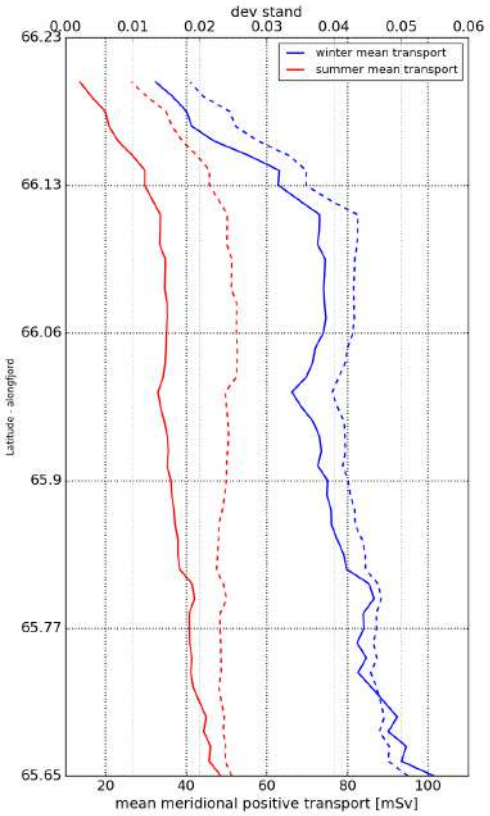

Figure 4.19: *Mean along fjord meridional positive transport for summer (bold red) and winter (bold blue). The associated standard deviation is represented by the dotted line.*

4.4.2 Summer and wint er experiments with runoff (HRSr and HRWr)

HRSr and HRWr are twin experiments of HRS and HRW with the same physical set- up and initial conditions, integrated over the same period but they include an idealized runoff input. Figure 4.20 shows the differences of mean temperature between the experiments with and without runoff for each season (HRS - HRSr and HRW - HRWr) along the meridional 'along-fjord' section. In summer, the injection of freshwater causes the warm water in the water column to move up and the cold water to move down (explaining the anomalies seen in the upper 200m and below).
In winter, the differences we observe are smaller, since the amount of freshwater injected is lower, and present a different pattern of anomalies, since the ambient column water is colder and thus the water injected finds its buoyancy at different depths (100 m and 350 m). In Figure 4.21, the horizontal distribution of temperature differences between the experiments with and without runoff is shown at differentdepths (surface, 100 m and 200 m) for both seasons. These depths have been chosen to observe the mean extension of the temperature anomalies that the runoff injected at the head of the fjord causes in three months of simulation.
In Fig. 4.22, 4.23 similar plots are shown for salinity fields. The salinity anomalies resulting from the freshwater input exhibit a similar behavior to the temperature. In winter they spread mostly on around 100m, while in summer they spread mostly in two layers at around 100 m and 350 m. In Fig. 4.24 and 4.25, the mean meridional 'along-fjord' velocity is presented for summer and winter.

In summer, the effect of the runoff is mostly evident at around 150 m, where the water injected at 200 m found its buoyancy, modifying the circulation at that depth.
Specifically the in-flow between 50 and 300 m visible in Fig. 4.24 (upper panel, red color) appears to be decoupled when the runoff is added, creating an additional layer of water that goes out-fjord. In winter the general behavior is the same but due to the stronger intermediary circulation and lower amount of runoff in that period the new structure is less evident. To better understand the circulation Fig. 4.26 and 4.27 the Hovmoller diagrams of the meridional velocity, averaged along the 'cross-fjord' section are presented.

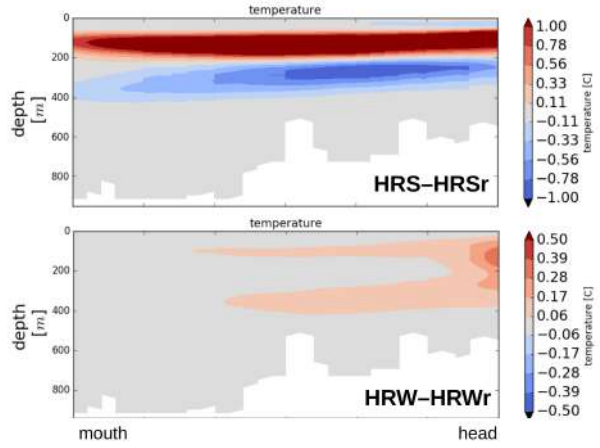

Figure 4.20: *Mean temperature differences between the summer (upper panel) and winter (lower panel) experiments with and without runoff in the meridional section 'along-fjord'. Note that the panels have different scales.*

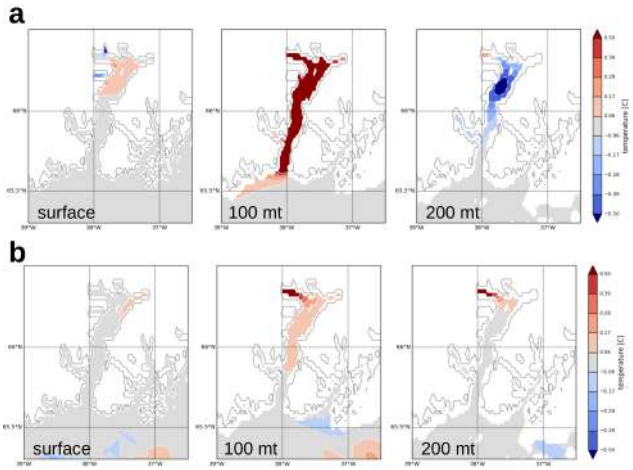

Figure 4.21: *Mean temperature differences between the summer (a) and winter (b) experiments with and without runoff for different depths: surface (right column), 100 m (central column) and 200 m (left column).*

From these plots we see how the injection of runoff changed the circulation at mid-fjord. The intermediary circulation appears affected especially in summer-time, where the out-flow at around 150 m becomes stretched and stronger in magnitude, shrinking the in-flow to lower depths. In winter, when the intermediary circulation is stronger and the runoff weaker, the general

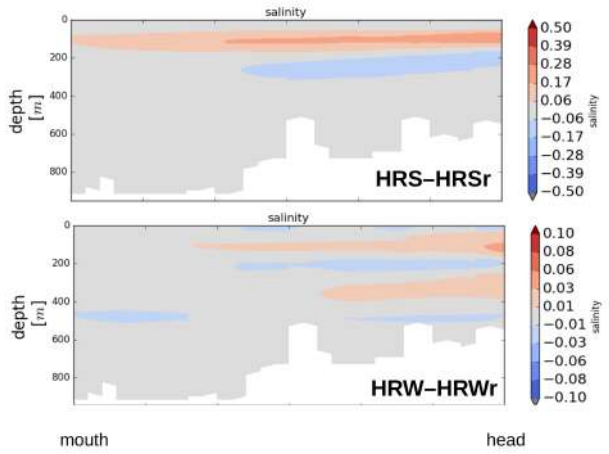

Figure 4.22: *Mean salinity differences between the summer (upper panel) and winter (lower panel) experiments with and without runoff in the meridional section 'along-fjord'. Note that the panels have different scales.*

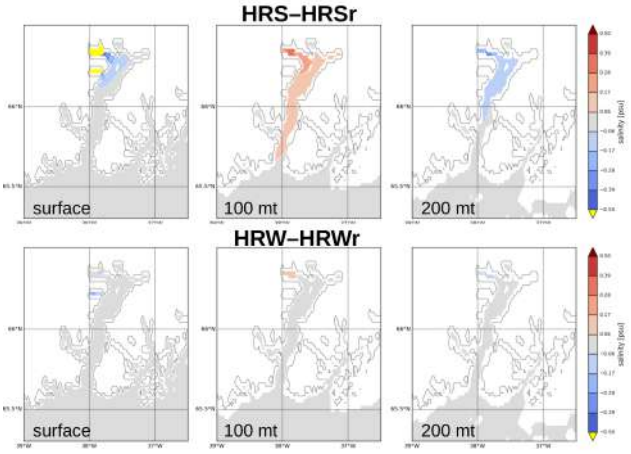

Figure 4.23: *Mean salinity differences between the summer (a) and winter (b) experiments with and without runoff for different depths: surface (right column), 100 m (central column) and 200 m (left column).*

behavior is the same, but less evident.Since it appears that the summer is the season where the properties changes the most, in Figures 4.28, 4.29, the time series of the summer temperature are shown averaged within different depth ranges during the whole simulation in two different locations (as in Fig. 4.31), at mid-fjord and at the head of the fjord, when a runoff at 0°C

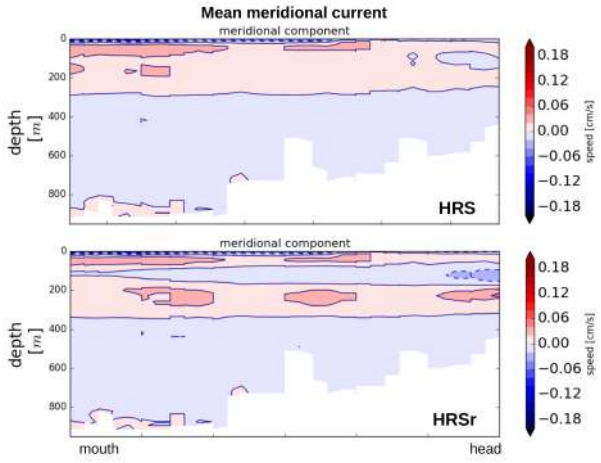

Figure 4.24: *Mean meridional velocities for experiments HRS (upper panel) and HRSr (lower panel) in the meridional section 'along-fjord'.*

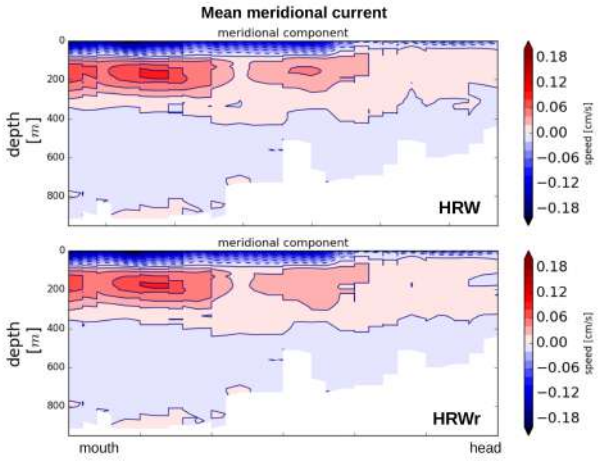

Figure 4.25: *Mean meridional velocities for experiments HRW (upper panel) and HRWr (lower panel) in the meridional section 'along-fjord'.*

and 0 psu is constantly injected. In both sections deeper waters (400 - 900 m) does not exhibit any temperature changes throughout the simulation. Mid-waters (50- 400 m) experience some minimum changes but the shallower waters (0 - 50 m) are the waters that exhibit bigger fluctuations in temperature, increasing with a visible trend due to seasonal air-sea fluxes. Figures 4.30 and 4.31 show the differences in temperature between the experiments

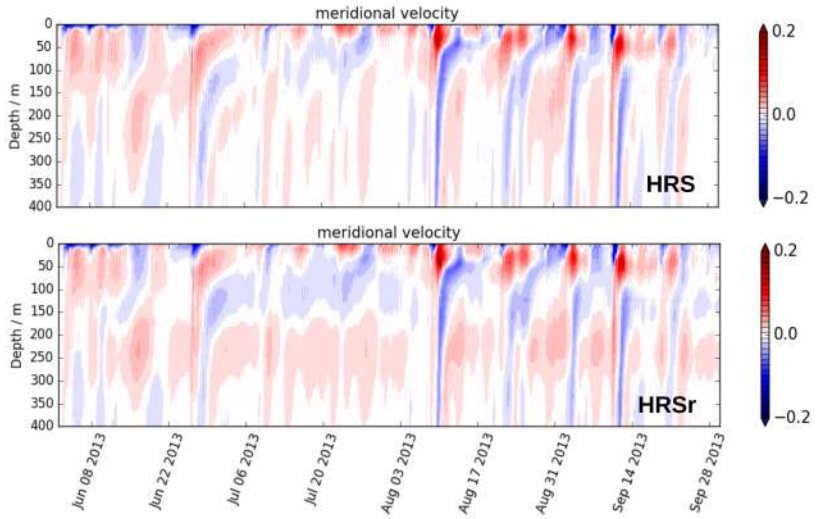

Figure 4.26: *Mean meridional velocities for experiments HRW (upper panel) and HRWr (lower panel) in the meridional section 'along-fjord'.*

with and without runoff for the same sections.
Deep water are not affected by the presence of runoff. Even though the runoff is injected at200m at a temperature considerably colder than the ambient waters at that depth (around 2°C, Fig. 4.28), we observe an increase in temperature, in particular in the depth range from 50m to 400m.
This occurs both at mid-fjord section and at the head of the fjord, but in the latter the increase in temperature in higher, around 0.5°C that the increase at mid-fjord, around 0.3°C. We here argue that the observed increase in circulation due to the presence of runoff (Fig. 4.26) it is causing more warmer water to intrude towards the head of the fjord, causing a warming of the waters in particular between 50 - 400 m.

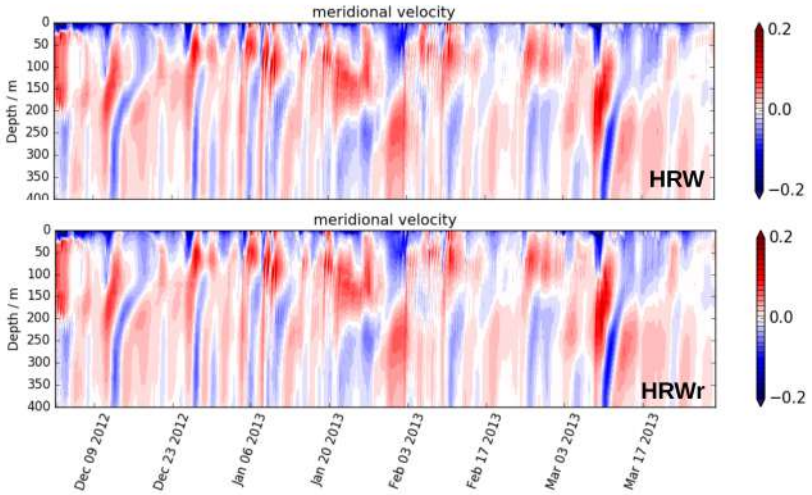

Figure 4.27: *Mean meridional velocities for experiments HRW (upper panel) and HRWr (lower panel) in the meridional section 'along-fjord'.*

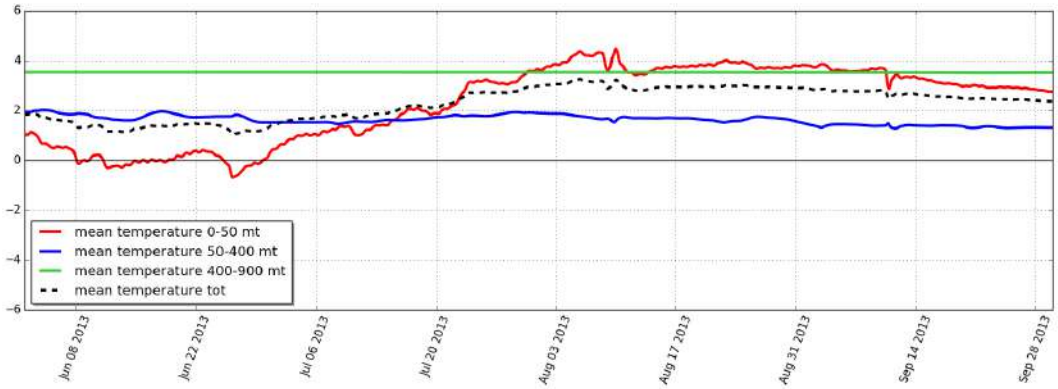

Figure 4.28: *Mid-fjord temperatures for 0-50 m (red line), 50-400 m (blue line), 400-900 m (green line) and the total water column (dotted black line).*

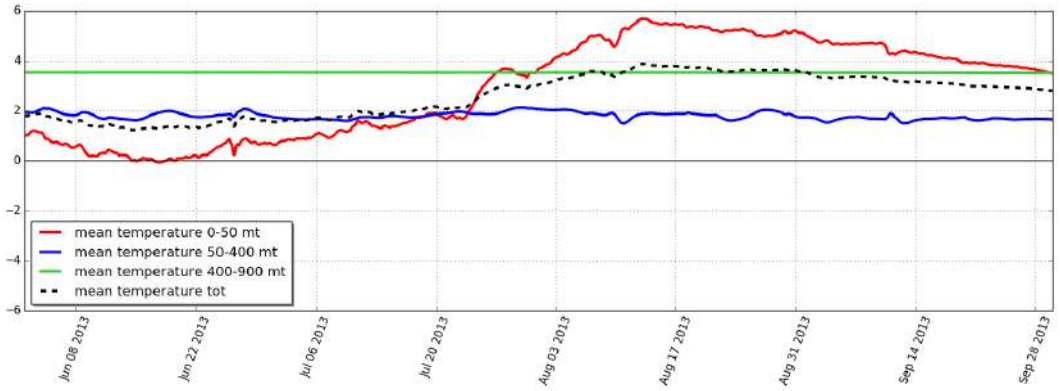

Figure 4.29: *Fjord head temperatures for 0-50 m (red line), 50-400 m (blue line), 400-900 m (green line) and the total water column (dotted black line).*

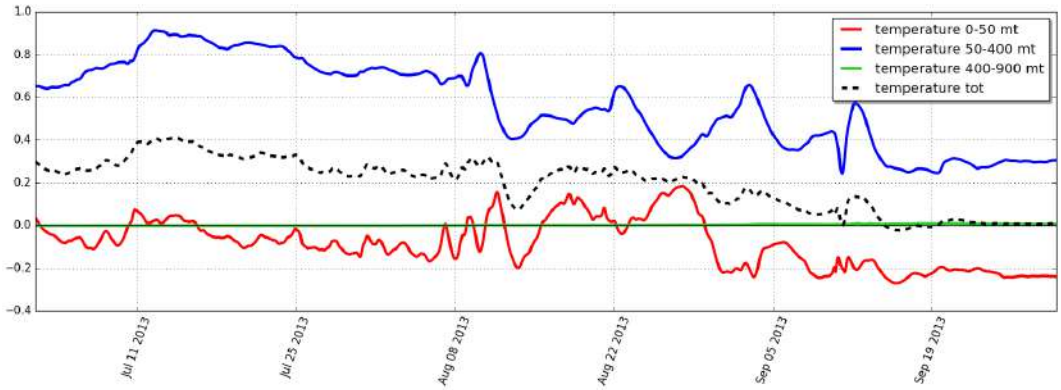

Figure 4.30: *Mid-fjord temperature differences (HRS-HRSr) for 0-50 m (red line), 50-400 m (blue line), 400-900 m (green line) and the total water column (dotted black line).*

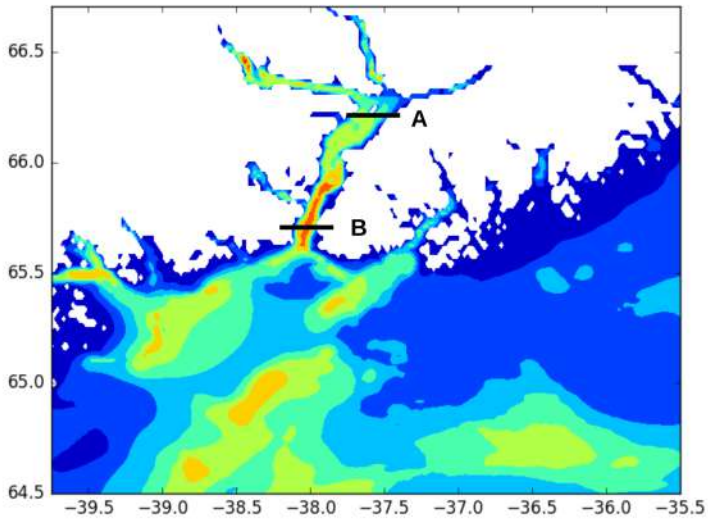

Figure 4.31: *Section located at the head of the fjord (section 'A') and the one located at mid-fjord (section 'B'). Colors are qualitatively bathymetry.*

4.4.3 Summer sensitivity experiments

We investigated in Section 4.4.1 the fjord dynamics in summer without the presence of runoff. We observed a two layer circulation in the fjord, and multiple reversals of circulation, found to frequency peaking between 6-12 days. They are associated with depressed pycnoclines and bursts of along-shore winds, which are computed at a location 45 km away from the fjord. This is what is called intermediary circulation. Having demonstrated the ability of the model to represent a buoyancy circulation in Section 4.4.2, we now perform different sets of experiments changing the properties of the injected runoff during the summer seasons.
It has been observed that the intermediary circulation is less strong in summer from observations [52], and we demonstrated this in Section 4.4.1. This allows the buoyancy circulation to be clearly detected. Secondly, the discharge in summer has been observed to be higher, allowing us to have a larger range of values to be chosen for the sensitivity experiments.
For the first guess experiment, we assumed a runoff with salinity of 33 psu, temperature of 2°C at a depth of 200 meters, coming solely from Helheim glacier. The magnitude of this runoff is set to be equal to 0.15 kg/m2s. This is a realistic representation of the glacier runoff properties, derived from observations. [48].
The following experiments have been integrated for the summer season for 120 days, starting in June 2013.
The scientific questions we want to answer are the following: (I) Which are the runoff variables that affect more the circulation and the properties of the fjord? (II) To which extent are the properties at the head of the fjord affected by runoff? (III) Which are the implications for future modeling studies?
The sensitivity experiments can be summarized in 'sets', depending on which variable is tuned. Therefore we will have the following sets:

- set T: in this set of experiments runoff temperature takes the values of 1 °C, 1.5 °C and 2 °C; since the waters coming from sub-glacial discharge and submarine melting do not usually exhibit great ranges of temperatures, being close to the freezing point, we argue that we explore a realistic range of summer temperature runoff.

- set S: in this set, salinity runoff is set to 32.5 psu, 33 psu, 33.5 psu and 25 psu;
- set M: here the magnitude of runoff is increased every 0.05 kg/m^2s from 0.05 to 0.20 kg/m^2s (0.05, 0.10, 0.15, 0.20 kg/m^2s);
- set D: the depth where the runoff is imposed is set every 100 m from the surface to 300 m (0, 100, 200, 300 m);
- set L: in these experiments the number and location of the grid points over which the runoff is spread is changed. The first experiment has the runoff spread over four points near Helheim Glacier, the second over nine grid points still near Helheim glacier and the last one consists in twelve grid points spread over the whole head of the fjord, mimicking the export of water from the three glaciere that are present in reality (Helheim, Fenrir and Midgard glaciers).

In Table 4.3 the specific of each experiment are presented.

EXP	**temperature** $[C]$	**salinity** $[psu]$	**magnitude** $[kg/m^2s]$	**depth** $[m]$	**location**
T1	**1**	33	0.15	200	H
T1_5	**1.5**	33	0.15	200	H
T2	**2**	33	0.15	200	H
T2_5	**2.5**	33	0.15	200	H
S1	2	**32.5**	0.15	200	H
S2	2	**33.5**	0.15	200	H
S3	2	**25**	0.15	200	H
M05	2	33	**0.05**	200	H
M10	2	33	**0.10**	200	H
M20	2	33	**0.20**	200	H
D000	2	33	0.15	**0**	H
D100	2	33	0.15	**100**	H
D300	2	33	0.15	**300**	H
L1	2	33	0.15	200	**bigger H**
L2	2	33	0.15	200	**H,L,M**
SMD	2	**25**	**0.20**	**300**	H

Table 4.3: The sensitivity experiments.

Set T - changing temperature

In Fig 4.32 and 4.33 the along-fjord anomalies averaged over the whole period of simulation from set T are shown. These plots are a good indicator of the differences that an injection of runoff with different temperature causes on the overall fjord. The temperature of the injected runoff in this window just slightly changes the overall temperature (with anomalies not greater than $\sim 0.05°C$, Fig. 4.32), salinity with anomalies not greater than $\sim$ 001 psu, Fig. 4.33) and circulation (with anomalies not greater than $\sim 0.02m/s$, Fig. 4.34) of the fjord. This implies that, to affect the properties within the whole fjord, the change in runoff temperature must be greater than the one considered here (at least $\Delta T > 1.5°$C). Additionally, from the time series (Fig. 4.35) it is clear that temperature and salinity anomalies due to the intrusion shift vertically in time accordingly to the change of the column water properties, driven by the shelf-forced circulation.
The differences between each experiment are so small that temperature within this range is not a property of runoff that affects significantly the fjord.

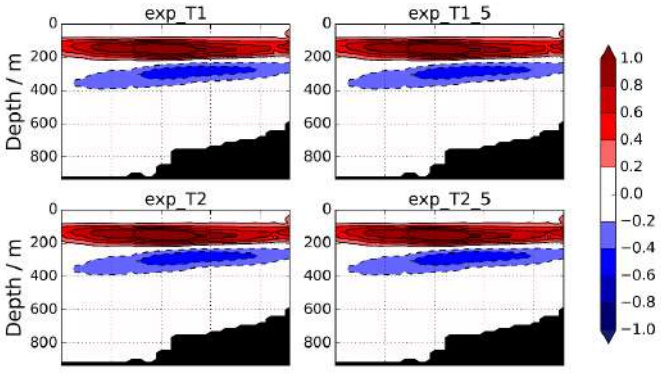

Figure 4.32: *Mean temperature anomalies between the control experiment (no runoff) and the labeled experiments (from upper left to lower right: T1, T1_5, T2, T2_5) in the meridional section 'along-fjord'. The colorbar is in Celsius degrees.*

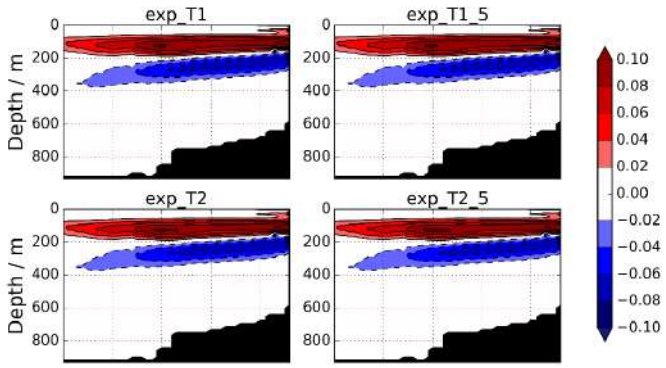

Figure 4.33: *Mean salinity anomalies between the control experiment (no runoff) and the labeled experiments (from upper left to lower right: T1, T1_5, T2, T2_5) in the meridional section 'along-fjord'. The colorbar is in psu.*

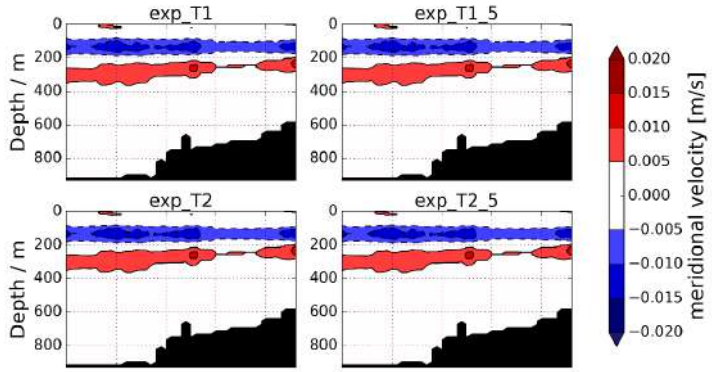

Figure 4.34: *Mean meridional velocity anomalies between the control experiment (no runoff) and the labeled experiments (from upper left to lower right: T1, T1_5, T2, T2_5) in the meridional section 'along-fjord'.*

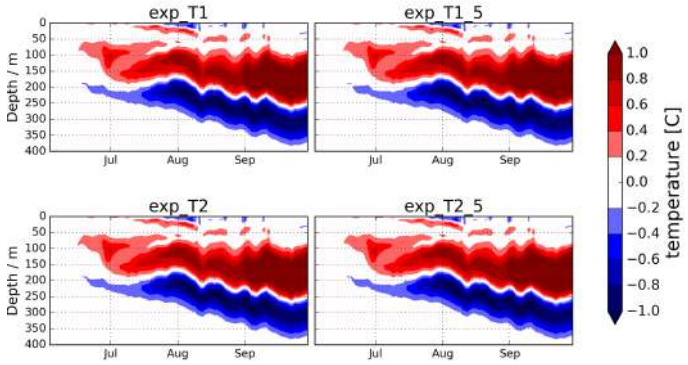

Figure 4.35: *Fjord head temperature anomalies between the control experiment (no runoff) and the labeled experiments (from upper left to lower right: T1, T1_5, T2, T2_5) in the zonal section at the head of the fjord (section 'A' in Fig. 4.31). The colorbar is in Celsius degrees.*

Set S - changing salinity

As for Set T, we see that a range of salinity compatible with the one observed (32.5 psu, 33 psu and 33.5 psu) does not change significantly the overall temperature (with anomalies not greater than $\sim 0.05°C$), salinity (with anomalies not greater than $\sim$ 001 psu) and circulation (with anomalies not greater than $\sim 0.02m/s$) of the fjord.
This implies that, in order to affect the properties within the whole fjord, the change in runoff salinity must be greater than the one considered in experiments S1, T2 and S2 (at least $\Delta S > 1$ psu). For this reason an additional low salinity run (hereafter S3) has been performed, and only the differences between either S1 or S2 and S3 are significant and here analyzed. In particular S3 experiment has been set with a runoff of 25 psu, a salinity largely distant from the observations available for the fjord, but still realistic in a framework of great discharge of waters. The S3 experiment represents numerically what happens when water with a salinity (and therefore density) inserted in the fjord water-column structure.
In Fig. 4.36 and Fig. 4.37 mean temperature and salinity anomalies are shown along the fjord. S3 causes the anomalies to be smaller in magnitude with respect to S1/S2.
Circulation anomalies are shown in Fig. 4.38.
We focus on the section at the head of the fjord (section 'A' in Fig. 4.31). Fig. 4.39, Fig. 4.40 and Fig. 4.41 show the time evolution of temperature, salinity and meridional velocity anomalies. We observe that in general the anomalies appear to be compressed and shifted to the upper column. Specifically, regarding temperature, positive anomalies are concentrated in a smaller region, causing bigger

positive anomalies than the ones found in run S1/S2. This means that simply the different salinity causes the 2° C waters to be compressed in a smaller region, hence the difference in temperature.
The overall change in circulation (Fig. 4.41) appears to be slightly stretched and stronger in S1/S2 (maximum increase/decrease of $\sim \pm 2$ cm/s) with respect to the one in S3 (maximum increase/decrease of $\sim \pm 1.5$ cm/s), even though the structure is overall the same.
These changes does not lead to a two-cells circulation, since the magnitude of the anomalies (that have a maximum of ~ 0.02 m/s) is too small to create an additional layer of waters going out of the fjord. With this set of experiments is clear, as for set T, that the changes induced by different salinities are small with respect to changes inducted by the addition of runoff alone.

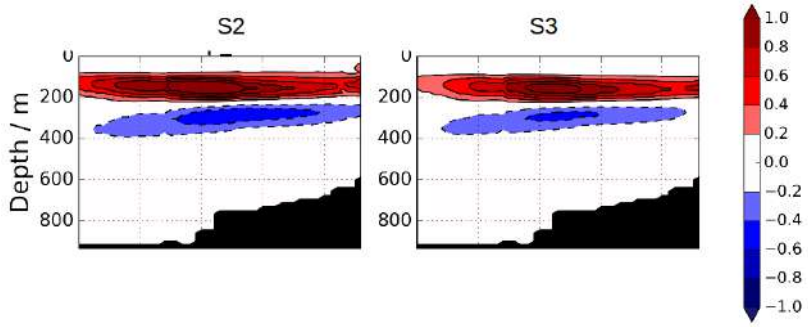

Figure 4.36: *Mean temperature anomalies between the control experiment (no runoff) and the labeled experiments (from left to right: S2, S3) in the meridional section 'along-fjord'. The colorbar is in Celsius degrees.*

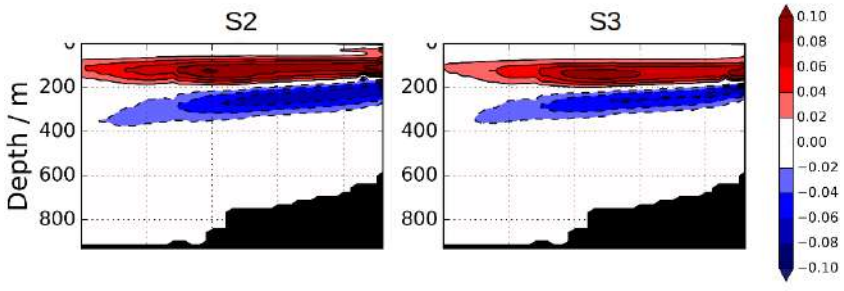

Figure 4.37: *Mean salinity anomalies between the control experiment (no runoff) and the labeled experiments (from left to right: S2, S3) in the meridional section 'along-fjord'. The colorbar is in psu.*

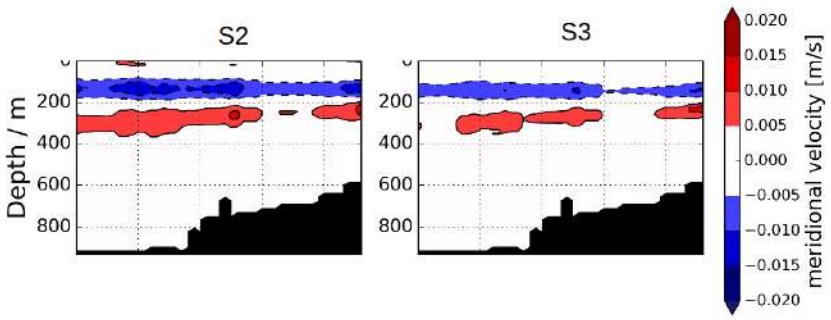

Figure 4.38: *Mean meridional velocity anomalies between the control experiment (no runoff) and the labeled experiments (from left to right: S2, S3) in the meridional section 'along-fjord'.*

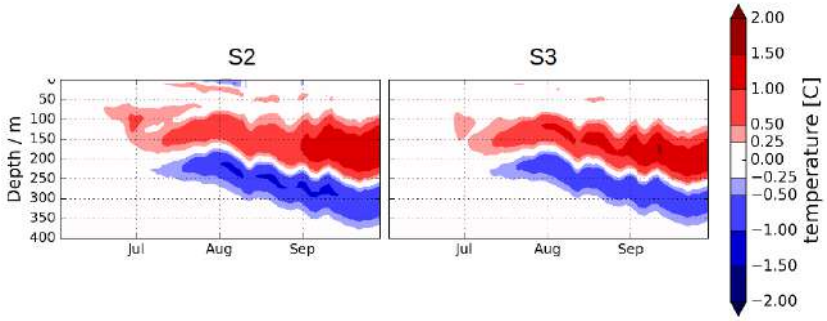

Figure 4.39: *Mean meridional temperature anomalies between the control experiment (no runoff) and the labeled experiments (from left to right: S2, S3) in the meridional section at the 'head' of the fjord.*

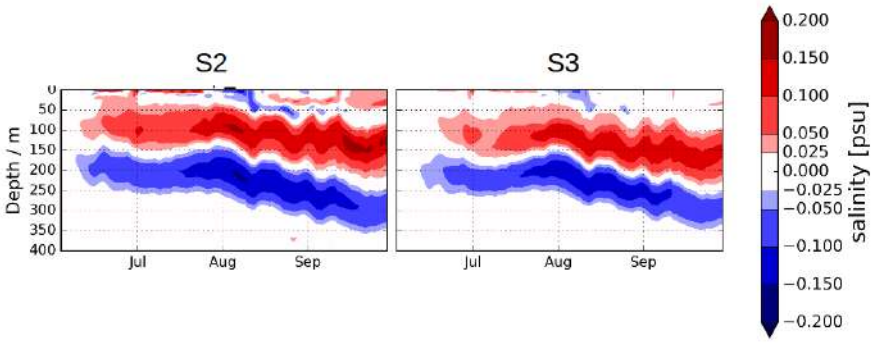

Figure 4.40: *Mean meridional salinity anomalies between the control experiment (no runoff) and the labeled experiments (from left to right: S2, S3) in the meridional section at the 'head' of the fjord.*

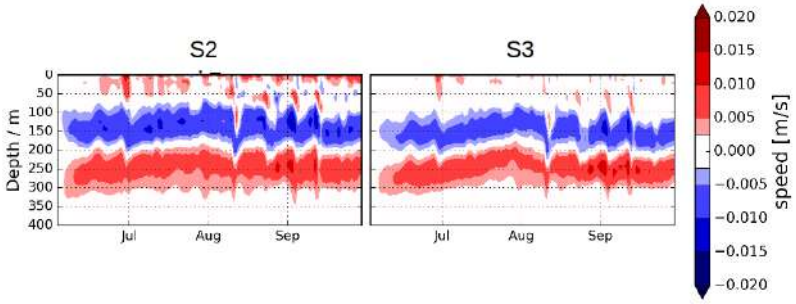

Figure 4.41: *Mean meridional velocity anomalies between the control experiment (no runoff) and the labeled experiments (from left to right: S2, S3) in the meridional section at the 'head' of the fjord.*

Set M - changing magnitude

The range of magnitude that has been taken into account is realistic as it represents a big enough window of discharge that can take place in summer in Sermilik fjord. Changing the magnitude of the injected runoff causes changes to the overall temperature, salinity and circulation of the fjord. Specifically, similarly to set T and S, salinity and temperature exhibit the same pattern of anomalies, but the changes appear to be proportional to the amount of runoff injected (Fig. 4.42, Fig. 4.43, Fig. 4.44).
At the head of the fjord, the comparison between the different mean temperature in the upper 400 mt are shown in Fig. 4.45. The temperature here increases as we enhance the magnitude of the runoff (that is always set at 2 °C).

Additionally, we show in Fig. 4.46 the sensitivity of the inward heat transport as a function of the magnitude of the injected runoff, in order to address to which extent the head of the fjord is affected. The plot shows clearly that it is present a strong linear correlation between the two variables.
These findings suggest that the induced circulation brings in the fjord warm waters from outside the shelf. The control experiment shows the inward heat transport is negative (Fig. 4.46), meaning that the mean properties of the waters are below the reference temperature, chosen as 0 °C.
Experiment M20 show the highest mean inward heat transport, that has a value of $\sim$ 17 MW.
In order to understand if this quantity is negligible, we can use classic calorimetry equations to obtain an approximation of the amount of ice mass melted with this total heat.
For a period of 4 months (the temporal length of simulation), this roughly translates to $17x10^{10}$ J for the whole period.
Assuming a mean temperature of the ice at the boundary to be $\sim$ -2°C, and a final temperature of ice to 0°C, the total mass of ice that would be melted with $17x10^{10}$ J is $m \sim 5x10^5$ kg.

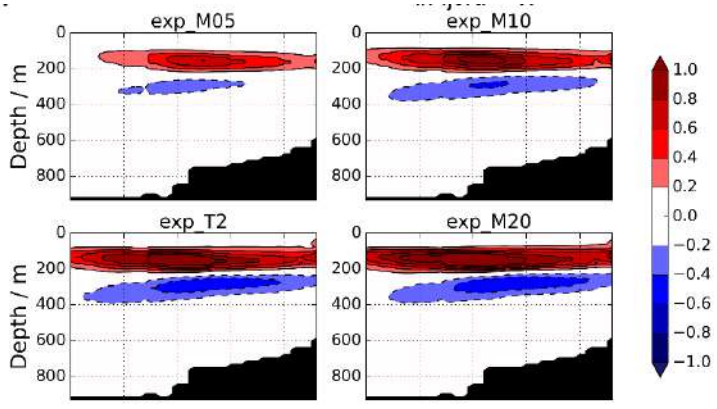

Figure 4.42: *Mean temperature anomalies between the control experiment (no runoff) and the labeled experiments (from upper left to lower right: M05, M10, M15/T2, M20) in the meridional section 'along-fjord'. The colorbar is in Celsius degrees.*

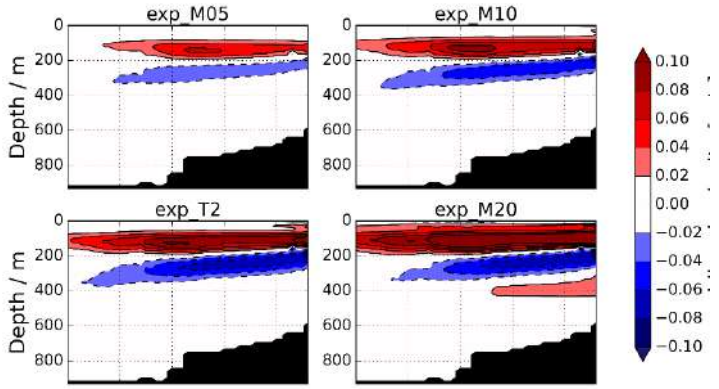

Figure 4.43: *Mean salinity anomalies between the control experiment (no runoff) and the labeled experiments (from upper left to lower right: M05, M10, M15/T2, M20) in the meridional section 'along-fjord'. The colorbar is in psu.*

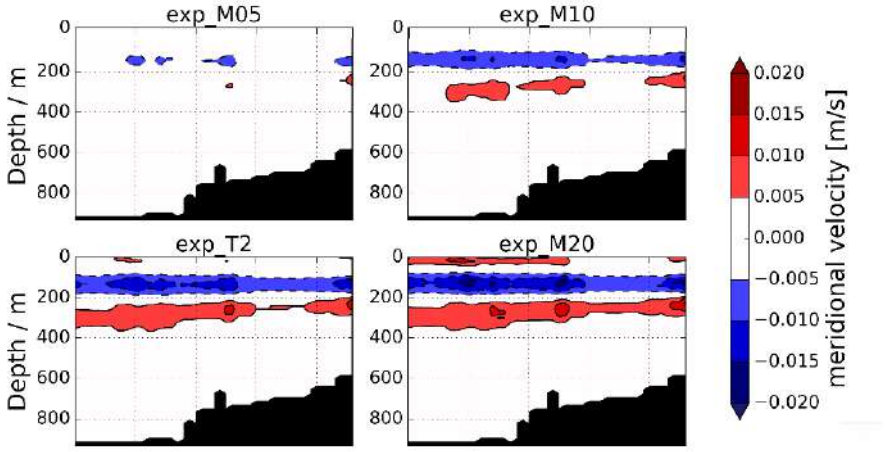

Figure 4.44: *Mean meridional velocity anomalies between the control experiment (no runoff) and the labeled experiments (from upper left to lower right: M05, M10, M15/T2, M20) in the meridional section 'along-fjord'.*

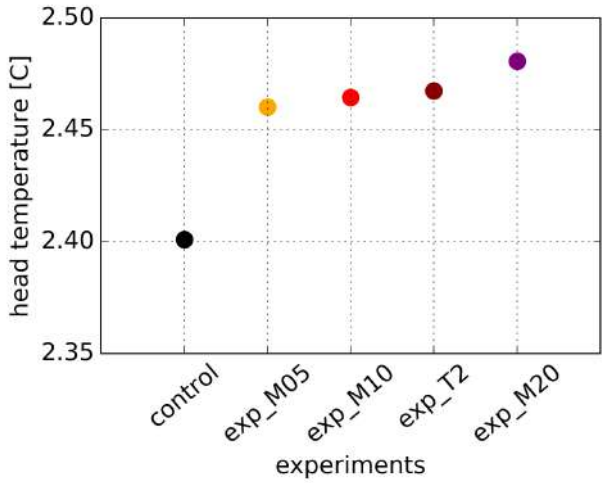

Figure 4.45: *Mean temperature comparison between the control experiment (no runoff) and the labeled experiments in the zonal section at the 'head' of the fjord.*

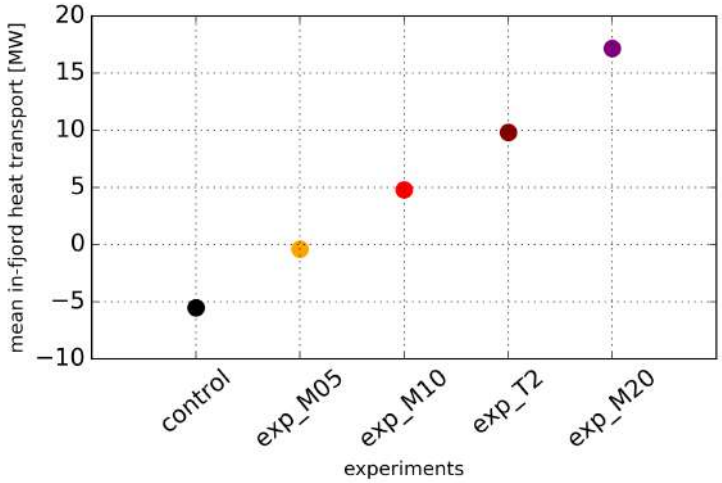

Figure 4.46: *Mean in-ward heat transport comparison between the control experiment (no runoff) and the labeled experiments in the zonal section at the 'head' of the fjord.*

Set D - changing depth

With this set of experiments we aim to investigate how the depth of intrusion influences the circulation and properties within the fjord.
This issue is critical, since it has been observed that, depending on its magnitude, the discharge can give rise to a single overturning cell (when it reaches the surface) or multiple cells characterized by intrusions of glacially modified water at mid-depths, typically between the AW and PW layer [3] .
From Fig. 4.47 and 4.48 we see that temperature and salinity anomalies are progressively increasing their extent as we apply discharge deeper and deeper , even though the magnitude injected is still the same. These changes in position and extent of anomalies are easily explained by the stratification of the fjord column water, characterized by a strongly stratified (owing to AW and PW) ambient water column.
Similarly, from Fig. 4.49 we see that the buoyancy-induced circulation progressively increases as we deepen depth. This does not translates necessary to an increase of heat transport, since the position of the induced circulation changes in the different experiments.
We show therefore in Fig. 4.50 the inward heat transport as a function of the depth. The plot shows clearly that the heat transport depends on the depth injection, and has a maximum when it is injected at 100 mt. This is easily explained by the fact that the enhanced out-fjord circulation in exp D100 occurs at the same depth as the minimum temperature of the water-column, pushing cold water towards the shelf.

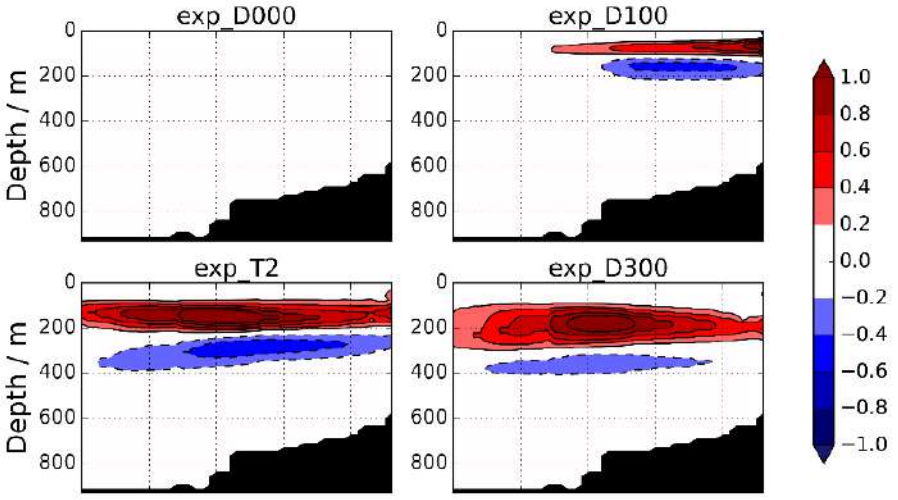

Figure 4.47: *Mean temperature anomalies between the control experiment (no runoff) and the labeled experiments (from upper left to lower right: D0, D100, D200/T2, D300) in the meridional section 'along-fjord'. The colorbar is in Celsius degrees.*

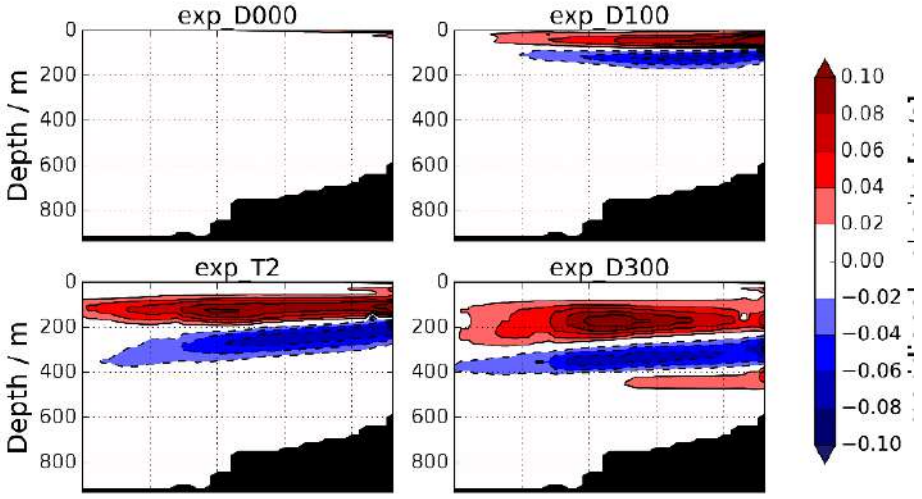

Figure 4.48: *Mean salinity anomalies between the control experiment (no runoff) and the labeled experiments (from upper left to lower right: D0, D100, D200/T2, D300) in the meridional section 'along-fjord'. The colorbar is in psu.*

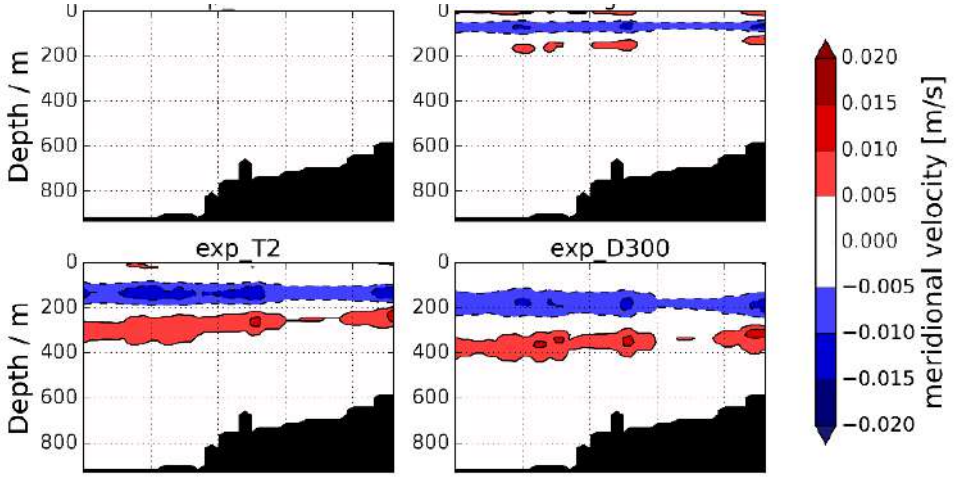

Figure 4.49: *Mean meridional velocity anomalies between the control experiment (no runoff) and the labeled experiments (from upper left to lower right: D0, D100, D200/T2, D300) in the meridional section 'along-fjord'.*

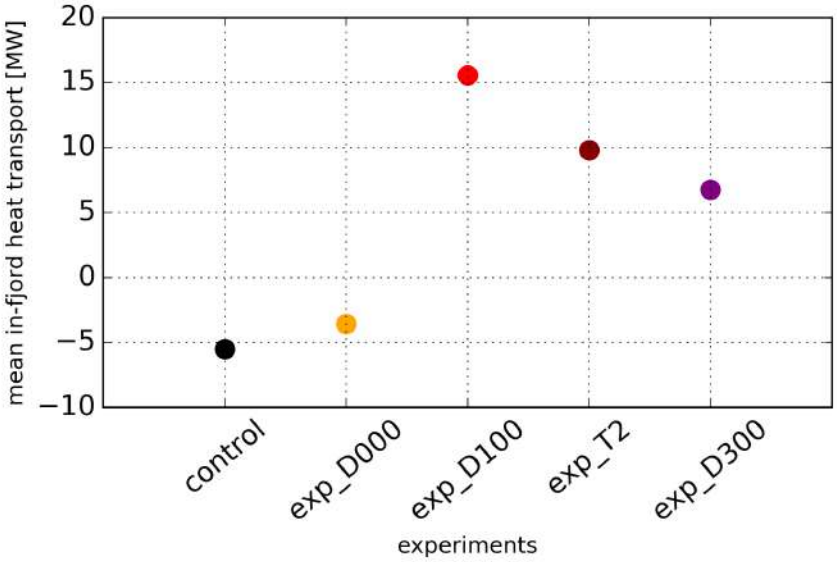

Figure 4.50: *Mean in-ward heat transport comparison between the control experiment (no runoff) and the labeled experiments in the zonal section at the 'head' of the fjord.*

Set L - changing horizontal distribution

The goal of this set of experiments is to evaluate if the results are affected by the horizontal distribution of the runoff. As mentioned before, T2 experiment employs a runoff spread over 4 grid points at the ice-ocean boundary of Heilhem Glacier. L1 employs a runoff spread over nine grid points centered in the same location as T2, and L2 consists of twelve grid points spread over the whole head of the fjord, mimicking the export of water from the three glacier that are present in reality (Helheim, Fenrir and Midgard glaciers).
The comparison between T2 and L1 shows that the overall temperature, salinity and circulation of the fjord does not change at all. This demonstrates that the above and next results are not affected by position and number of points over the runoff is spread at the Helheim glacier.
On the other hand, some minor discrepancies are seen comparing L1 and L2. Specifically, the change of location of the injected runoff changes the overall temperature by a maximum of $\sim 0.02°C$, salinity by $\sim$ 002 psu and circulation by ~ 0.5 cm/s.
We can conclude that for the overall fjord, setting the runoff at different sea-ice boundaries with the same properties induce changes that are negligible.

SMD experiment

This single experiment has been performed in order to understand the fjord response to properties that are closer to a input from a plume.
Specifically we chose salinity to be 25 psu, in order to be closer to a salinity that is the result of the mixing between melted freshwater and the fjord ambient waters. We chose depth to be 300m and magnitude 0.20 kg/m^2s, close to observations and consistent to an enhanced discharge.
We evaluated this experiment against the control (no runoff), the first-guess experiment (T2), the 300 mt depth (D300) one and the experiment with the higher discharge(0.20 kg/m^2s, M20).
From Fig. 4.51 and 4.52 we see that temperature and salinity are showing the same pattern of anomalies for all the experiment considered. Similarly, from Fig. 4.53 we see that the buoyancy-induced circulation anomaly exhibit the same pattern, even though the anomalies appear to be stretched in the SMD experiment. This does not translates necessary to an increase of heat transport, as seen before, but it increases the mean temperature at the head of the fjord (Fig.4.54).
We show in Fig. 4.55 the sensitivity of the inward heat transport as a function of the different experiments. The plot shows that the the fjord has a non-linear dynamic response to the parameters we changed. This result underlines the complexity of the system and the interplay within the parameters that have been chosen play a big role in determining the response of it.

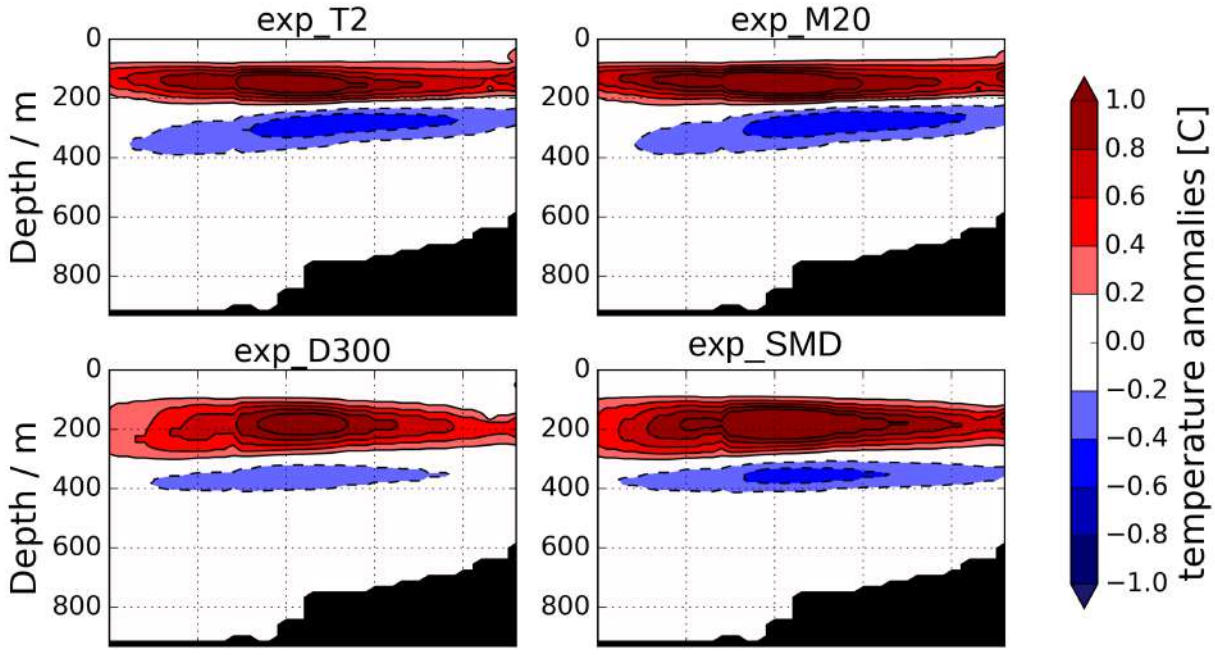

Figure 4.51: *Mean temperature anomalies between the control experiment (no runoff) and the labeled experiments (from upper left to lower right: D0, D100, D200/T2, D300) in the meridional section 'along-fjord'. The colorbar is in Celsius degrees.*

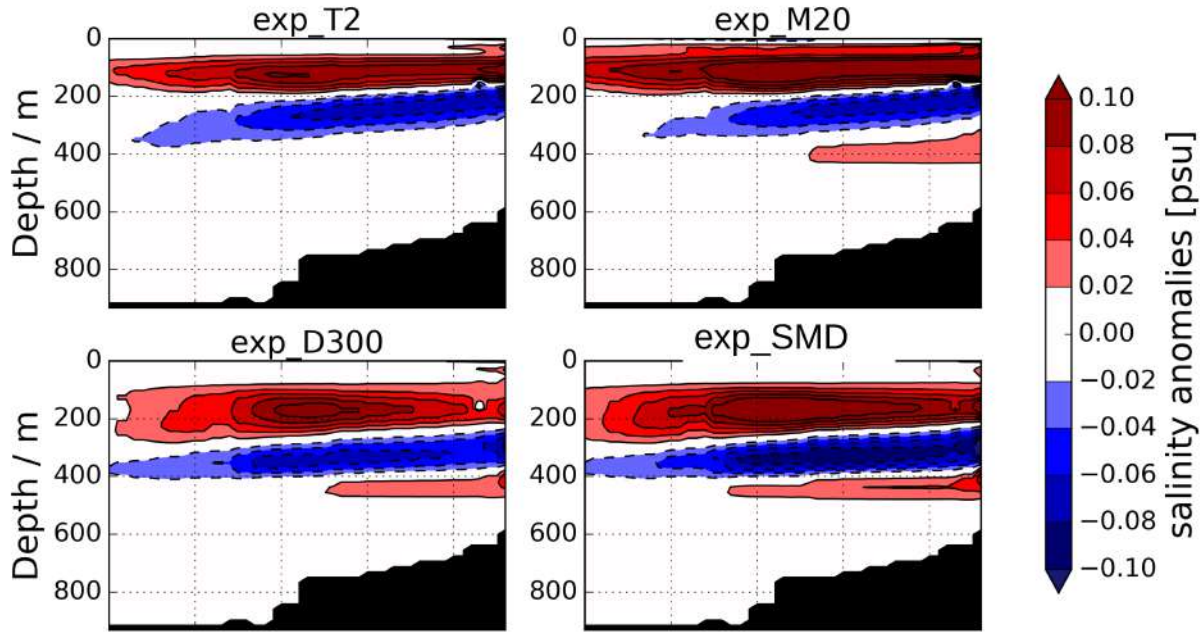

Figure 4.52: *Mean salinity anomalies between the control experiment (no runoff) and the labeled experiments (from upper left to lower right: D0, D100, D200/T2, D300) in the meridional section 'along-fjord'. The colorbar is in psu.*

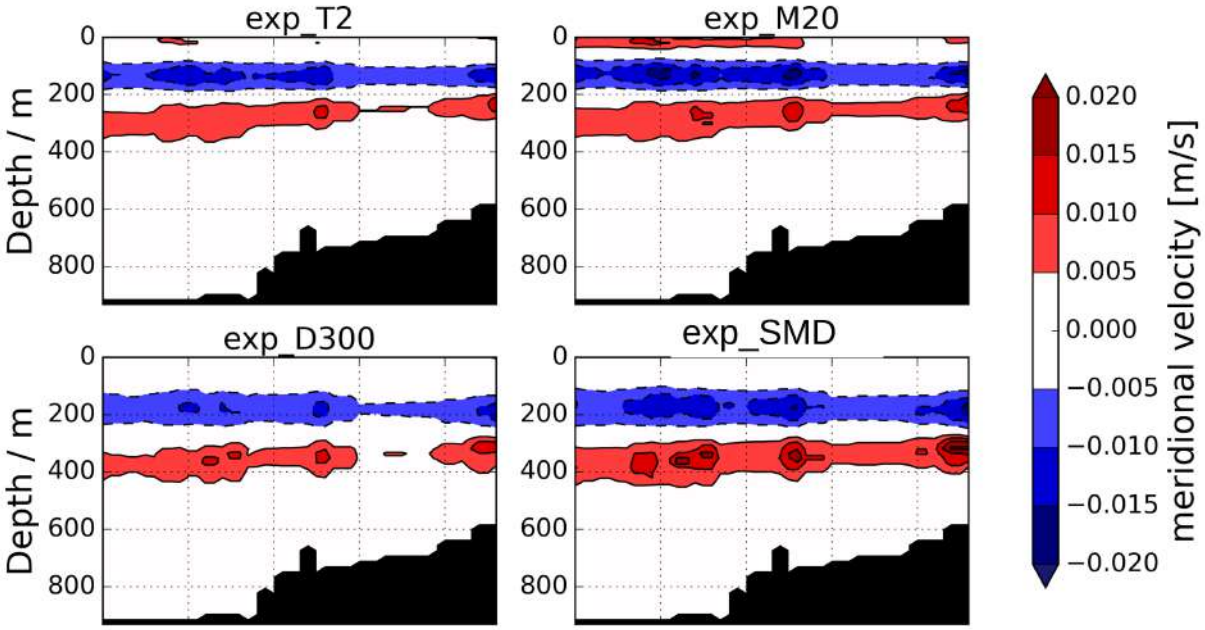

Figure 4.53: *Mean meridional velocity anomalies between the control experiment (no runoff) and the labeled experiments (from upper left to lower right: D0, D100, D200/T2, D300) in the meridional section 'along-fjord'.*

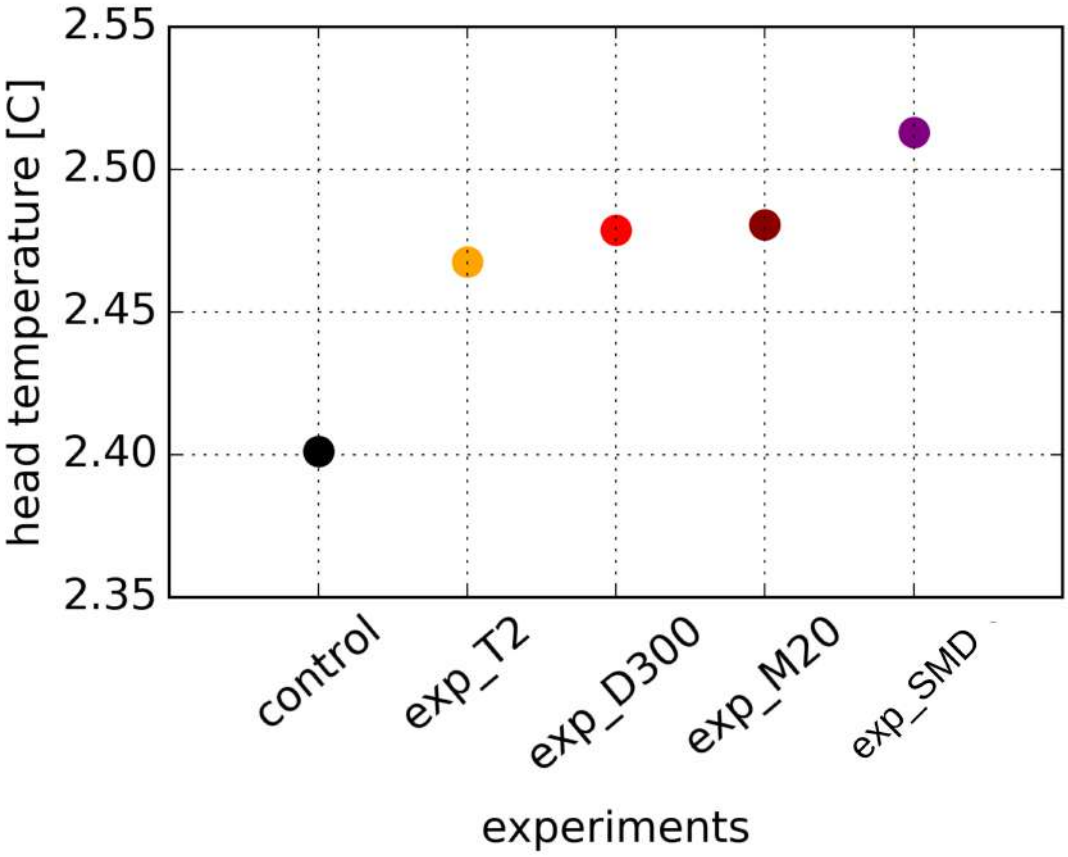

Figure 4.54: *Mean temperature comparison between the control experiment (no runoff) and the labeled experiments in the zonal section at the 'head' of the fjord.*

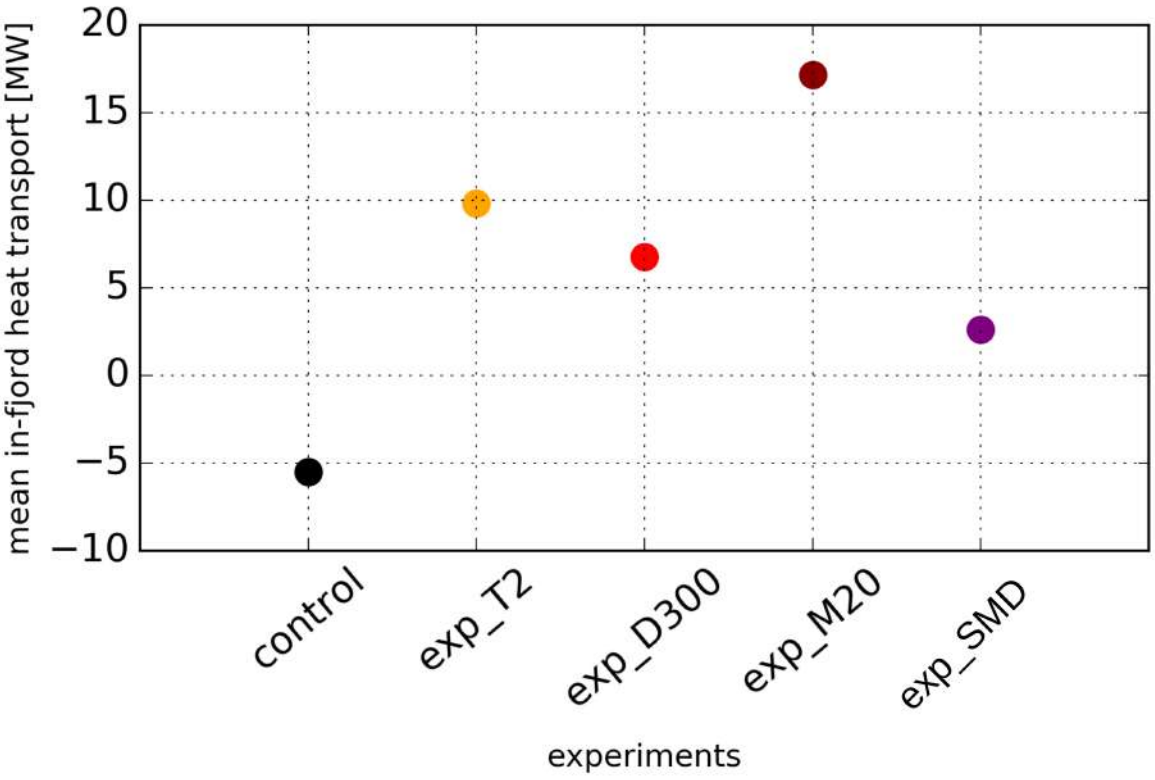

Figure 4.55: *Mean in-ward heat transport comparison between the control experiment (no runoff) and the labeled experiments in the zonal section at the 'head' of the fjord.*

4.5 Summary

In this Chapter, we presented the 1/48° resolution regional ocean configuration embedded in the global eddying ocean over the Sermilik fjord region. This configuration, implemented via SURF framework, is used to simulate the shelf-forced fjord seasonal dynamics, in summer and in winter seasons.
We investigated the differences and similarities of the fjord dynamics in summer and winter. In both seasons, we observed a two layer circulation in the fjord, and multiple reversals of circulation. The reversals are found to be more energetic and frequent in winter with respect to summer, with a frequency peaking between 3-8 days. They are associated with depressed pycnoclines and bursts of along-shore winds, computed at a location 45 km away from the fjord (as in [72]). This is what is called intermediary circulation.
In our model simulations, the mid-fjord winter volume transport is doubled compared to summer. This is associated to the fact that the shelf-driven circulation is more energetic during winter, and means that an anomalous winter on the SE Greenland shelf could have potentially more impact of an anomalous summer, on the properties of the fjord. To analyze the combined effect of both the shelf-forced circulation and a buoyancy-driven circulation from an idealized runoff, we injected water at depth at the head of the fjord, to mimic the Helheim seasonal freshwater discharge.
For this purpose, the SURF platform have been improved by adding the option to have an idealized runoff as boundary condition. This was a necessary step in order to study the glacier-terminating fjords circulation, in particular in a summer regime. The model results show indeed that in summer the circulation is primarily glacially-driven, due to weaker shelf-forced flows and bigger export of the freshwater in the fjord. We demonstrated that the implementation of an idealized runoff at depth the head of the fjord influences temperature, salinity and circulation within the whole fjord.
Specifically, we found that in summer, when the discharge is bigger and the intermediary circulation weaker, warmer waters intrude in the fjord till the head of the fjord when an additional buoyant circulation is added. These results confirm that the glacier discharge is a key feature to implement: in order to understand the interplay of the shelf with the fjord the shelf forcing is not enough.
The second part of this chapter focused on sensitivity experiment in order to address the effect of a runoff with different properties at the sea-ice boundary. The key findings are the following:

I Changing temperature and salinity in a reasonable range (from observations, $\Delta T < 1.5$°C and $\Delta S < 1$ psu) has a negligible effect on the properties within the Sermilik fjord;

II The magnitude of the runoff chosen to be injected is a key factor in deter-

mining the properties of the fjord: we have demonstrated that the the the buoyancy induced circulation pulls water from the shelf and the heat transport at the 'head' of the fjord resulting from it linearly increases with the magnitude of the runoff itself.

III The depth of the runoff intruding from the ice-ocean boundary affects the properties and the in-ward heat transport depending on the structure of the water column of the fjord: in the summer Sermilik fjord case we observed that the most heat reaches the head when the depth over which the runoff is spread is 100 mt;

IV We observe as expected that the fjord has a non-linear dynamic response to the parameters we changed.

Chapter 5

Summary and conclusions

Greenland glacial fjords represent the natural link between the ice sheets and the large-scale ocean, being exposed to input of oceanic heat from the outside and source of melt-water from the ice-ocean boundary.

Nowadays there is widespread consensus that a portion of the recent Greenland mass loss was triggered by increased submarine melting at the glacier/ocean interface, located at the heads of Greenland's fjords [3]. As the properties inside glacial fjords are influenced by those on the adjacent shelves, knowledge of the processes that govern the variability of water mass properties on the Greenland shlef is an important step towards the understanding of the mechanisms behind the stability of the Greenland ice sheet.

However, the observational records on the continental shelf are scarce in space and time, preventing a full assessment of the relative partitioning of the water masses on the shelf, their interaction, and their seasonal to inter-annual variability. In this context, this thesis contributes to investigate the shelf and fjord dynamics and interaction by making use of numerical ocean/sea ice models based on the NEMO framework and observations.

Two model configurations have been used, a global eddying ocean at 1/16° horizontal resolution and a regional configuration at 1/48°. GLOB16, which reaches ∼4km horizontal resolution on the south-east Greenland shelf, is employed to investigate the variability of the currents, heat content and freshwater transports at different time scales, and to identify the potential drivers of their variability in the period 2008-2017.

With the available observations on the shelf (2008-2017) and the Cape Farewell

seasonality (2014-2016), we validated the (I) shelf modeled mean and summer estimates, (II) the Cape Farewell seasonal evolution and (III) the mean and seasonal SST on the shelf and the Irminger Sea.

The results show that the model is able to properly simulate the EGCC, EGC and IC mean pathways and properties. In good agreement with observations, the EGCC transports along the shelf increases while moving southward, where distinct branches of EGC/IC join together feeding the coastal current EGCC flowing on the shelf.

However, some discrepancies are found: (I) currents simulated by the model appear to be stronger and (II) waters flowing along the shelf are saltier and warmer than in observations. However, the anomalies have the correct amplitude: current anomalies go from -0.1 to 0.1 m/s, salinity anomalies from -0.2 to 0.2 psu and temperature anomalies range from -2 to 2 °C.

At Cape Farewell (near 60°N) we have simulated and compared year-round volume and freshwater transports, salinity and temperature fields with the OSNAP dataset. We underestimate (in average by 35%) the summer volume and freshwater transports, obtaining though reasonable results in modeling the increasing magnitude of the transports along the shelf. The observed transport maximum occurs in June and exhibits its minimum in November, while with our model we observed a shifted seasonality, peaking in March and having its minimum in July.

In summary, in Chapter 2 we provided for the first time a year-round validation and analysis on the SE shelf with a global model, showing the capability of the model in reproducing unique features that link the Arctic and the sub-polar Atlantic variability on the shelf.

An extension of the analysis presented in Chapter 2 would consist in addressing the discrepancies found in the transport variability, in order to understand the processes behind the shifted variability at Cape Farewell.

In Chapter 3, we demonstrated that the GLOB16 configuration is also able to reproduce the inter-annual temperature variability, and can capture exceptional years of deep convection in the Irminger Sea and the associated changes in temperature. Furthermore, the model is able to represent the variability of ocean temperature and atmospheric heat fluxes over the ISI region and the variability of the sea ice advected from the Arctic ocean on the shelf. We also find negative significant trends in sea ice concentrations on the shelf.

This thesis provided further steps in understanding the complex dynamics that take place on the SE Greenland shelf, highlighting the processes that concur in shaping the observed variability.
The main results are the following:

- In 2010 and 2015, anomalous positive (negative) atmospheric heat fluxes cause the ocean to warm (cool) due to enhanced (diminished) exchange with the atmosphere. This causes the winter mixed layer depth to increase (decrease) resulting in exceptional years of deep (shallow) convection in the ISI region. In these years the offshore part of shelf temperature changes accordingly to the ISI, even though the maximum anomalies are still found in the ISI region.

- The main driver of the variability in 2011 and 2016 is the heat transport through the Denmark Strait, that it is associated (in particular in 2016) with anomalous sea ice mass transport and a lack of sea ice on the entire shelf. The above results confirm that GLOB16, forced with the JRA55-do atmospheric reanalysis, is able to replicate the features that link the Arctic and the sub-polar Atlantic variability on the SE Greenland shelf

A further step would consist in performing quantitative analysis on the temperature and salinity structure of the East Greenland Coastal Current in different regimes of variability, using the whole GLOB16 hindcast which covers the period from from 1958 to 2018. Performing a composite analysis of years with same pattern of temperature variability would allow us to reach a more robust understanding of the processes behind the observed variability.
The processes that control the properties and circulation within the fjords and the connection with the shelf are investigated and presented in Chapter 4. In the Sermilik fjord region, we implemented a regional ocean configuration: with resolution of 1/48° (∼1 km) based on the relocatable ocean platform SURF. The main improvement we added to the system is a set of options to inject freshwater and river runoff to the ocean as surface boundary condition. Following the NEMO framework, runoff was inserted into the system at the top model cell, as traditionally done in many ocean models, but also at a non-zero depth with specified temperature and salinity. Injecting water at depth at the head of the fjord allows us to mimic an idealized Helheim discharge, and results in large impacts on

temperature, salinity and circulation within the whole fjord.
The innovative aspect of these modeling exercises with respect to previous studies is that this is the first time a relocatable model is implemented in the region, allowing us to have realistic bathymetry, forcings, initial and boundary conditions.
Furthermore, sensitivity experiments were run to evaluate the effect of a runoff with more realistic temperature, salinity and vertical structure at the sea-ice boundary in order to evaluate which are the runoff characteristics that affect the most the circulation and the properties of the fjord.
From these experiments we show that warmer waters from the shelf intrude till the head of the fjord when an additional buoyant circulation is added to the system. This implies that the buoyancy circulation induces more heat to be transported at the sea-ice boundary, and therefore possibly triggering more submarine melting.
Secondly, our findings suggest that the runoff properties that affect more significantly the properties in the fjord are depth and magnitude of runoff, while temperature and salinity changes within a realistic range affect the system in a negligible way.
Specifically we observe that the fjord response to a progressive increasing of the injected runoff amount is linear for the window of magnitudes here analyzed.
On the other hand, we have shown that when the depth of injection is set to where the PW layer is (in this case, $\sim$100 m), we have more AW intruding to the 'head' of the fjord leading to more heat transport at the sea-ice boundary.
This modeling study demonstrated that the glacier discharge is a key feature to be implemented to represent the fjord dynamics and properly reproduce the exchanges with the open ocean, and highlighted the need of the runoff-induced forcing in order to understand the interplay of the shelf with the fjord. This also suggests that a multi-variate analysis of different combinations of the parameters presented in Chap. 4 is necessary to reach a more comprehensive understanding of the fjord response to the shelf forcing and to the buoyant forcing.

Bibliography

[1] H. Zwally, Waleed Abdalati, T. Herring, Kristine Larson, Jack Saba, and Konrad Steffen. Surface melt-induced acceleration of greenland ice-sheet flow. *Science (New York, N.Y.)*, 297:218–22, 08 2002.

[2] Rignot, E., I. Velicogna, M. R.van den Broeke, A. Monaghan, J. Lenaerts. Acceleration of the contribution of the greenland and antarctic ice sheetsto sea level rise. 2011.

[3] F. Straneo and P. Heimbach. North atlantic warming and the retreat of greenland's outlet glaciers.

[4] Pickart R. S., Torres D. J., Fratantoni P. S. The east greenland spill jet. *J. Phys. Oceanogr., vol. 35, no. 6, pp. 1037-1053*, 2005.

[5] Laura C. Gillard, Xianmin Hu, Paul G. Myers, and Jonathan L. Bamber. Meltwater pathways from marine terminating glaciers of the greenland ice sheet. *Geophysical Research Letters*, 43(20):10,873–10,882, 2016.

[6] H. Luo, R. M. Castelao, A. K. Rennermalm, M. Tedesco, A. Bracco, P. L. Yager, and T. L. Mote. Oceanic transport of surface meltwater from the southern greenland ice sheet. *Nature Geosci.*, 9(7):528–532, 2016.

[7] Juliana M. Marson, Paul G. Myers, Xianmin Hu, and Julien Le Sommer. Using vertically integrated ocean fields to characterize greenland icebergs' distribution and lifetime. *Geophysical Research Letters*, 45(9):4208–4217, 2018.

[8] L. Wang, L. Zhang, C. Chen, M. Thomas, and M. K. Kaban. Anomalous acceleration of mass loss in the greenland ice sheet drainage basins and its contribution to the sea level fingerprints during 2010-2012. *The Cryosphere Discussions*, 2018:1–33, 2018.

[9] Le Bras I. A., Straneo F., Holte J., Holliday N. P. Seasonality of freshwater in the east greenland current system from 2014 to 2016. *J. Geophys. Res. Ocean., vol. 123, no. 12, pp. 8828-8848*, 2018.

[10] Sutherland D. A. and Pickart R. S. The east greenland coastal current: Structure, variability, and forcing.

[11] Wilkinson D. and Bacon S. The spatial and temporal variability of the east greenland coastal current from historic data.

[12] Straneo F. et al. Rapid circulation of warm subtropical waters in a major glacial fjord in east greenland. *Nat. Geosci., vol. 3*, 2010.

[13] Stearns, Leigh A., Hamilton, G. S. Rapid volume loss from two east greenland outlet glaciers quantified using repeatstereo satellite imagery.

[14] Enderlin E. M., Carrigan C. J., Kochtitzky W. H., Cuadros A., Moon T., Hamilton G. S. Greenland iceberg melt variability from high-resolution satellite observations.

[15] Dickson B., Dye S., Jonsson S., Kohl A., Macrander A., Marnela M., Meincke J., Olsen S., Rudels B., Valdimarsson H. and Voet G. The overflow flux west of iceland: Variability, origins and forcing. *978-1-4020-6773-0*, 2008.

[16] Rudels B., Fahrbach E., Meincke J., Budeus G., Eriksson P. The east greenland current and its contribution to the denmark strait overflow. *CES J. Mar. Sci., vol. 59, no. 6, pp. 1133-1154*, 2002.

[17] Bacon S., Myers P., Rudels B., Sutherland D. Accessing the inaccessible: Buoyancy driven coastal currents on the shelves ofgreenland and eastern canada,. *Arctic-Subarctic Ocean Fluxes: Defining the Role of the Northern Seas in Climate, edited by R. R. Dick-son, J. Meincke, and P. Rhines, chap. 28, pp. 701-720*, 2008.

[18] L. Havik, K. Vage, R. S. Pickart, B. Harden, W.J. von Appen, S. Jonsson, and S. Osterhus. Structure and variability of the shelfbreak east greenland current north of denmark strait. *Journal of Physical Oceanography*, 47(10):2631–2646, 2017.

[19] Bacon S,, Reverdin G., Rigor I. G., Snaith H. M. A freshwater jet on the east greenland shelf. *J. Geophys. Res., vol. 107, no. C7*, 2002.

[20] Straneo F. et al. Rapid circulation of warm subtropical waters in a major glacial fjord in east greenland.

[21] Madec G. and the NEMO Team. Nemo ocean engine. note du pole de modelisation. *no. 27, pp. 1-332*, 2006.

[22] Iovino D., Masina S., Storto A., Cipollone A., Stepanov V. N. A 1/16° eddying simulation of the global nemo sea-ice-ocean system. *Model Dev., vol. 9, no. 8, pp. 2665-2684*, 2016.

[23] Nurser A. J. G. and Bacon S. The rossby radius in the arctic ocean. *Ocean Sci., 10, 967-975*, 2014.

[24] Locarnini R. A. et al. World ocean atlas 2013, volume 1: Temperature. *NOAA Atlas NESDIS 73, vol. 1, no. September*, 2013.

[25] Zweng MM et al. World ocean atlas 2013, volume 2: Salinity. *NOAA Atlas NESDIS 74, vol. 2, no. September*, 2013.

[26] Kobayashi, S. et al. The jra-55 reanalysis: General specifications and basic characteristics. 2015.

[27] NODC and Rosenstiel School of Marine and Atmospheric Science. Avhrr pathfinder level 3 monthly daytime sst version. *https://doi.org/10.5067/PATHF-MOD50.*

[28] Lozier M. S. et al. Overturning in the subpolar north atlantic program: A new international ocean observing system. *Bull. Am. Meteorol. Soc., vol. 98, no. 4, pp. 737-752*, 2017.

[29] Wunsch, Carl and Heimbach, Patrick. Two decades of the atlantic meridional overturning circulation: Anatomy, variations, extremes, prediction, and overcoming its limitations. *Journal of Climate*, 26:7167–7186, 09 2013.

[30] L. P. Thierry Virginie, Mercier Herle, Petit Tillys, Branellec Pierre, Balem Kevin. Reykjanes ridge experiment (rrex) dataset. *https://doi.org/10.17882/55445, 2018.*

[31] N. P. Holliday, A. Meyer, S. Bacon, S. G. Alderson, and B. de Cuevas. Retroflection of part of the east greenland current at cape farewell. *Geophys. Res. Lett., vol. 34, no. 7, pp. 1-5*, 2007.

[32] S. Bacon, A. Marshall, N. P. Holliday, Yevgeny Aksenov. Seasonal variability of the east greenland coastal current. *J. Geophys. Res. Ocean.*, 2014.

[33] P. Lin, R. S. Pickart, D. J. Torres, and A. Pacini. Coastal current at the southern tip of greenland. *J. Phys. Oceanogr., vol. 48, no. 9, pp. 2127-2140*, 2018.

[34] B. E. Harden, F. Straneo, and D. A. Sutherland. Moored observations of synoptic and seasonal variability in the east greenland coastal current. *Geophys. Res. Ocean., vol. 119, no. 12, pp. 8838-8857*, 2014.

[35] N. P. Holliday et al. Subpolar north atlantic overturning and gyre-scale circulation in the summers of 2014 and 2016. *J. Geophys. Res. Ocean., vol. 123, no. 7*, 2018.

[36] Sutherland D. A. et al. Atlantic water variability on the se greenland continental shelf and its relationship to sst and bathymetry.

[37] D. Carroll et al. Subannual and seasonal variability of atlantic-origin waters in two adjacent west greenland fjords.

[38] S. A. Good, M. J. Martin, and N. A. Rayner. En4: Quality controlled ocean temperature and salinity profiles and monthly objective analyses with uncertainty estimates. *J. Geophys. Res. Ocean., vol. 118, no. 12, pp. 6704-6716*, 2013.

[39] G. Peng, W. N. Meier, D. J. Scott, and M. H. Savoie. A long-term and reproducible passive microwave sea ice concentration data record for climate studies and monitoring. *Earth Syst. Sci. Data, vol. 5, no. 2, pp. 311-318*, 2017.

[40] J. C. Comiso. Bootstrap sea ice concentrations from nimbus-7 smmr and dmsp ssm/i-ssmis, version 3. *Boulder, Color. USA. NASA Natl. Snow Ice Data Cent. Distrib. Act. Arch. Center.*, 2017.

[41] M. Femke de Jong, Marilena Oltmanns, Johannes Karstensen, Laura de Steur. Deep convection in the irminger sea observed with a dense mooring array. *Oceanography*, 31:50–59, 2018.

[42] P. Zunino, H. Mercier, and V. Thierry. Two superimposed cold and fresh anomalies enhanced irminger sea deep convection in 2016-2018. *Ocean Sci. Discuss., no. May, pp. 1-29*, 2018.

[43] Bacon S, Aksenov Y, Fawcett S, Madec G. Arctic mass, freshwater and heat fluxes: methods and modelled seasonal variability. *Phil. Trans. R. Soc. A 373: 20140169*, 2014.

[44] Adrian Gill . Atmosphere-ocean dynamics. *Volume 30*, 1982.

[45] Greatbatch, Richard J. A note on the representation of steric sea level in models that conserve volume rather than mass. *Journal of Geophysical Research: Oceans*, 99(C6):12767–12771, 1994.

[46] Chafik L., Nilsen J.E., Dangendorf S., Reverdin G., Frederikse T. North atlantic ocean circulation and decadal sea level change during the altimetry era. *Scientific Reports*, 2019.

[47] de Steur L., Pickart R. S., Macrander A., Vage K., Harden B., Jonsson S., Osterhus S., Valdimarsson H. Liquid freshwater transport estimates from the east greenland current based on continuous measurements north of denmark strait. *Journal of Geophysical Research: Oceans*, 2016.

[48] F. Straneo and C. Cenedese. The dynamics of greenland's glacial fjords and their role in climate. *Ann. Rev. Mar. Sci., vol. 7, no. 1, pp. 89-112*, 2015.

[49] B. Holland, D. M., Thomas, R. H., de Young, B., Ribergaard, M. H., Lyberth. Acceleration of jakobshavn isbrae triggered by warm subsurface ocean waters. *Nat. Geosci., vol. 3, no. 3*, 2010.

[50] E. Rignot, M. Koppes, and I. Velicogna. Rapid submarine melting of the calving faces of west greenland glaciers. *Ann. Rev. Mar. Sci., vol. 7, no. 1, pp. 89-112*, 2015.

[51] F. Straneo et al. Challenges to understand the dynamic response of greenland's marine terminating glaciers to oceanic and atmospheric forcing. *Bull. Am. Meteorol. Soc., no. august, p. 130117123745009*, 2013.

[52] R. H. Jackson and F. Straneo. Heat, salt, and freshwater budgets for a glacial fjord in greenland. *J. Phys. Oceanogr., vol. 46, no. 9, pp. 2735-2768*, 2016.

[53] E. M. Enderlin, C. J. Carrigan, W. H. Kochtitzky, A. Cuadros, T. Moon, and G. S. Hamilton. Greenland iceberg melt variability from high-resolution satellite observations. *Cryosphere, vol. 12, no. 2, pp. 565-575*, 2018.

[54] C. S. Andresen et al. Rapid response of helheim glacier in greenland to climate variability over the past century. *Nat. Geosci., vol. 5, no. 1, pp. 37-41*, 2012.

[55] Oltmanns M., Straneo F., Moore G. W. Kn. Strong downslope wind events in ammassalik, southeast greenland. *J. Clim. 27 977-993*, 2014.

[56] S. H. Mernild et al. Freshwater flux to sermilik fjord, se greenland. *Cryosphere, vol. 4, no. 4, pp. 453-465*, 2010.

[57] Jenkins, Adrian. Convection-driven melting near the grounding lines of ice shelves and tidewater glaciers. *Journal of Physical Oceanography*, 41(12):2279–2294, 2011.

[58] Yun Xu, Eric Rignot, Ian Fenty, Dimitris Menemenlis, and M. Mar Flexas. Subaqueous melting of store glacier, west greenland from three-dimensional, high-resolution numerical modeling and ocean observations. *Geophysical Research Letters*, 40(17):4648–4653, 2013.

[59] R. Sciascia, F. Straneo, C. Cenedese, and P. Heimbach. Seasonal variability of submarine melt rate and circulation in an east greenland fjord. *J. Geophys. Res. Ocean., vol. 118, no. 5, pp. 2492-25061*, 2013.

[60] Fiammetta Straneo, David A. Sutherland, David Holland, Carl Gladish, Gordon S. Hamilton, Helen L. Johnson, Eric Rignot, Yun Xu, and Michele

Koppes. Characteristics of ocean waters reaching greenland's glaciers. *Annals of Glaciology*, 53(60):202–210, 2012.

[61] R. H. Jackson, F. Straneo, and D. A. Sutherland. Externally forced fluctuations in ocean temperature at greenland glaciers in non-summer months. *Nat. Geosci., vol. 7, no. 7, pp. 503-508*, 2014.

[62] M. H. Johnson H. L., Munchow A., Falkner K. K. Ocean circulation and properties in petermann fjord, greenland. *J. Geophys. Res., 116C01003*, 2011.

[63] F. Straneo et al. Impact of fjord dynamics and glacial runoff on the circulation near helheim glacier. *Nat. Geosci., vol. 4, no. 5, pp. 322-327*, 2011.

[64] F. Trotta et al. A structured and unstructured grid relocatable ocean platform for forecasting (surf). *Deep. Res. Part II Top. Stud. Oceanogr., vol. 133, pp. 54-75*, 2016.

[65] Bellafiore D. Hydrodynamic coastal processes in the north adriatic investigated with a 3d finite element model. *Ocean Dyn., 60 255-273*, 2010.

[66] Griffies S. Fundamentals of ocean climate models. 2004.

[67] Bruno Blanke and Pascale Delecluse. Variability of the tropical atlantic ocean simulated by a general circulation model with two different mixed-layer physics. *Journal of Physical Oceanography*, 23(7):1363–1388, 1993.

[68] B. IOC, IHO. Centen. ed. gebco digit. atlas, publ. cd-rom behalf intergov. oceanogr. comm. int. hydrogr. organ. as part gen. bathymetr. chart ocean. br. oceanogr. dat,. 2003.

[69] M. Morlighem et al. Icebridge bedmachine greenland, version 3. 2018.

[70] S. H. Mernild et al. Freshwater flux to sermilik fjord, se greenland. *Cryosphere, vol. 4, no. 4, pp. 453-465.*

[71] David A. Sutherland, George E. Roth, Gordon S. Hamilton, Sebastian H. Mernild, Leigh A. Stearns, and Fiammetta Straneo. Quantifying flow regimes in a greenland glacial fjord using iceberg drifters. *Geophysical Research Letters*, 41(23):8411–8420, 2014.

[72] Rebecca H. Jackson, Steven J. Lentz, and Fiamma Straneo. The dynamics of shelf forcing in greenlandic fjords. *Journal of Physical Oceanography*, 48(11):2799–2827, 2018.